

Radio-Frequency Heating of Magnetic Nanoparticles

A thesis submitted in partial fulfillment of the
requirements for the degree of
Master of Science

by

Mohammud Zafrullah JAGOO
BSc., University of Mauritius, 2009

2012

Wright State University

Wright State University
School of Graduate Studies

March 16, 2012

I hereby recommend that the thesis prepared under my supervision by Mohammad Zafrullah Jagoo entitled RF Heating of Magnetic Nanoparticles be accepted in partial fulfillment of the requirements for the degree of Master of Science.

Gregory Kozlowski, Ph.D.
Thesis Director

Lok C. Lew Yan Voon, Ph.D.
Chair, Department of Physics

Committee on
Final Examination

Gary Farlow, Ph.D.

Jerry Clark, Ph.D.

Andrew Hsu, Ph.D.
Dean, Graduate School

Jagoo, Mohammad Zafrullah. M.S., Department of Physics, Wright State University, 2012. Radio-Frequency Heating of Magnetic Nanoparticles.

Abstract

In the present study, a power supply capable of converting a direct current into an alternating current was built. The frequency of oscillation of the output current could be varied from 174.8 kHz to 726.0 kHz by setting a set of capacitors in resonance. To this power supply is attached a 20-turns copper coil in the shape of a spiral. Because of the high heat generated in the coil, the latter has to be permanently water-cooled. A vacuum pump removes the air between the sample holder and the coil. A fiber optic temperature sensor with an accuracy of 0.001 °C was used to measure the temperature of the nanoparticles.

Four ferromagnetic nanoparticles (CoFe_2O_4 , NiFe_2O_4 , $\text{Ni}_{0.5}\text{Zn}_{0.5}\text{Fe}_2\text{O}_4$, $\text{Co}_{0.4}\text{Ni}_{0.4}\text{Zn}_{0.2}\text{Fe}_2\text{O}_4$) with different magnetic properties were subjected to heating. The heating performance is given by the specific power loss (SPL) which was calculated from the initial slope of the heating curve whereby there is minimum heat loss to the surroundings and the highest SPL was obtained when magnetic field and frequency were highest at 2.06×10^{-5} T and 348.0 kHz, respectively. When the frequency was changed from 174.8 to 348.0 kHz, the SPL value was double indicating a one-to-one relationship between the frequency and the SPL. No such relationships were found when the magnetic field was increased from 1.38×10^{-5} T to 2.06×10^{-5} T. There is also a coercivity and remanent magnetization dependence on the SPL and both of them obey an inverse law. We found that the SPL for $\text{Ni}_{0.5}\text{Zn}_{0.5}\text{Fe}_2\text{O}_4$ (GPZ4) was 1.09 ± 0.02 W/g². Moreover, the sample CoFe_2O_4 (GPZ11) with the highest power loss density (12250 J/m³) measured by the variable sample magnetometer was found to have the lowest SPL (0.135 ± 0.002 W/g²) in the lot. The magnetic field inside the coil is only a fraction the VSM, so when the low magnetic field was turned on, the hysteresis loop opened only to the extent of the minor loop.

Contents

1	Introduction	1
1.1	Importance of Nanoparticles	1
1.2	Nanotechnology: The Plastics of the 21st Century?	3
1.3	Aims of the Project	3
1.4	Structure of Report	4
2	Nanoparticles	5
2.1	Nanostructures	5
2.2	Nanoparticles as Intermediate Systems	5
2.3	Origins of Magnetism	6
2.3.1	Constituent Equations in Magnetism	9
2.4	Magnetism in Matter	9
2.4.1	Diamagnetic Materials	9
2.4.2	Paramagnetic Materials	10
2.4.3	Ferromagnetic Materials	11
2.4.3.1	Magnetic Anisotropy	14
2.4.3.2	Domain Structure	16

2.5	Nanomagnetism	18
2.5.1	Single-Domain Particles	18
2.5.1.1	Coercivity of Single-Domain Particles	19
2.5.2	Superparamagnetism	20
2.5.2.1	ZFC-FC Measurement	24
2.6	Summary of Chapter 2	26
3	Magnetic Heating	30
3.1	Hysteresis	30
3.2	Neel and Brown Relaxation	32
3.3	Frictional Losses	34
3.4	Chapter Summary	35
4	AMF System	36
4.1	Specific Power Loss	36
4.2	Temperature Measurement	37
4.2.1	Temperature Probes	37
4.2.2	Choice of Thermometer	40
4.2.3	FISO Inc. FOT-L Temperature Sensor	41
4.3	Frequency of Operation	43
4.3.1	Magnetic Field	47
4.3.1.1	Design of Coil	48
4.3.2	AMF Power Supply	50
4.3.3	Optimization of the System	54
4.3.4	End-Product	56
4.3.5	Commercially Available Systems	56
4.3.5.1	Comparison with Commercially Available System	58
4.4	Chapter Summary	59
5	Results	61
5.1	Magnetic Nanoparticles	61
5.2	Mass Measurement	63
5.3	Holding Container	63
5.4	Test Measurement	65

5.5	Resonance Frequency	68
5.6	WSU Magnetic Field	69
5.6.1	Simulated Field	70
5.6.2	Measured Magnetic Field	70
5.7	Magnetic Heating	70
5.7.1	GPZ4	74
5.7.2	GPZ5	75
5.7.3	GPZ8	76
5.7.4	GPZ11	77
5.8	QU Magnetic Field	80
5.9	Magnetic Heating	80
5.9.1	GPZ4	83
5.9.2	GPZ5	84
5.9.3	GPZ8	85
5.9.4	GPZ11	86
5.10	Chapter Summary	87
6	Analysis and Discussion	88
6.1	Heating Rate	88
6.2	WSU	91
6.2.1	GPZ4	91
6.2.2	GPZ5	91
6.2.3	GPZ8	94
6.2.4	GPZ11	94
6.3	QU	96
6.3.1	GPZ4	96
6.3.2	GPZ5	96
6.3.3	GPZ8	98
6.3.4	GPZ11	100
6.4	Normalized SPL	100
6.5	Magnetic Field Dependence of SPL	107
6.5.1	Estimation of the Magnetic Field at Queen's University . .	109
6.6	Frequency Dependence of SPL	109

6.7	Magnetic Property Dependence of SPL	111
6.7.1	Remanent Magnetization	112
6.7.2	Saturation Magnetization	113
6.7.3	Coercive Forces	114
6.8	Grain Size Effect	115
6.9	Discrepancy between Measured Values	117
6.10	Chapter Summary	117
7	Conclusion	119
7.1	Future Works	120
A	Procedure for using AMF System	122
A.1	AMF Hardware	122
A.2	Testing	122
	References	124

List of Figures

1.1	Nanotechnology-related goods and services	3
2.1	Band gap energy of molecules, nanoparticle and bulk materials . .	7
2.2	Magnetization vs. applied magnetic field for a ferromagnetic substance	12
2.3	Magnetization vs. temperature for a ferromagnetic substance . . .	13
2.4	Magneto-crystalline anisotropy	15
2.5	Decrease of magnetic energy by domain splitting	17
2.6	Domain wall	18
2.7	Fanning mechanism	20
2.8	Curling mechanism	21
2.9	Energy of a superparamagnetic particle	22
2.10	Hysteresis loop of superparamagnetic particle	23
2.11	ZFC-FC measurements	26
2.12	Hysteresis loops for paramagnetic, ferromagnetic and superparamagnetic materials	28
2.13	Size effect on ferromagnetic/superparamagnetic particles	28

3.1	Magnetizing and demagnetizing of ferromagnets	31
4.1	FISO FOT-L	43
4.2	Electromagnetic spectrum	44
4.3	Power density	46
4.4	Magnetic field of solenoid	48
4.5	Tailor-made coil	49
4.6	Coil cooling mechanism	51
4.7	Schematic of power supply	52
4.8	BK Precision 4011A function generator	53
4.9	Set-up assembly	55
4.10	Complete system setup	57
4.11	Ambrell EASYHEAT induction heater	58
4.12	Coil in Belfast	59
5.1	Hysteresis loop, coercivity, and saturation magnetization	62
5.2	Mass balance	64
5.3	Wilmad NMR tubes	64
5.4	Probe position relative to powder	65
5.5	Test Measurement	66
5.6	CRO output	69
5.7	WSU field profile	71
5.8	Induction coil	72
5.9	Magnetic field measurements	72
5.10	Temperature against time of GPZ4	74
5.11	Temperature against time of GPZ5	75
5.12	Temperature against time of GPZ8	76
5.13	Temperature against time of GPZ11	77
5.14	QU field profile	81
5.15	Temperature against time of GPZ4	83
5.16	Temperature against time of GPZ5	84
5.17	Temperature against time of GPZ8	85
5.18	Temperature against time of GPZ11	86

6.1	Heating rate curve	89
6.2	Time evolution of gradient	90
6.3	Heating of GPZ4 magnetic nanoparticles	92
6.4	Heating of GPZ5 MNP	93
6.5	Heating of GPZ8 MNP	94
6.6	Heating of GPZ11 MNP	95
6.7	Heating of GPZ4 MNP	97
6.8	Heating of GPZ5 MNP	98
6.9	Heating of GPZ8 MNP	99
6.10	Heating of GPZ11 MNP	101
6.11	Heat capacity vs. saturation magnetization	103
6.12	Normalized SPL vs. current	106
6.13	Magnetic field effect on SPL	107
6.14	Current effect on SPL	108
6.15	Frequency effect on SPL	109
6.16	Frequency significance on SPL	110
6.17	SPL vs. remanent magnetization	112
6.18	SPL vs. saturation magnetization	113
6.19	SPL vs. coercivity	114
6.20	SPL vs. grain size	116
6.21	Minor loops	118

List of Tables

1.1	Generation of Intel microprocessors	2
4.1	Characteristics of thermometers	41
4.2	Specifications of FOT-L	42
5.1	The sizes and magnetic properties of the nanoparticles are shown as measured by the VSM, SEM and XRD.	63
5.2	Resonance frequencies of power supply	68
6.1	Heating of GPZ4 magnetic nanoparticles (MNP)	91
6.2	Heating of GPZ5 MNP	92
6.3	Heating of GPZ8 MNP	95
6.4	Heating of GPZ11 MNP	96
6.5	Heating of GPZ4 MNP	96
6.6	Heating of GPZ5 MNP	99
6.7	Heating of GPZ8 MNP	100
6.8	Heating of GPZ8 MNP	100
6.9	Heat Capacities of some ferrites	102
6.10	Heat Capacities of some ferrites (contd.)	104

6.11 Normalized SPL at WSU 105
6.12 Normalized SPL at QU 105

Acknowledgements

This research bears the imprints of many people who have contributed in one way or the other in its completion.

First of all, I wish to express my gratitude to Dr. Gregory Kozlowski, my research supervisor, for his enthusiasm, unrelenting attention, support, useful advice, encouragement, excellent guidance and comments without whom it would have been very impossible for me to complete this project.

I would also like to express my gratitude to Dr. Evgeny Rebrov for granting me full access to his lab. He helped me understanding the mechanism for heat-to-mass transfer.

I would like to thank Dr. Lok Lew Yan Voon, program coordinator at Wright State University for his useful advice. He is someone I admire and trust a lot.

It will not be fair if I fail to mention Dr. Gary Farlow's name in this work. He has assisted me wholeheartedly during laboratory work and has never failed to answer any of my questions.

I would also like to thank Dr. Jerry Clark for his help in solving for the magnetic field of the coil.

Thanks to Dr. Zafer Turgut, Dr. Hiroyuki Kosai, Tyler Bixel and Alex Sheets for their help in building the coil and power supply.

Even though they are far from here, I would like to thank my father and my mother for their moral support, spiritual support and on-going kindness.

A special thank goes to all those people not mentioned but have in one way or another supported me to complete this research work.

Last but not least, I am grateful to God who has sorted me out from every difficult situation in life.

To my parents...

CHAPTER 1

Introduction

Imagine how incredible our world would be without surgical blades! A world where surgical procedures are nonexistent; a world where the word operation is an anachronism. This utopic world is possible with the development of nanoparticles for the administration of which can be used to destroy the cancerous cells.

1.1 Importance of Nanoparticles

Nanoparticle science is a novel field in the sense that much research is on-going. Much effort is devoted to get the perfect blend between the composition of the particles and their size. As a matter of fact, nanoparticles can be used for practically everything if they are properly harnessed. The world is migrating towards nanotechnology as we continue to miniaturize everything. The best example is to consider how computers have changed in the time span of one century, where "smaller" has meant greater performance ever since the advent of integrated circuits: more components per chip, faster operation, lower cost, and less power consumption [1]. In the 1940's, the ENIAC (Electronic Numerical Integrator And Computer) was developed and it occupied more than 1500 sq. ft. of floor space. With the advent of transistors, sophisticated computers could fit in a single normal size bedroom, instead of the six regular bedrooms for the ENIAC. Three decades later, the integrated circuit which contained thousands of transistors and

Table 1.1: Generation of Intel microprocessors

Processor	Year	Feature Size (μm)	Transistors	Frequency (MHz)
4004	1971	10	2.3 k	0.75
8008	1972	10	3.5 k	0.5-0.8
8080	1974	6	6 k	2
8086	1978	3	29 k	5-10
80286	1982	1.5	134 k	6-12
Intel386	1985	1.5-1.0	275 k	16-25
Intel486	1989	1-0.6	1. 2M	25-100
Pentium	1993	0.8-0.35	3.2-4.5 M	60-300
Pentium Pro	1995	0.6-0.35	5.5 M	166-200
Pentium II	1997	0.35-0.25	7.5 M	233-450
Pentium III	1999	0.25-0.18	9.5-28 M	450-1000
Pentium 4	2001	0.18-0.13	42-55 M	1400-3200

other parts on a silicon chip reduced the size of computers drastically. We can see in Table 1.1 how the Intel processor has evolved over three decades. The size of the processor changed from 10 μm for the 4004 processor to 0.18-0.13 μm during that time period. The meaning of this is that in the same physical dimension, more transistors can be implemented and the trend of the number of transistors per chip is also evident from the same table. Apparently, the plateau for the number of transistors per chip has not been reached. As of the time of writing, the latest microprocessor, which in fact is a nanoprocessor is 32 nm (Intel Core i7 Gulftown) and it boasts more power than all the primitive computers combined. With the reduced size of chips, it is now possible to hold a computer in the palm of the hand.

Particle science has unfortunately not followed the same trend as silicon chips until recently. Now there is a big boom on the development and use of nanomaterials. I firmly believe that nanoparticle science is a silver bullet for many of the problems, especially in the medical sector, which humanity is facing.

1.2 Nanotechnology: The Plastics of the 21st Century?

Many scientists view nanotechnology as the revolutionary technology of the 21st century. Just as plastics were a pervasive and revolutionary product of the 20th century, nanotechnology products are expected to have widespread use and change our lives in a myriad of ways. Nanotechnology products are currently in use in more than 200 consumer products, ranging from air conditioners to sunscreen [2]. The National Science Foundation forecasts that \$1 trillion in nanotechnology-enabled products will be on the market by 2015 [3]. Figure 1.1 gives a pictorial overview of how the budget of the National Science Foundation is imparted to different sectors. The majority of the budget is devoted to developing new materials.

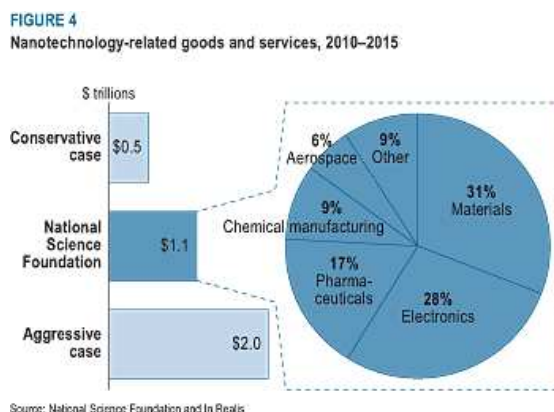


Figure 1.1: Nanotechnology-related goods and services

1.3 Aims of the Project

This project aims at synthesizing nanoparticles and then designing the relevant apparatus for measuring one or more physical quantities of the prepared nanoparticles. There will be several preliminary scientific targets to be accomplished on the way and one of them is to magnetically characterize the nanoparticles. Thus, different sets of measurements will be performed to determine the most suitable

type of nanoparticle that can be useful for other purposes. Consequently, the degree to which the nanoparticles can be used for the proper treatment of cancer cells will be scrutinized. Later on, we can speculate on issues of large-scale deployment of the apparatus and its economics.

1.4 Structure of Report

An outline of the remaining chapters of this report is as follows:

Chapter 2 gives an exposé on the nanoparticles with concentration on the types of nanoparticles. Emphasis will be laid on magnetic nanoparticles.

Chapter 3 elaborates on the different type of heating mechanisms for magnetic nanoparticles. A review of the existing applications that have proved themselves will be given.

Chapter 4 details each stage of the design of our own model of the radio-frequency (RF) apparatus for the heating of the magnetic nanoparticles. Simulations of how the system works will be illustrated.

Chapter 5 displays the results from several experiments carried out in the lab. It also evaluates the performance of the system.

Chapter 6 analyzes the results from all the experiments performed and logical judgments will be drawn from the analysis. Moreover, the best experimental tuning and magnetic nanoparticle will be deduced.

Chapter 7 concludes the report by summarizing the important results and also suggesting future recommendations to improving the prototype.

CHAPTER 2

Nanoparticles

2.1 Nanostructures

Nanostructures are structures that are defined as having at least one dimension between 1 and 100 nm; that is, reducing one, two or three dimensions of a bulk material to a nanometer scale produces nanometer thick 2D layers, 1D nanowires (or nanotubes), or 0D nanoclusters, respectively [4]. Nanoclusters usually have a very narrow size distribution. Nanowires (or nanotubes) are structures that have a lateral size constrained to a few nanometers and an unconstrained longitudinal size. A 2D nanolayer can be defined as an infinite plane of nanomaterials. These form the most fundamental subdivision of nanoparticles [5]. Nanomaterials possess very high surface to volume ratios because of the fine grain size and they are characterized by a very large amount of low-coordination number atoms at edge and corner sites.

2.2 Nanoparticles as Intermediate Systems

Atoms and molecules exhibit properties that follow quantum mechanical rules, while the chemical and physical properties of bulk materials obey the laws of classical mechanics. In the middle, nanosystems display electronic, photochemical, electrochemical, optical, magnetic, mechanical or catalytic properties that

differ significantly not only from those of molecular units, but also from those of macroscopic systems. In physical terms, nanoparticles have different properties: they have a large surface area in relation to their tiny mass and at the same time a small number of atoms. This can produce quantum effects that lead to altered material properties [6]. Typical quantum effects arise in atomic-sized and eventually nano-sized objects because their global dimensions are comparable to the characteristic wavelength for fundamental excitation in materials. The latter (including the electron wavelength, phonons, photons, etc.) carry the fundamental unit of energy - quantum - through materials and therefore govern the dynamics of their propagation and conversion from one form to another. However, if the size of the structures is in the same order of magnitude of these characteristic wave functions, the propagation and the behavior of quanta are noticeably perturbed and thus quantum mechanical selection rules appear. Quantum mechanical selection rules are usually ignorable for a larger systems but have to be catered for in these nanosystems. The drift is shown in Figure 2.1 where for a single molecule, there are only a few energy levels which increases for a nanosystem and the energy levels cannot be distinguished for a bulk material. For example, in the case of metals, typical "metallic" properties, like conductivity, decrease when the size is reduced and when the number of constituent atoms in the sample is significantly diminished. Indeed, the electronic conduction band of a metal gradually evolves from continuous levels of a bulk infinite material into discrete states as a function of size reduction, resulting in an increase in the band-gap energy [7].

These structures have intrigued scientists in the last two decades for their strange and fascinating properties and apparent inexhaustible applications which are dissimilar to their bulk counterparts [4]. Hence by tweaking the properties and composition of the structures, desirable novel properties may be obtained.

2.3 Origins of Magnetism

Before diving into the magnetism of nanoparticles, a brief recapitulation of bulk magnetism will be discussed in the following sections. As we all know, electricity and magnetism are coupled and James Clark Maxwell laid the founding stones of

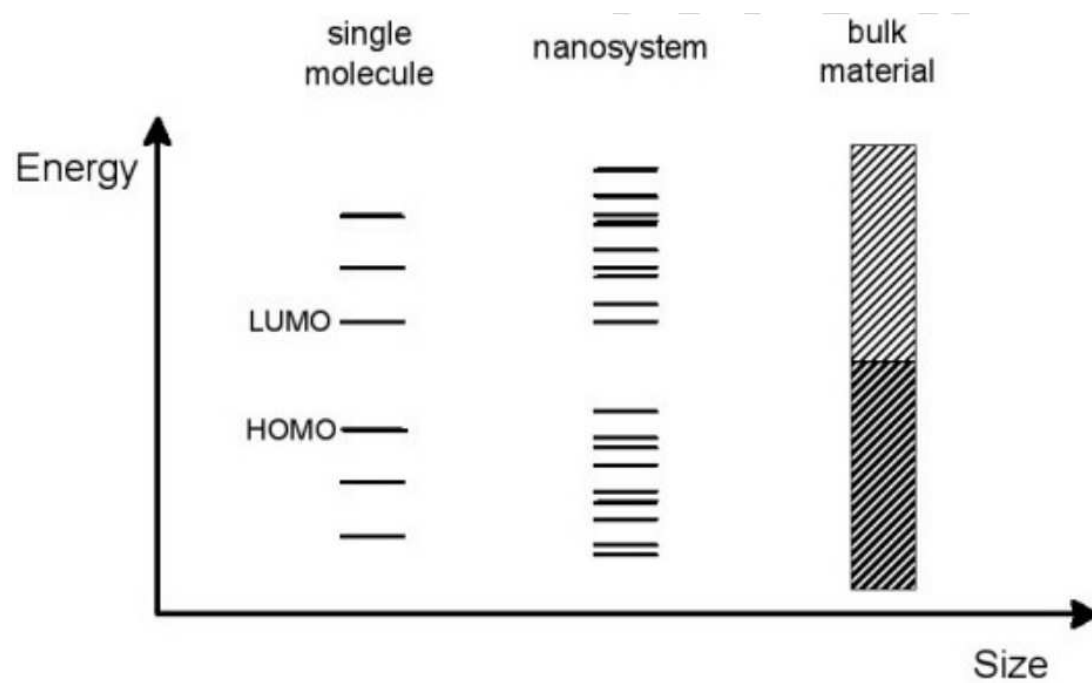


Figure 2.1: Band gap energy of molecules, nanoparticle and bulk materials

magnetism from a physical point of view. In differential form, Maxwell's equations are as follows:

$$\nabla \cdot \vec{E} = \frac{\rho}{\varepsilon_0} \quad (2.1)$$

$$\nabla \cdot \vec{B} = 0 \quad (2.2)$$

$$\nabla \times \vec{E} = -\frac{\partial \vec{B}}{\partial t} \quad (2.3)$$

$$\nabla \times \vec{B} = \mu_0 \vec{J} + \mu_0 \varepsilon_0 \frac{\partial \vec{E}}{\partial t} \quad (2.4)$$

The first equation (Eq. 2.1), inherently known as Gauss's law shows how an electric field (\vec{E}) is formed by a charge density (ρ). ε_0 is an electric constant called the permittivity of free space.

Eq. 2.2 is the famous Gauss's law for magnetism with \vec{B} as the magnetic field. There are two important results to this law. Firstly, magnetic field lines always form continuous loops and thus all closed surfaces have the same number of magnetic field lines going in as coming out. Hence, the zero magnetic flux on the right hand side of the equation. Secondly, there is a break of symmetry in this equation as compared to Eq. 2.1 in the sense that there are no magnetic monopoles while there are electric monopoles. Magnetic dipoles which are basically current loops produce the required magnetic fields.

Faraday's law of induction (Eq. 2.3) shows how a time-varying magnetic field creates an electric field.

Finally, Ampere's circuital law (Eq. 2.4) describes how magnetic fields are created. An electric current density (\vec{J}) produces a magnetic field and time-varying electric fields also create magnetic fields. The magnetic constant or the permeability of free space (μ_0) dimensionalizes the equation.

Based on Maxwell's equations, we can safely say that moving charges form the basis of magnetism in matter. From a quantum mechanical perspective, we

can deduce that there is the orbital motion of the electron and the spin of the electron. These two electronic motions mainly give rise to magnetism in the atom.

2.3.1 Constituent Equations in Magnetism

$$\vec{B} = \mu \vec{H} = \mu_o (1 + \chi) \vec{H} \quad (2.5)$$

$$\vec{M} = \chi \vec{H} \quad (2.6)$$

$$\chi = \frac{\mu}{\mu_o} - 1 \quad (2.7)$$

Eq. 2.5 shows how the magnetic field is related to the magnetizing field (\vec{H}) and Eq. 2.6 demonstrate that a material will have a net magnetization (\vec{M}) when a magnetizing field is applied. χ is the magnetic susceptibility which is a property of the material in question. Eq. 2.7 relates the permeability of the material, the permeability of free space and the magnetic susceptibility.

2.4 Magnetism in Matter

The type of response of materials to an applied magnetic field depends on the properties of the individual atoms or molecules and also on the nature of the interactions. The latter allows us to classify materials into three categories: diamagnetic, paramagnetic and ferromagnetic.

2.4.1 Diamagnetic Materials

Diamagnetic substances consist of atoms or molecules with no net spin angular momentum. The response to an applied magnetic field is the creation of circulating atomic currents that produce a very small bulk magnetization opposing the applied field [8]. The susceptibility (Eq. 2.8), which is a measure of how effective an applied field is for inducing a magnetic dipole, of a diamagnetic material is less than zero ($\chi < 0$). This is because when an applied field is being experienced by

a material, the induced moment is opposite to the field as orbital velocity of electrons around their nuclei is changed. In diamagnetism, only the outermost shells significantly contribute due to the susceptibility of the material. The equation governing diamagnetism is

$$\chi = -\frac{N \mu_o e^2}{V 6m} \sum_i \langle r^2 \rangle \quad (2.8)$$

where N is the number of atoms, e is the charge of the electron, V is the volume, m is the mass of the electron, and $\langle r \rangle$ is the average orbital radius. Lenz's rule explains the origin of the negative sign for this equation.

Proof of Eq. 2.8 can be found in [9]. We can also infer from the equation that for diamagnetic materials, the temperature dependence is negligible.

2.4.2 Paramagnetic Materials

Paramagnetic substances have a net angular momentum arising from unpaired electrons (cf. Hund's rules). The magnetic moment of the extra odd electron in the outermost shell is aligned parallel to the applied field [8]. Therefore, paramagnetic substances have a positive magnetic susceptibility. Without an external magnetic field no favored orientation of the magnetic moments occurs and the resulting magnetization tends to zero. But, the application of an external magnetic field produces a net magnetization in a preferential orientation. For low magnetic fields, the susceptibility of an atom can be described as

$$\chi = \frac{n \mu_o g_J^2 \mu_B^2 J(J+1)}{3k_B T} \quad (2.9)$$

with J being the total angular momentum, g as the Lande factor, n the number of magnetic moments, μ_B is the Bohr magneton, T is the temperature, k_B is the Boltzmann's constant.

Similarly, for larger magnetic fields, the saturation magnetization is reached so that $J(J+1) \sim J^2$ as shown

$$\chi = \frac{n \mu_o g_J^2 \mu_B^2 J^2}{3k_B T} \quad (2.10)$$

As both equations show, the susceptibility is highly dependent on the temperature. Another end result is the permeability of paramagnetic materials which decrease at high temperatures because of randomizing effect of thermal excitations. A formal treatment can be found in [9].

2.4.3 Ferromagnetic Materials

In ferromagnetic materials, each atom has electronic magnetic moments, and these moments are all aligned in the same direction when the material is fully magnetized (saturation magnetization). Ferromagnetic substances show spontaneous magnetization: that is all the magnetic moments in a microscopically large region called a domain are aligned at zero applied magnetic field. The application of an external field tends to enlarge the domains with magnetization direction close to the direction of the magnetic field minimizing in the same time, domain sizes (with not favorable orientations with respect to the field). Further increase of the magnetic field leads to the saturation magnetization which means that the individual magnetic moments lie in the direction of the field [8]. Upon removal of the field, a considerable fraction of the moments are still left aligned, giving a remanant magnetization which is more often than not very large. To gain more know-how on ferromagnetic materials, we have to understand what exchange (J_{ij}) and e.g., uniaxial anisotropic (K_{ij}) interactions between spins at site i and site j are commanded by the Hamiltonian

$$\mathcal{H} = - \sum_{\substack{i,j \\ i \neq j}} J_{ij} \vec{S}_i \cdot \vec{S}_j + \sum_{i,j} K_{ij} S_i^z S_j^z$$

but unfortunately, these are beyond the scope of this research.

When a magnetic field is applied to a material that displays ferromagnetic behavior and the removed, the magnetization does not follow the initial magnetization curve and this gives rise to the hysteresis loop of the material (Figure 2.2). The limit of an extremely large applied field gives the “saturation magnetization”, when all domains are aligned parallel and pointing in the same direction as seen in the top right and bottom left diagram of the Figure 2.2. If the field is

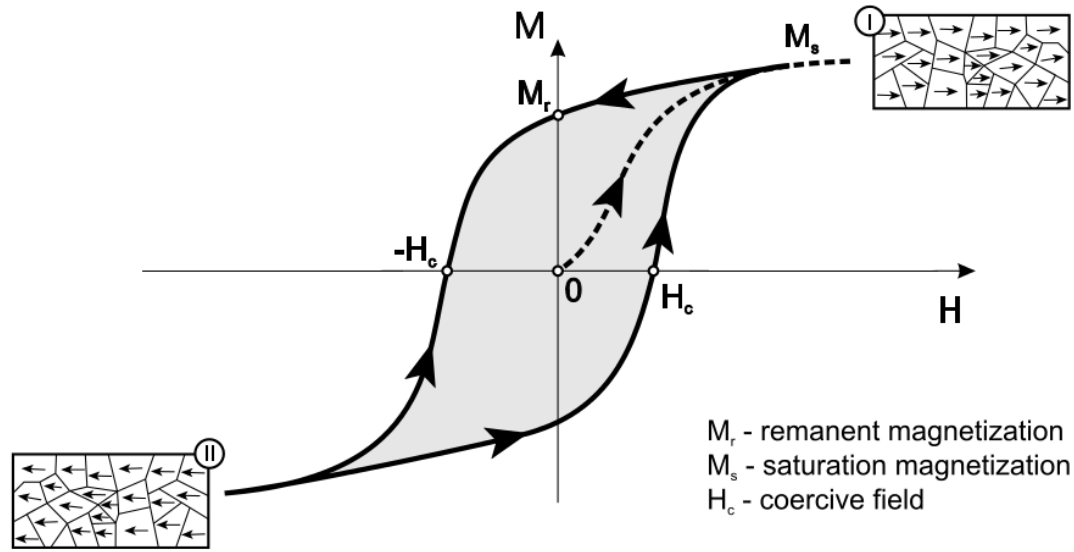


Figure 2.2: Magnetization vs. applied magnetic field for a ferromagnetic substance - Hysteresis arises from motion of domain walls. A large remanent magnetization when the field is zero is typical of a permanent magnet.

reduced to zero (zero applied field), the domains tend to remain oriented, leading to a “remanent magnetization” as the curve lags behind the original magnetization curve. If a field in the opposite direction is applied, then magnetization will reach a null point so that the magnetic domains are agglomerated into the domain wall and if the domain walls cannot move easily, then the “coercive field” H_c is large. As a result of the, sometimes complex, domain structure, the magnetization of a sample has a characteristic dependence upon applied magnetic field, as sketched in Figure 2.2. Symmetric behavior of the hysteresis curve is obtained as the magnetic field is varied between large positive and negative magnitudes. The area enclosed by the loop is the magnetic energy that is dissipated while circling the loop.

The statement that a ferromagnetic substance can behave as a paramagnetic material is highly dependent on the temperature of the system. The Curie temperature (T_c) is the temperature at which a ferromagnetic material transitions into a paramagnetic material by losing long-range order. This second-order phase transition is the result of zero spontaneous magnetization and infinite sus-

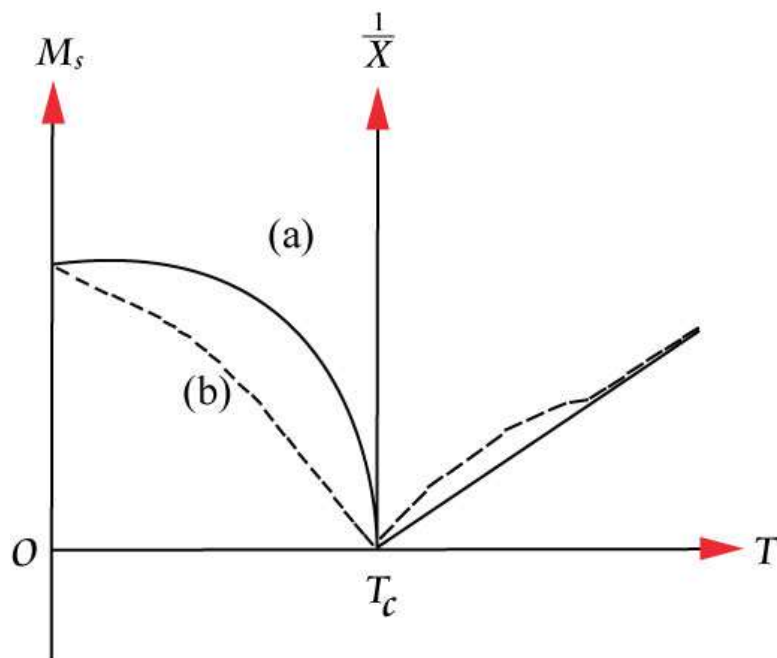


Figure 2.3: Magnetization vs. temperature for a ferromagnetic substance - Theoretical (a) and experimental (b) variation of saturation magnetization below, and reciprocal susceptibility above Curie temperature T_c for a ferromagnetic. Adapted from J. Bland Thesis M. Phys (Hons): 'A Mossbauer spectroscopy and magnetometry study of magnetic multilayers and oxides.' Oliver Lodge Labs, Dept. Physics, University of Liverpool.

ceptibility [10]. From an atomic point of view, when approaching T_c , there is a decrease in the magnetization of the domain for the ferromagnetic material. Above T_c , the material is paramagnetic so that magnetic moments are in a completely disordered state. A sketch of this transition is shown in Figure 2.3. In this figure, (a) represents the theoretical prediction while (b) shows the experimental values of the saturation magnetization and inverse susceptibility. At absolute zero temperature, all the magnetic moments are frozen in a specific orientation so that the magnetization is saturated and as the temperature is increased, the overall magnetization decreases until it reaches zero at T_c . Above T_c , the inverse susceptibility increases linearly (c.f. Figure 2.3 or Eq. 2.9).

2.4.3.1 Magnetic Anisotropy

Magnetic anisotropy is the property of a material that depends on the direction of the crystallographic structure. The anisotropy is playing the most effective role in a magnetic field whereby a magnetically anisotropic material will align its magnetic moment with an axis that is energetically favorable called the easy axis. There are several causes from which anisotropy may occur, but the most common ones will be discussed: magneto-crystalline anisotropy and shape anisotropy.

In magneto-crystalline anisotropy, magnetization changes differently for different crystallographic directions. Thus, certain crystallographic directions are preferred directions, or easy axes, for the spontaneous magnetization. The spin-orbit interaction is the primary source of the magneto-crystalline anisotropy. An example of magneto-crystalline anisotropy is shown in Figure 2.4 where [111] is the easy axis while [100] is the hard axis. This was verified by experimenting on magnetite and the result shows that when magnetized along the easy axis, saturation magnetization is reached faster than when magnetized along the hard direction.

In shape anisotropy, when a sample is not perfectly spherical, it will be easier to magnetize it along a long axis than along a short axis. The reason for this is the demagnetizing field which is stronger along a short axis than along a long axis. The applied field along a short axis then has to be stronger to produce the same

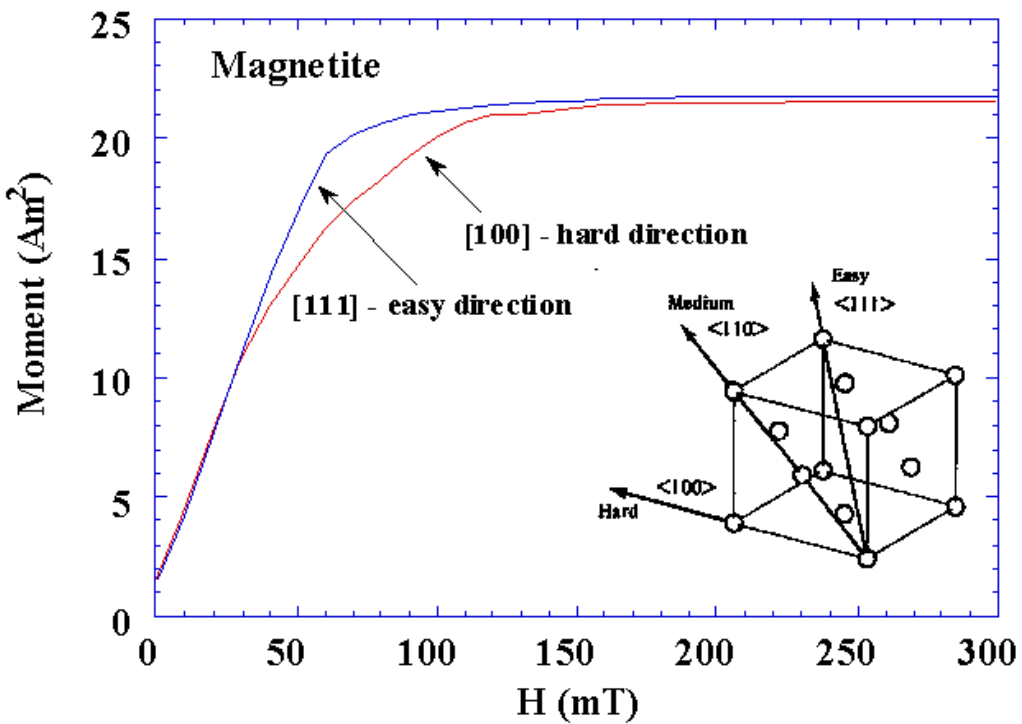


Figure 2.4: Magneto-crystalline anisotropy - Change in the saturation magnetization with the easy and hard axis of magnetite as a function of applied field. Taken from Hitchhiker's Guide to Magnetism written by Bruce M. Moskowitz for the Environmental Magnetism Workshop.

saturation magnetization inside the specimen. Hence shape anisotropy becomes important in thin films and often produces in-plane alignment of moments [10].

2.4.3.2 Domain Structure

If significant number of the magnetic moments pointing in the same respective direction in a ferromagnetic material are grouped together, then a magnetic domain is generated. In each domain, all of the atomic dipoles are coupled together in a specific direction. The domains can be considered as small magnets within a material. Ferromagnetic materials have the tendency to minimize the energy of the system and to do so, they are inclined to break up into domains that align themselves in such a manner as to minimize the overall energy of the material. Hence, a single domain can be broken into two smaller oppositely aligned domains in a hexagonal crystal as shown in Figure 2.5 and this process continues until breaking into more domains does not have any favorable decrease in energy because the transition region between domains, or domain wall, requires energy to be produced and maintained. The splitting of the domain can also occur in a cubic crystal whereby instead of being oppositely aligned, the domains are perpendicular to each other following directions of easy axes. This has the same effect of minimizing the energy of the system.

In between domain walls, the magnetization revolves by 90° or 180° depending on the crystallographic structure or easy axis in different directions. Again, this happens because the abrupt change in the magnetic moment directions are unfavorable and the wall allows the 90° or 180° difference in spin alignments between domains to be shared by many magnetic moments. In Figure 2.5, the domains are in different direction but in reality, the domains flips by discrete angles in a very small region known as domain walls. A magnified picture of a domain wall is shown in Figure 2.6. Domain walls have a finite width that is determined principally by a competition between anisotropy and exchange interaction.

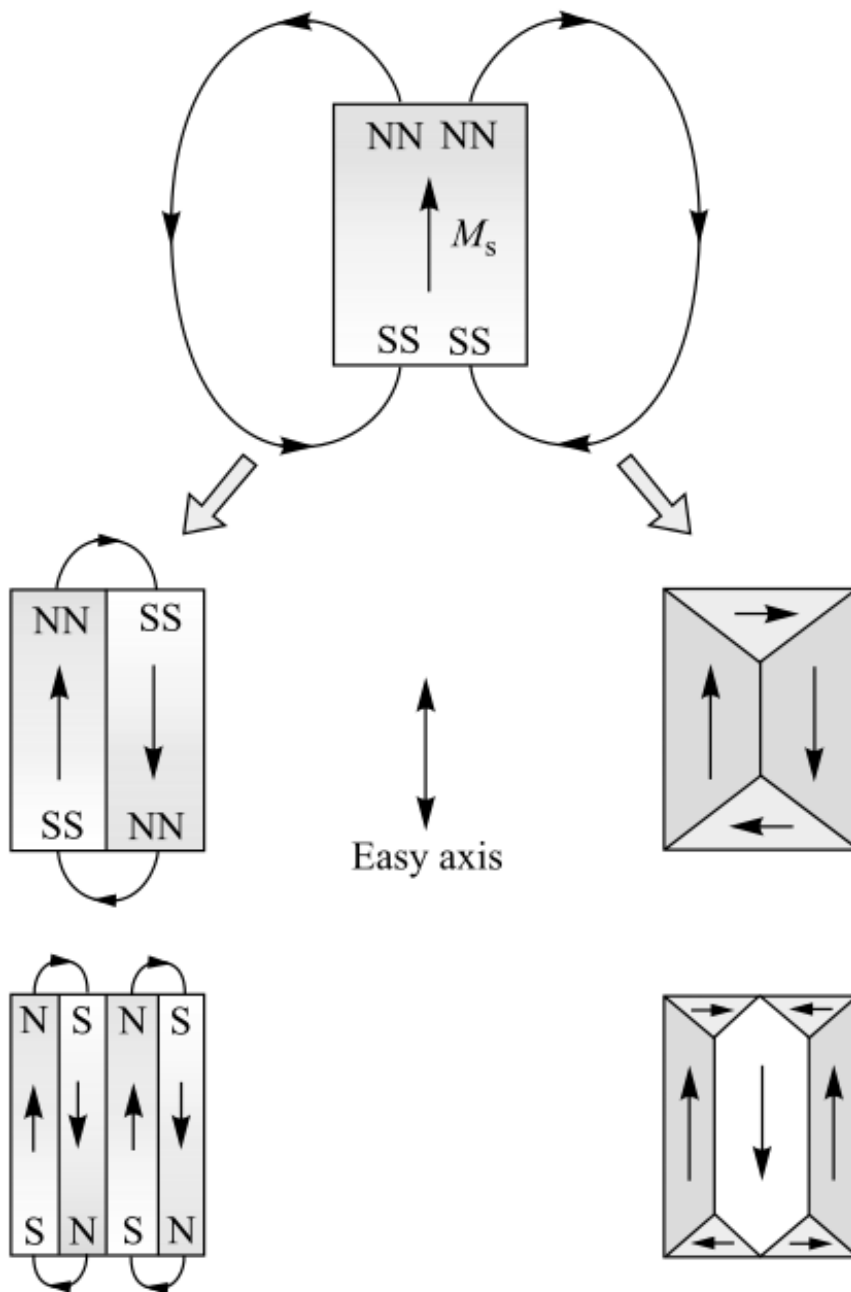


Figure 2.5: Decrease of magnetic energy by domain splitting - Domain creation and the associated demagnetizing field for both hexagonal and cubic crystals. The external field decreases (magnetic lines of force are shortened), and hence the demagnetizing energy decreases, as the system breaks into domains.

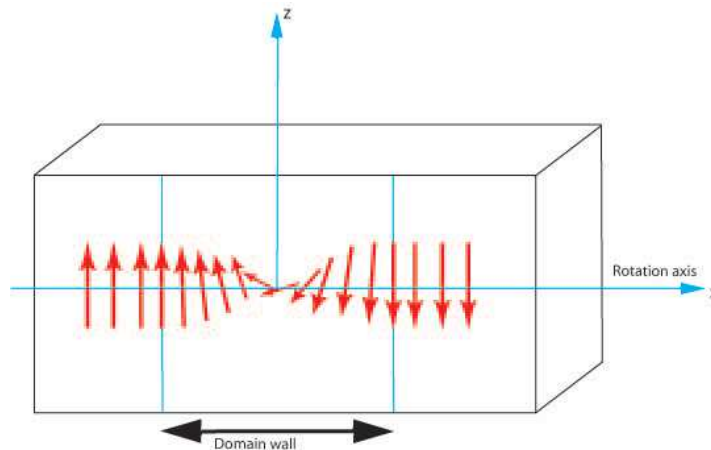


Figure 2.6: Domain wall - The rotation of magnetic moments through a 180° domain wall.

2.5 Nanomagnetism

Nanomaterials just like their bulk counterparts shows magnetic behavior. However, because of the magnitude of their size, they show behavior which are beyond the traditional magnetism realm.

2.5.1 Single-Domain Particles

Bulk ferromagnetic materials tend to break up into several domains in order to decrease the overall magnetic energy of the system. This is not often the case for nano-scale materials because their sizes are comparable to the minimum domain size and can no longer accommodate a wall. Henceforth, in single-domain particles, the magnetization stays constant across the magnet because of the single magnetic domain and the strongly coupled magnetic moments of each atom combine cooperatively to give rise to a system with a single “giant” magnetic moment. A sample transitions from multi-domains to single-domain at the critical size which depends on the saturation magnetization and the domain wall energy per unit area. Although there are theoretical calculations to estimate the critical size of a nanoparticle, the most reliable determination of this size is by experimenting on the sample.

2.5.1.1 Coercivity of Single-Domain Particles

The magnetization at any point in a single-domain ferromagnet must occur via spin rotation due to the fact that there are no domain walls to displace. In a multi-domain system, the domain walls move easily within a magnetic material and consequently have a low coercivity. By contrast, single-domain particles have a larger coercivity compared to multi-domain systems because, it is harder to flip the magnetization than to move a domain wall [11]. For a single domain spherical nanoparticle, the magnetization reversal occurs through the coherent rotation of magnetization associated with a square hysteresis loop [12].

For a chain composed of a number of single domain spherical nanoparticles, the magnetization reversal is modified to curling and fanning modes due to the exchange and magnetostatic interactions between the particles [13].

Fanning prevails in chains of particles or highly elongated particles. In these set-ups, the saturation magnetization vector of each particle interacts with its neighbors via the magnetic bipolar interaction. Thus the dipoles line up, north to south, and like to remain in alignment, hence causing an anisotropy even if no others exist. Applying a field in the other direction tends to reorient these dipoles, but the re-orientation may occur either coherently or (fanning) incoherently [14] as in Figure 2.7. When the re-orientation occur incoherently, the magnetic moments are pointing in different directions in adjacent particles. If the process is not fanning, then all the moments are displacing in the same direction.

Curling is the other mechanism by which single domain particles can change their magnetization directions. Initially the magnetization of a particle is out of and normal to the page. Then a magnetic field is applied into and normal to the page (z-axis) in the opposite direction to magnetization (with each single atomic magnetic moment considered). The coherent (a) and curling (b) responses are illustrated in Figure 2.8. As the total saturation magnetization turns to reverse, the atomic magnetic moments could either stay parallel so that their x-y components are equal (coherent rotation) or they could rotate away from the z-axis with different x-y components. If these x-y components are always perpendicular to a radius vector in the xy plane, curling takes place. It is common

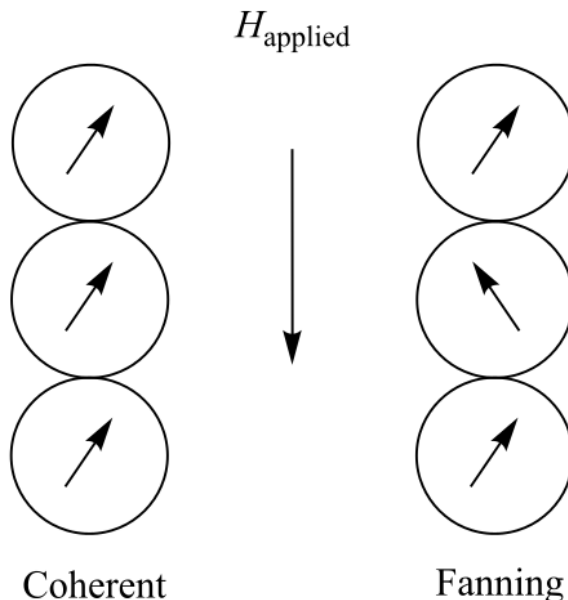


Figure 2.7: Fanning mechanism - Coherent and fanning rotation of magnetization in particles, initially upward, with an applied field in the downward direction.

for small particles to reverse coherently, whereas large particles use curling [14].

2.5.2 Superparamagnetism

Superparamagnetism (SP or SPM) describes the state of a uni-axial, single-domain particle when thermal energy is sufficient to overcome energy barriers (arising from magneto-crystalline, magneto-elastic and/or shape anisotropy) to a reversal of magnetization [15]. When the energy barriers are relatively low, thermal excitations can result in reversal of the magnetization over very short time scales, and the particle is in a superparamagnetic state. The magnetization behavior of single domain particles in superparamagnetic regime is identical with that of atomic paramagnetic except that very large magnetic moments are involved and hence the term superparamagnetism [16].

The anisotropy energy of a single-domain particle is proportional, in a first approximation, to its volume, V . For most simple case of the uni-axial anisotropy, the associated energy barrier E_b , separating easy magnetization directions, is

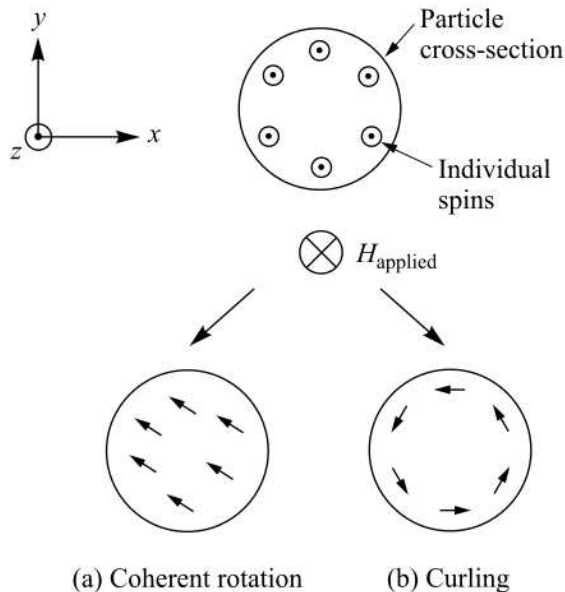


Figure 2.8: Curling mechanism - Comparison of coherent and curling rotation of particle magnetization due to an applied field. Particle cross-sections are shown.

proportional to KV , where K is the magnetic anisotropy energy density.

$$E_b = KV \sin^2 \theta \quad (2.11)$$

Figure 2.9 shows the variation of the angle θ of the magnetization relative to a preferred direction (horizontal in our case) with the energy of the system. The energy is zero when the magnetization is pointing either to the right or left and is maximum when the angle is 90° . The energy barrier is the energy difference between the two perpendicular angles.

With decreasing particle size, the anisotropy energy decreases, and for a particle size lower than a particular value, it may become so low as to be comparable to or lower than the thermal energy $k_B T$ at room temperature. This implies that the energy barrier for magnetization reversal may be overcome, and then the total magnetic moment of the particle can thermally fluctuate, like a single atomic magnetic moment in a paramagnetic material. This leads to a spontaneous random orientation of the magnetic moment inside the particles, or in other words, the remanent magnetization as well as the coercivity will be zero. This means

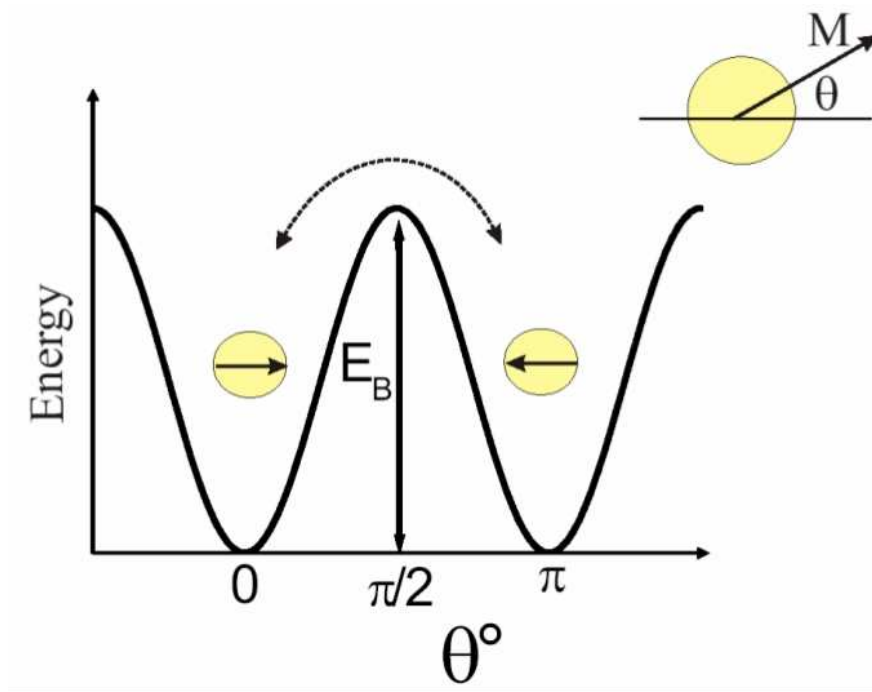


Figure 2.9: Energy of a superparamagnetic particle - The energy of a particle with uni-axial anisotropy as a function of magnetization direction. E_b , the energy barrier, is needed for the rotation of the magnetization and θ is the angle between the magnetization M and the preferred direction (easy axis).

no hysteresis and therefore superparamagnetic behavior [17] as shown in Figure 2.10 for superparamagnetic magnetite (diameter: 7.5 nm).

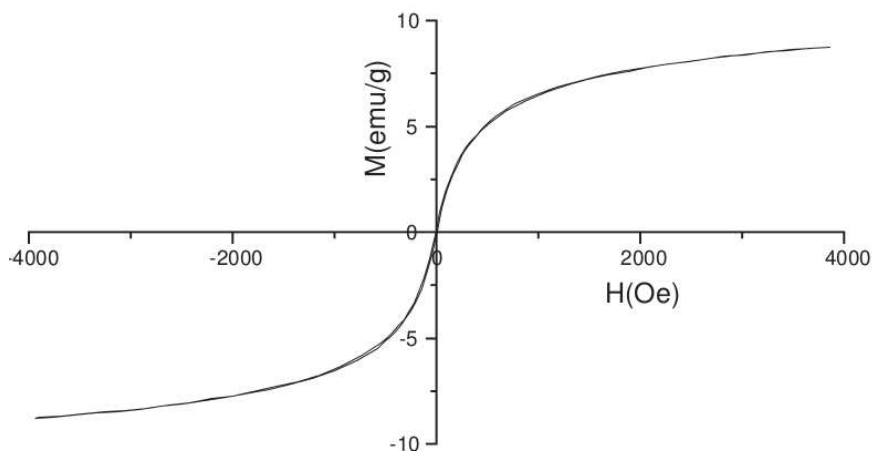


Figure 2.10: Hysteresis loop of superparamagnetic particle - The hysteresis loop of magnetite particles with a diameter of 7.5 nm which is in the superparamagnetic regime for magnetite. Adapted from [18].

This can be made quantitative by introducing an attempt timescale τ_o characteristic of the material, which describes the timescale over which nanoparticle's magnetization attempts to jump the KV barrier. Then the timescale for a successful jump is τ_N to describe a random flip due to thermal fluctuations.

The total magnetic moment of the particle may be freely rotated, whereas the moments within the particle remain coupled ferromagnetically. In that case, an assembly of nanoparticles can quickly approach to thermal equilibrium if the external magnetic field or temperature changes. The actual magnetic behavior of nanoparticle assemble depends highly on time. In case of non-interacting single-domain nanoparticles with the uniaxial magnetic symmetry, the relaxation time τ_N [19]) is given by the Neel-Arrhenius law [20]:

$$\tau = \tau_o \exp\left(\frac{E_b}{k_B T}\right) = \tau_o \exp\left(\frac{KV}{k_B T}\right) \quad (2.12)$$

where τ_o is the characteristic time and is usually in the order of 10^{-9} s. Taking value of $\tau_N = \tau_m = 100$ s (measurement time) and $\tau_o = 10^{-9}$ s, one can obtain

some interesting properties.

$$100 = 10^{-9} \exp\left(\frac{E_b}{k_B T_B}\right) \quad (2.13)$$

$$25.32 = \frac{KV}{k_B T_B} \quad (2.14)$$

$$V = 25.32 \frac{k_B T_B}{K} \quad (2.15)$$

A particle with volume smaller than this acts superparamagnetically on the 100 s experimental timescale.

If $\tau_m \gg \tau_N$ the relaxation is faster than the magnetization orientation observed in this time window, allowing the system to reach thermodynamical equilibrium. The nanoparticles are considered to be in the superparamagnetic regime. On the other hand, if $\tau_N \gg \tau_m$, the system relaxation proceeds very slowly, and one can observe quasi-static properties as in ordered magnetic systems. Such nanoparticles are in the so-called blocked regime. The temperature that divides both regimes is called blocking temperature T_B , and depends on the characteristic measuring time τ_m (defined by $\tau_m = \tau_N$). T_B is associated to the energy barrier and for this reason it increases with particle size. The critical volume for superparamagnetism is directly proportional to the temperature, i.e., the higher the temperature, the higher the critical size of the particles; all particles which are smaller than the critical size are in the superparamagnetic regime, i.e., if the system has a grain size distribution, when temperature is increased, more particles fall into the superparamagnetic regime. From Eq. 2.15 one sees that the blocking temperature is directly proportional to the volume of the particles and its anisotropy constant. In other words, the bigger particles become superparamagnetic at higher temperatures [21].

2.5.2.1 ZFC-FC Measurement

To get the mean blocking temperature experimentally, a special set of procedures has to be followed: zero field-cooling (ZFC) and field-cooling (FC) measurements.

The ZFC magnetization curve is typically obtained by cooling in zero field from a high temperature where all particles show superparamagnetic behavior to a low temperature and continuously measuring the effects of the field as the temperature is raised to a level well above the blocking level. The temperature raise is done in a small applied field. At each temperature, measurements are taken after time τ_m . The FC magnetization curve is typically obtained by applying the magnetic field at a relatively high temperature compared to the blocking temperature and continuously measuring the effects of the field as you lower the temperature in the same small applied field after waiting τ_m to a level well below the blocking level [22].

Distinct features of a ZFC/FC measurement are a peak of the ZFC magnetization curve and that the ZFC and FC magnetization curves coincide at high temperatures but split at a temperature which is slightly less than the blocking temperature at which the relaxation time of the largest particles becomes comparable to $\tau_m \approx \tau_N$. Yi Liu et al. [23] believe that the peak in the FC curve is due to the “quench” effect while the sample is cooling down. When the temperature is just slightly below T_B , the magnetizations of the particles are fixed in their directions (‘up’ or ‘down’). ZFC curves shows that the blocking temperature T_B shifts to lower temperatures with increasing applied magnetic field, which is accounted for the reduction in the barrier energy. If the temperature decreases slowly, the FC curve should follow the Curie law. With increasing magnetic field, the peak becomes smaller and finally disappears. This is because with increasing the field, the relaxation rate becomes much larger due to the reduction in energy and the system can reach a state much nearer the equilibrium. Above the blocking temperature, ZFC and FC magnetization data follow the Curie law at a low field, but show non Curie law behaviour at higher fields. A theoretical approach to the blocking temperature is performed by Hansen et al. [24] in their paper entitled “Estimation of blocking temperatures from ZFC/FC curves”. They have successfully estimated the blocking temperature and compared it to the experimental values which agrees to a very high extent as illustrated in Figure 2.11. The figure shows the temperature dependence of magnetization and shows the experiments performed when the sample (manganese) is cooling/warming under different fields (zero or a low field).

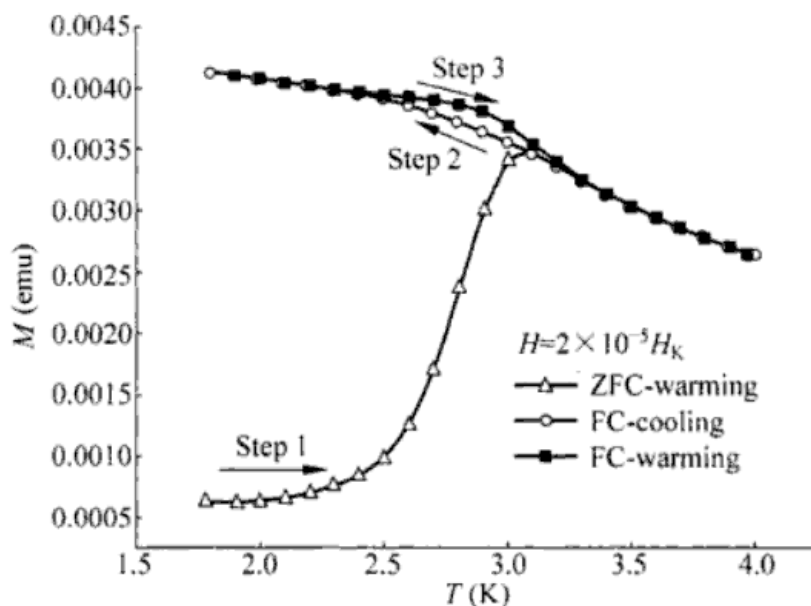


Figure 2.11: ZFC-FC measurements - The temperature dependent magnetization of manganese to show the zero field-cooling and field-cooling effects. Taken from [23].

2.6 Summary of Chapter 2

As the introduction to this chapter, the governing equations relating electricity and magnetism are explained briefly. Magnetism, at the atomic level is ruled by the laws quantum mechanics. This gives rise to a magnetic field which indeed is the result of the motion of electric charges. The motion can be in the form of the orbital motion of the electron or the spin of the electron. Material-wise, there are several kinds amongst which are ferromagnetic, paramagnetic and diamagnetic materials.

Diamagnetic substances are repelled by a magnetic field and this is given by the negative magnetic susceptibility which is the effectiveness of an applied field for inducing a magnetic dipole.

The susceptibility is positive and very close to zero for paramagnetic materials. This means that there is a weak interaction between a material and a magnetic field. Ultimately, the interaction is strongly attractive towards a magnetic pole for ferromagnetic materials since they have very large and positive magnetic susceptibilities. Just like paramagnetic material, properties of ferromagnetic materials

are highly dependent on temperature.

Ferromagnetic materials are known for their resistive behavior when a field is applied and then reversed. This is characterized by a hysteresis loop which is specific to each material. A ferromagnetic will transform into a paramagnetic substance on increasing temperature above a critical temperature called the Curie temperature. The magnetic anisotropy which is direction dependence of the magnetization is elaborated. Finally, the domain structure is illustrated by describing how there is a mechanism inherent in the substance to minimize energy of the overall system by breaking into domains.

Changing from bulk material to nanomaterial, the high coercivities of single domain particles are described. In the same line, coherent (regular), fanning and curling processes are explained. In Figure 2.12, the hysteresis loops of a paramagnetic material, ferromagnetic and superparamagnetic material is shown. We can deduce from the figure that the remanent magnetization of both superparamagnetic and paramagnetic materials is zero meaning that there is no energy loss when the magnetic field is reversed. The saturation magnetization for the different systems should also be noted (ferromagnetism and superparamagnetism displays around the same saturation magnetization while the latter is much smaller for paramagnetism).

A large section of the chapter is devoted to superparamagnetism. Superparamagnetism occurs when thermal energy of the material overpowers the energy barrier and over a very short time scale, the magnetization is reversed. Also, superparamagnetism is a size phenomenon and the relevant equations have been derived. This is summarized in Figure 2.13 where below a certain threshold particle size (usually between 2-10 nm), a zero coercive force prevails (superparamagnetism). Above this threshold, single-domain or multi-domain systems are present depending on the size. D_c is the size where a particle changes from single domain to multi-domain. We can also see from the same figure how the width of the hysteresis loops decreases when transitioning from single-domain to multi-domain systems.

Superparamagnetic substances are interesting for their high saturation magnetization and zero remanent magnetization. Quasi-static properties can be ob-

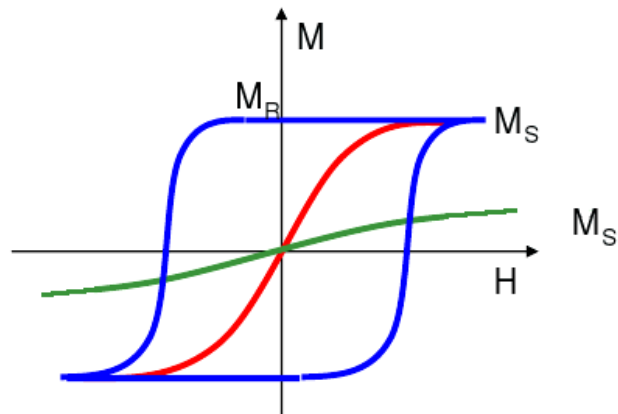


Figure 2.12: Hysteresis loops for paramagnetic, ferromagnetic and superparamagnetic materials - Figure interlaces paramagnetic (green), ferromagnetic (blue) and superparamagnetic (red) hysteresis loops into one figure to show the difference in remanent magnetization, coercive field and saturation magnetization.

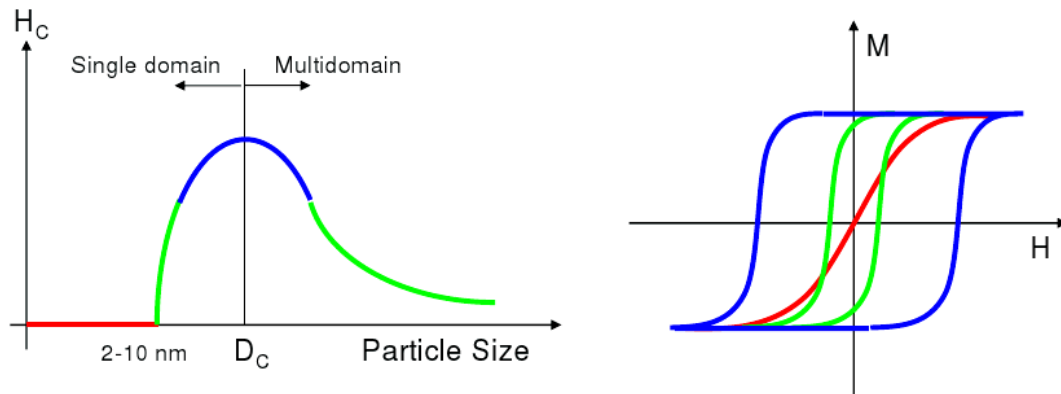


Figure 2.13: Size effect on ferromagnetic/superparamagnetic particles - Ferromagnetic grains undergoes a change from multi-domain to single domain particles and further reduction in the size modifies their behavior from ferromagnetic to superparamagnetic. The corresponding hysteresis loop is drawn on the right. The red curve corresponds to superparamagnetic while the blue/green curves are ferromagnetic.

served (blocked system) depending on the magnetization relaxation time. There are a couple novel happenings because of this blocked state of the nanoparticles. The critical factor is the blocking temperature and this can be determined experimentally by performing the zero field-cooling and field-cooling measurements.

Now that the foundations have been laid, we can proceed with the next chapter which is purely on the heating mechanisms that prevail in different types of nanoparticles.

CHAPTER 3

Magnetic Heating

When magnetic particles are irradiated with an alternating electromagnetic field, the particles transform the energy of the AC field into heat by several physical mechanisms, and transformation efficiency strongly depends on the frequency of the external field as well as the physical characteristics of the particles such as particle size and surface modification [25]. In this chapter, the different processes of magnetization reversal in the particle system by which the latter heat up will be elaborated.

3.1 Hysteresis

All ferromagnets are characterized by their corresponding hysteresis curves. As has been described in Chapter 2, if the magnetic field applied to a ferromagnetic material is increased and then decreased back to its initial value, the magnetic field inside the material does not return to its original value but ‘lags’ behind the external field. This behavior results in a loss of energy, called the hysteresis loss, when a sample is repeatedly magnetized and demagnetized. To understand this at a deeper level, we refer to Figure 3.1 where the energy to magnetize and demagnetize a ferromagnetic sample is shown. The overall energy lost will be the area enclosed by the curve and the positive H-axis. We can go one step further and infer that the total energy lost over one complete cycle is proportional to the

area within the hysteresis loop.

Repeated magnetization and demagnetization of a sample results in a loss of

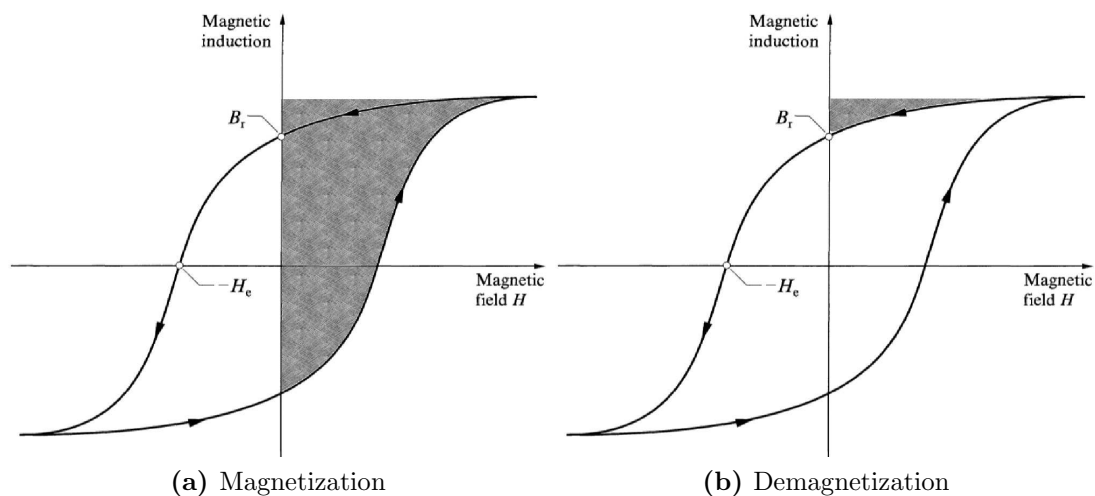


Figure 3.1: Magnetizing and demagnetizing of ferromagnets - Figure (a) shows the energy to establish the field while figure (b) shows the energy released by the collapse of the field.

energy, called the hysteresis loss [26]. Hysteresis losses may be determined by integrating the area of hysteresis loops, a measure of energy dissipated per cycle of magnetization reversal [27, 28].

The area of a hysteresis loop

$$E_{hyst} = \oint HdB = \mu_o \oint HdM = -\mu_o \oint MdH \quad (3.1)$$

$$\text{since } B = \mu_o(H + M) \quad (3.2)$$

corresponds to the energy density loss in magnetization of the demagnetized material.

E_{hyst} corresponds to the energy when a material is magnetized till saturation in one direction, demagnetized and finally magnetized again in the opposite direction. If this process is repeated f times in one second, then instead of the

energy, we will have the corresponding hysteresis power loss [29, 30] in a material with frequency f is

$$P_{hyst} = \mu_o f \oint H dM = -\mu_o f \oint M dH \quad (3.3)$$

$$P_{hyst} = f \oint H dB \quad (3.4)$$

3.2 Neel and Brown Relaxation

When the particle size decreases until the thermal energy takes over the energy barrier, the particle is in the superparamagnetic regime. When this happens, the particle relaxes over a very short period of time given by:

$$\tau_N = \tau_o \exp\left(\frac{KV}{k_B T}\right). \quad (3.5)$$

The relaxation effects cause the remanent magnetization, coercive forces and hysteresis to disappear below a critical size where superparamagnetism prevails. The transition to superparamagnetism occurs in a narrow frequency range and consequently, a particle can show superparamagnetism behavior in low frequency and ferromagnetic behavior at high frequencies [31].

If magnetic particles are suspended in a fluid characterized by a viscosity η , an extra relaxation mechanism takes place due to reorientation of the whole particle which is commonly referred to as Brown relaxation with the characteristic relaxation time

$$\tau_B = \frac{4\pi\eta r_h^3}{k_B T} \quad (3.6)$$

with r_h as the hydrodynamic radius [32]. The reciprocal of Neel relaxation time and Brown relaxation time can be summed algebraically [33] as a total frequency

f_{total} .

$$f_{total} = f_N + f_B \quad (3.7)$$

$$\frac{1}{\tau_{total}} = \frac{1}{\tau_N} + \frac{1}{\tau_B} \quad (3.8)$$

$$\tau_{total} = \frac{\tau_N \tau_B}{\tau_N + \tau_B} \quad (3.9)$$

Landau and Lifschitz in his book “Electrodynamics of Continuous Media” (course of Theoretical Physics, Volume 8) give detailed derivation of the power loss density (W/m³) in an alternating magnetic field of small amplitude within the validity of linear response [34]. It is convenient to express the magnetization response as a complex susceptibility. If the applied magnetic field is sinusoidal $H(t) = H_o \cos \omega t = \Re \{H_o e^{i\omega t}\}$ and $M(t) = \chi H(t)$ then $M(t) = \Re \{\chi H_o e^{i\omega t}\} = \Re \{(\chi' - i\chi'')H_o(\cos \omega t + i\sin \omega t)\} = H_o(\chi' \cos \omega t + \chi'' \sin \omega t)$.

It is obvious that χ' is the in-phase component while χ'' is the out-of-phase component. From the field dependence we have $dH(t) = -H_o \omega \sin \omega t dt$, so changing the variable to t in Eq. 3.3 and substituting $M(t)$, we have

$$P_{super} = \mu_o f \omega H_o^2 \chi'' \int_0^{\frac{2\pi}{\omega}} \sin^2(\omega t) dt \quad (3.10)$$

$$= \mu_o \pi \chi'' H_o^2 f \quad (3.11)$$

where χ'' is the imaginary part of the susceptibility given in the first approximation

$$\chi = \chi' - i\chi'' \quad (3.12)$$

$$\chi' = \frac{\chi_o}{1 + \phi^2}, \chi'' = \frac{\chi_o \phi}{1 + \phi^2} \quad (3.13)$$

$$\phi = f \tau_{N/B} \quad (3.14)$$

$$\chi_o = \frac{\mu_o M_s^2 V}{k_B T}. \quad (3.15)$$

The frequency dependence of relaxation of the particle ensemble may be well investigated experimentally by measuring spectra of the complex susceptibility.

From these equations at low frequencies ($\phi \ll 1$), i.e., in the superparamagnetic regime, losses increase with the square of frequency as

$$P_{super} = \mu_o \pi \chi_o H_o^2 f^2 \tau_{N/B} \quad (3.16)$$

while for $\phi \gg 1$ losses reach a plateau (frequency independent) given by

$$P_{super} = \frac{\mu_o \pi H_o^2 \chi_o}{\tau_{N/B}} \quad (3.17)$$

The strong size dependence of the relaxation times leads to a very sharp maximum of the loss power density in dependence on particle size [35]. Hence, a very high heat loss occurs only for particle systems with a very narrow size distribution (and anisotropy) with the mean diameter being well adjusted in relation to the driving frequency, f .

3.3 Frictional Losses

On top of the losses caused by the relaxation, the Brown mechanism has another heating effect: friction between rotating particles and surrounding medium. In principle, magnetic particles with remanent magnetization (M_r) and volume (V) are capable of a magnetic torque moment, τ

$$\tau = \mu_o M_r H V \quad (3.18)$$

when exposed to an alternating magnetic field. In the steady state the viscous drag in the liquid $12\pi\eta V f$ is counteracted by the magnetic torque and the loss energy per cycle (E_{fric}) is [31] given by

$$E_{fric} = 2\pi(\text{Torque}) \quad (3.19)$$

The power loss (P_{fric}) due to the alternating field at a frequency f can then be given as

$$P_{fric} = 2\pi f(\text{Torque}) = \omega(\text{Torque}) \quad (3.20)$$

This loss type is not restricted to superparamagnetic particles but all magnetic particles subjected to a magnetic field [36].

3.4 Chapter Summary

This chapter elucidates the different heating mechanisms in particles when subjected to an alternating magnetic field.

Firstly, hysteresis losses which is nothing more than the closed path integration of the B-H curve for one cycle of a ferromagnetic sample and it grows proportionally to the driving frequency of the magnetic field. The higher the frequency and the magnetic field, the higher will be the hysteresis loss of the particle being subjected to the oscillating field.

Secondly, there are losses due to the Neel and Brown relaxation which are typical to superparamagnetic particles. This happens when the thermal energy overcomes the energy barrier and the magnetization can change direction over a very short time period. The power loss in this regime depends on the complex susceptibility, the magnetic field and the frequency. This power follows a maxima which happens at very specific diameter of the particle and its anisotropy.

Finally, there is the viscous losses which is another effect of the Brown relaxation. The heating losses are caused by the torque of (superpara/ferro/para) magnetic particles in an alternating magnetic field. This effect is highly dependent on the viscosity of the liquid in which the sample is placed. Highly viscous solutions will produce very high heating effects.

CHAPTER 4

AMF System

In the previous chapter, we have encountered the different heating mechanisms of magnetic particles when interacted upon by a time-varying field. Hitherto, only the theoretical aspect has been considered and an experimental procedure has to be devised in order to test the experimental settings. In this chapter, we are going set the blueprint to create the essential equipment to test nanoparticles.

4.1 Specific Power Loss

Before the design of the adequate equipment, we first need to point out the different variables that are going to be involved. Since nanoparticles are going to be irradiated by a magnetic field, they are going to liberate heat to their surroundings. The easiest and most straight-forward methodology is to measure the temperature of the system. Notwithstanding different amount of nanoparticles will release different quantity of heat to the environment. Unitizing the amount of nanoparticle will eliminate the ‘quantity’ issue. Of late, many publications [37] have coined the term specific power loss (SPL), or more commonly known as specific absorption rate (SAR) in the medical field. SPL is the standard measure of the heating performance of magnetic nanoparticles and as name might reflect, is the power per unit weight of nanoparticles. It can be accurately evinced by the

following calorimetric formula:

$$\Delta Q = mc\Delta T \text{ and } P = \frac{\Delta Q}{\Delta t} \quad (4.1)$$

$$\therefore SPL = c \left(\frac{\Delta T}{\Delta t} \right) \quad (4.2)$$

where m is the mass of particle used and c is the specific heat capacity. These equations are valid if and only if there are only solid nanoparticles in the vessel. In case that a fluid is present in the container, for example a liquid, then we have to modify the equation to cater for the added substance. Equation 4.2 will become:

$$SPL = \frac{(m_l c_l + m_{NP} c_{NP})}{m_{NP}} \left(\frac{\Delta T}{\Delta t} \right) \quad (4.3)$$

where c_l is the specific heat capacity of the liquid, c_{NP} is the specific heat capacity of particles, m_l is the mass of liquid and m_{NP} is the mass of nanoparticles used. The specific absorption rate (SAR) is the quantity used to measure how much energy is actually absorbed in a human body. To illustrate, in the case of whole-body exposure, a standing human adult can absorb energy at a maximum rate when the frequency of the radiation is in the megahertz range, meaning that the whole-body SAR is at a maximum under these conditions (resonance).

4.2 Temperature Measurement

Temperature is the prime parameter in SPL determination and hence, it has to be determined to a high degree of precision and accuracy. On top of that, it should not have any effect on the medium whose temperature is being measured. Moreover, it should respond almost instantaneously and has a conditioned output.

4.2.1 Temperature Probes

Several known apparatuses (both electrical and non electrical) are available in today's world to measure the temperature and all the popular probes will be

listed along with their own advantages and drawbacks.

1. *Liquid-in-glass thermometer* is perhaps the most commonly known temperature device measurement that is known. It has several advantages that have made it so popular in the midst of experimental enthusiasts.

Advantage	Disadvantage
Uniform expansion	Slow response
Good conductor	One third immersion
High boiling point (Hg)	High freezing point (Hg)
Low freezing point (C_2H_5OH)	Low boiling point (C_2H_5OH)
	Wets the tube (C_2H_5OH)

2. *Thermocouple* is a device made-up of two different conductors that produce a voltage proportional to a temperature difference between two thermocouple junctions.

Advantage	Disadvantage
Large temperature range	Cold junction compensation
Compact in size	Non-linear change
Fast response time	Unstable output
Point sensing	
Rugged and durable	

3. *Resistance Temperature Detector (RTD)* are sensors used to measure temperature by correlating the resistance of the RTD element with temperature. They are also called platinum resistance thermometers because the raw material to fabricate them is platinum.

Advantage	Disadvantage
Highly accurate	Lead resistance error
Low drift	Low response time
Linear response	Vibration resistance
High range	Shock resistance

4. *Thermistor* is a type of resistor whose resistance varies according to its temperature. The resistance is measured by passing a small, measured direct current through it and measuring the voltage drop produced.

Advantage	Disadvantage
Sensitive and accurate	Small temperature range
Rugged design	Non-linear response
Flexible packages	Self-heating
Surface mount	

5. *Fiber Optics* is the next generation temperature measurement device. It uses either visible light or infrared rays to measure the temperature of the body [38].

Advantage	Disadvantage
Compact	Extremely high cost
Large range	Require a controller
Very sensitive	Not portable
Very Flexible	
Wide bandwidth	
Free from EMI	

6. *Optical Pyrometer* is a non-contacting temperature measuring device that measures thermal energy radiated from a hot object. It is usually used to measure the temperature of the surface of a very hot object. It is similar to IR thermometers.

Advantage	Disadvantage
Non-contact measurement	Low sensitivity
High temperature measurement	Poor response time
Wide bandwidth	Prone to systematic errors

4.2.2 Choice of Thermometer

The perfect thermometer is one having the following characteristics:

- zero heat capacity - the thermometer does not take or give in heat to the material, This means that the temperature of the material is intact (no effect on the material in terms of temperature).
- fast response - the temperature probe should measure exactly the temperature of the media without any time lag. This is specially useful if the temperature is changing at a fast pace.
- accurate and precise - the probe should be able to yield consistent measurements at all times (high accuracy). Also, it should measure to the nearest 0.1 K if not better (high precision).
- miniature size of sensor - the best temperature device should have a microscopic contact area. Being tiny, it can be inserted even if the apparatus does not support temperature sensing inherently.
- digital display - easy reading is a must in applications since many data points are required and reading manually can become tedious over time. Data logging is rendered possible if the temperature controller is electronic in nature.

Now that all our goals are set, we can examine the different thermometers and select the best one for our experiment.

The biggest concern is that the final apparatus would be creating magnetic fields changing over time ultimately, thence we cannot incorporate a magnetic material in our experiment other than the magnetic particles.

Table 4.1: Characteristics of thermometers - The thermometer type, the material from which the sensor is made, the classes of magnetic material and whether it can be a candidate for the AMF system.

Thermometer	Material	Magnetic Type	Candidate
Mercury-in-glass	Mercury	Diamagnetic	Yes
Alcohol-in-glass	Alcohol	Diamagnetic	Yes
Thermocouple (J)	Iron-Constantan [39]	Ferromagnetic	No
Thermocouple (K)	Chromel-Alumel [40]	Ferromagnetic	No
RTD	Platinum	Paramagnetic	No
Thermistor (NTC)	NiMnCoFe-oxide [41]	Paramagnetic	No
Thermistor (PTC)	BaTiO ₃ [42]	Paramagnetic	No
Fiber Optics	Glass	Diamagnetic	Yes
Optical Pyrometer	Si	Diamagnetic	Yes

Mostly all electric/electronic thermometers are eliminated in this set-up. Furthermore, we can eliminate the liquid-in-glass (mercury and alcohol) because of the size of their bulb and the fact that they have to be one-third immersed into the substance. A really large amount of nanoparticles (> 20 g) would be needed and this is not feasible. Also, they have to be read manually by looking at the meniscus. Although digital versions exist, they are not considered because the tip is usually made of a magnetic material rendering them inappropriate.

The choice of thermometers was boiled down to the optical pyrometer and fiber-optics probe. Although the portability and in-built data logger of the pyrometer was appealing, we have opted for the fiber-optics thermometer because of its superior precision, response and data-logging capabilities. Also, it is not safe for a person to be holding a pyrometer while an experiment involving high current.

4.2.3 FISO Inc. FOT-L Temperature Sensor

The FISO's FOT-L is our preferred fiber-optics temperature sensor. The sensor offers accuracy and reliability in extreme temperature and hostile environments. Fiber optic technology provides intrinsic immunity to EMI and RFI since the sensors are not electronically active and do not emit nor are they affected by any

type of EM radiation, whether it is microwave, RF, or NMR. Another important advantage of optical fibers is the capability it provides to produce miniature components without compromising the physical characteristics of the bulk material. Optical fiber is optimized in size to provide the smallest possible light path.

FISO's fiber optic temperature sensors provide accurate, stable, and repeatable measurements. The FOT-L temperature sensor has a Fabry-Prot cavity constituted by two optical fibers precisely assembled into a glass capillary. The cavity length changes with temperature variations due to differences in the coefficient of thermal expansion between optical fibers and the glass capillary. Such variations are proportional to temperature changes which are thus evaluated using a calibration factor. The temperature measurements are based on variations of the reflected light - when compared to the emitted light due to thermal expansion of the glass used within the sensor. Due to the incredibly small size of this sensor, the thermal inertia is virtually reduced to zero allowing ultra fast temperature monitoring [43]. Table 4.2 shows the specifications of the FOT-L probe given by FISO Inc. The temperature range, although small, is sufficient for our purpose as heating will commence at room temperature. The response time (0.5 s) is the maximum response time

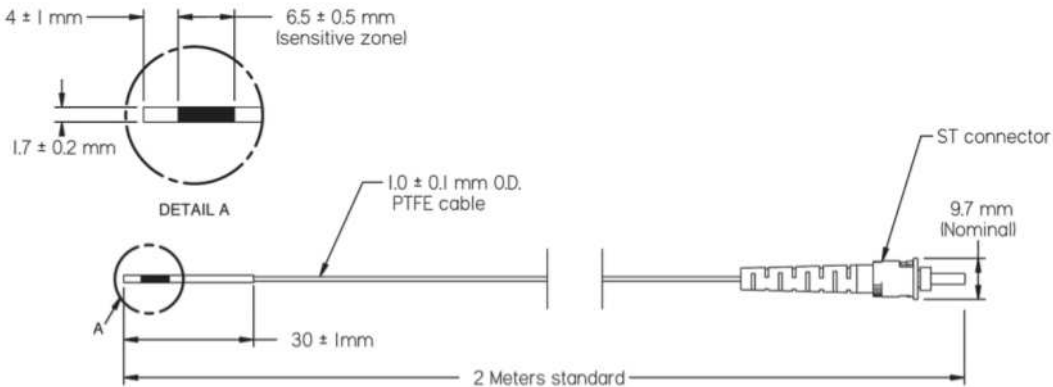
Table 4.2: Specifications of FOT-L - Characteristics of the FISO FOT-L temperature probe.

Specifications	
Temperature range	40°C to 250°C
Resolution	0.001°C
Accuracy	0.01°C
Response time	≤0.5 s
Connector type	ST connector

Furthermore, the fiber optic lead cable can be expanded to several meters long without affecting the quality or the accuracy of the results. Figure 4.1a is a picture of the actual probe while Figure 4.1b gives the actual dimensions. From the figures, we can see that the probe is extremely small and will fit any container with the sample.



(a) Temperature sensor



(b) Physical dimensions

Figure 4.1: FISO FOR-L - (a) The fiber-optics temperature probe, (b) the metric dimensions of the probe.

The bottom line is that FOT-L temperature sensors combine all the desired characteristics you would expect from the ideal sensor.

Chosen Temperature Sensor
Optical Fiber FOT-L Probe

4.3 Frequency of Operation

Whether ferromagnetic nanoparticles or superparamagnetic nanoparticles are used, we have to set a frequency of operation since both types of nanoparticle are directly dependent on the number of times the magnetic field is changing per second.

As long as the frequency is not 0 Hz, a magnetic material will heat up. Yet

concern that they may also have an effect on neurological function [47]. De Vocht et al., [48] consider the effect of switched gradient fields on cognitive function and used volunteers to assess their visual sensory (FACT) and visuo-motor (Pursuit Aiming II and visual tracking) neurobehavioral domains and the outcome was that there was a trend for visuo-motor accuracy to be reduced ($p=0.06$) by 1% during high exposure, but not at medium exposure.

There are well-known biophysical phenomena that lead to health problems as a result of exposure to sufficiently strong alternating magnetic fields [49]. The mechanism at low frequency ($f < 100$ kHz) is different from that at high frequency ($f > 100$ kHz). Since the operating frequency lies in the 3 Hz to 300 GHz range, it can unanimously be called radio frequency.

Low radio-frequencies are defined as frequencies between 300 Hz and 100 kHz. They involve two different mechanisms, namely induced currents and dielectric absorption. The cut-off frequency when one predominates over the other is not precisely defined. The existence of effects depend upon two superimposed phenomena: absorption of the external field in the organism at the macroscopic level and the stimulation of biological effects by the penetrating fields. Those two phenomena depend on the kind of field, electric or magnetic, and on the frequency.

For many years, it is known that exposure to very high levels of radiation from the high radio frequency oscillating field can cause a lot of damage due to the ability of the magnetic energy to heat biological tissue very rapidly. This is the thermal effect caused by high radio frequency fields. Heated tissues will eventually damage themselves during exposure to high RF levels because of the human body's inability to cope with or dissipate the excessive heat that could be generated. Two areas of the body, the eyes and the testes, are particularly vulnerable to heating because of the relative lack of available blood flow to dissipate the excessive heat load.

For low frequencies ($f < 100$ kHz) the mechanism is stimulation of nerve and muscle cells due to induced currents while, for higher frequencies ($f > 100$ kHz), tissue heating is the main mechanism. These mechanisms lead to acute effects

[50].

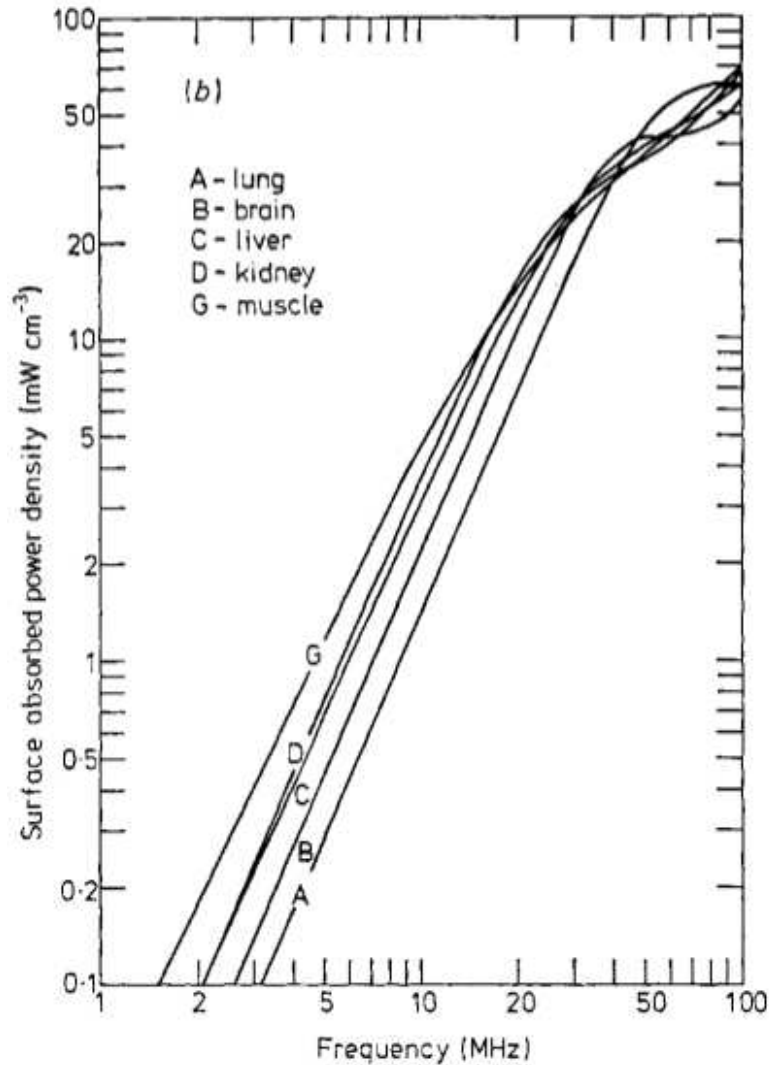


Figure 4.3: Power density - Absorbed power density at the surface of a 20 cm radius cylinder for biological tissues as a function of frequency.

As the peer-reviewed papers attest, it is safe to go up to a frequency of 100 kHz. Even so, another paper [51] tests how different frequencies (1-100 MHz) affect the tissue of rats in an NMR imaging experiment. It concludes that the surface power absorption operating at frequencies of 1, 2, 3, 4, 5, 10, 15, 20, 25, 30, 40, 50, 60, 70, 80, 90 and 100 MHz at 37 °C and 25 °C exceeds the maximum

recommended safe absorbed power density for long term human exposure of the order 1 mW/cm^3 at frequencies greater than about 5 MHz for the 20 cm radius tissue cylinders. This is also clearly shown in Figure 4.3 which is a plot of the absorbed power density against the frequency. At 1 MHz, from the graph, we can infer that the power density absorbed is going to be less than 0.1 mW/cm^3 providing that it follows the same trend.

There may be situations, particularly workplace environments near high-powered RF sources, where I strongly believe that a frequency between 100 kHz and 1 MHz is still safe to be used whereby the recommended limits for harmless exposure of human beings to RF energy is exceeded and this point will be considered while designing the apparatus.

Chosen Operating Frequency

$$100 \text{ kHz} < f < 500 \text{ kHz}$$

4.3.1 Magnetic Field

As we have seen in various sections of Chapter 2, a magnetic field is produced by electric charges in motion. This can be easily achieved by flowing a current in a wire. This will produce a circular magnetic field around the wire given by the expression

$$B = \frac{\mu_o I}{2\pi r} \quad (4.4)$$

where r is the distance from the wire to the point in consideration.

A single wire carrying an electric current is not very useful since whose the magnetic field strength is inversely proportional to the distance from the center of the wire. A constant magnetic field is more important in our case since a sample will be immersed in the field. Out of the numerous current-carrying devices that produces a constant magnetic field, the solenoid is the most fundamental one. A solenoid consists of wires wrapped around each other in such a way that it produces a constant magnetic field inside when an electric current is applied. The

magnetic field of an infinitely long solenoid is given by

$$\vec{B} = \frac{\mu_0 N I}{l} \hat{r} \quad (4.5)$$

where N is the number of turns of the coil, l is the length and \hat{r} is perpendicular to the coil.

The direction is given by the right-hand rule. A visual example is given by Figure 4.4. In this figure, the strength of the magnetic field is represented by the color of the lines. The highest field strength is white in color while the smallest field strength is blue. We can see that the field lines inside the solenoid is parallel (neglecting edge effects and wire proximity effects).

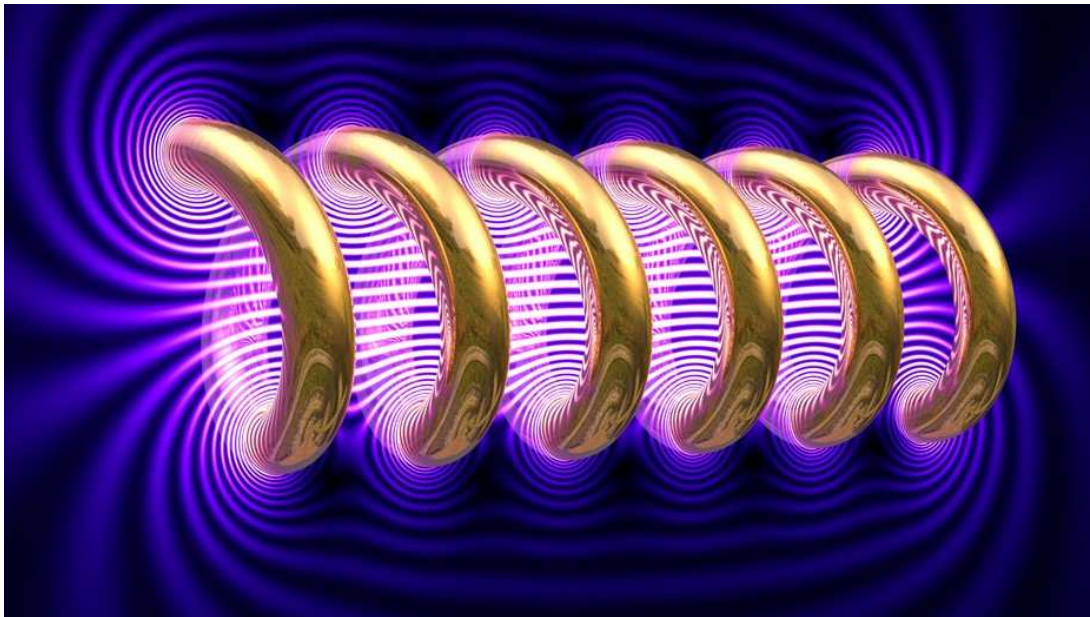


Figure 4.4: Magnetic field of solenoid - A 3D simulation of the magnetic field of a finite length solenoid by Paul Nylander.

4.3.1.1 Design of Coil

Although a regular solenoid would be perfect, it is not convenient for our use because of the heat generated by firstly, the high current that will flow in the wires and secondly, the oscillating magnetic field at a frequency exceeding 100 kHz. The

heat will possibly damage the wires if a regular solenoid is made. Therefore, we have to resort to a special design of the coil that will not be affected by the heat released in the coil. Our custom coil consists of insulated copper sheets wrapped around each other 20 times in the form of a spiral as shown in Figure 4.3.1.1.

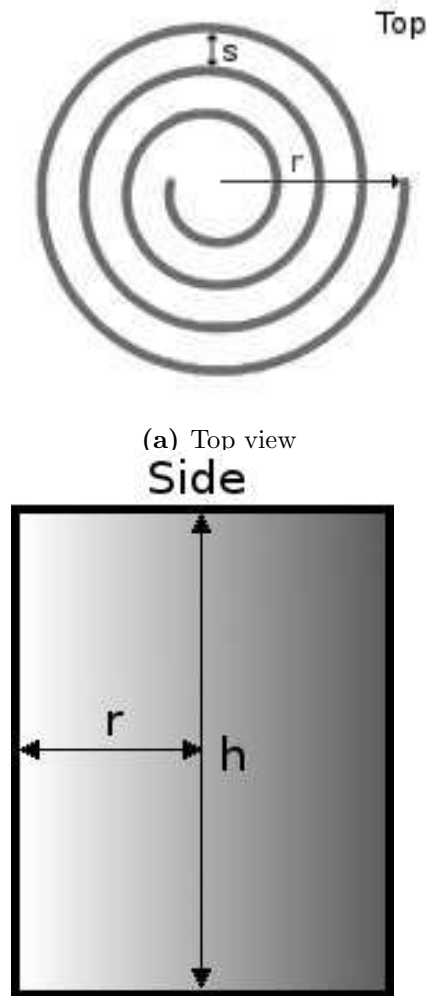


Figure 4.5: Tailor-made coil - (a) Top view shows the top view of how the coil is wrapped. Figure (b) gives the side view of our coil.

The coil design alone is not ample to dissipate the heat produced by the alternating magnetic field and the high current density that will be flowing. To eliminate the high heat production, the coil has to be cooled externally. There are several methods to decrease the overall temperature of the system; blowing air on

the coil constantly, adding a heat sink to absorb some of the heat, using a liquid to cool the coil, using thermal pads on the coil. The most efficient in the previous list is liquid-cooling. To achieve this, water is injected into the set-up and water is chosen because it has a high-heat capacity and it will take a large amount of heat energy to heat it by a few degrees Celsius. To prevent short-circuit from ions present in water, the copper sheets are isolated inside an enclosure and the water is de-ionized before being used. Also, a thin kapton film is inserted in between the layers of copper to dissipate additional heat. A chiller is trusted with the task of maintaining the temperature of the water at a constant level. A pump will be responsible to sustain a constant flow-rate in the pipes. The coil, pump and chiller is shown in 4.6. In the figure, red color represents very high temperature and blue color represents cold temperature. Cool water flows into the system thence forcing the hot water from the coil. A valve is included in one of the pipes to regulate the movement of water and thus preventing excessive pressure from building inside the coil.

To connect the current supply to the coil, two leads are included. One is located on the innermost sector of the coil while the second one is located at the edge. The values of r , the distance from the center of the coil, will be minimum and maximum, respectively. On a final note, a glass tube containing the sample will be placed inside the enclosed coil from the top.

<p style="text-align: center;">Chosen Coil Copper sheets spirally wrapped</p>
--

The magnitude of the magnetic field will be addressed in the forthcoming sections.

4.3.2 AMF Power Supply

The coil that was designed in the previous section will produce a constant magnetic field if a direct current (dc) supply is connected to the leads. Yet, we concluded in Chapter 3 that an oscillating magnetic field is required to produce heating effects in nanoparticles. To produce an oscillating magnetic field, instead of a direct current supply, an alternating current source has to be used. Alternating current sources are fairly common but for our purpose, a regular alternating current (ac) supply will not work because the regular ac sources have a frequency

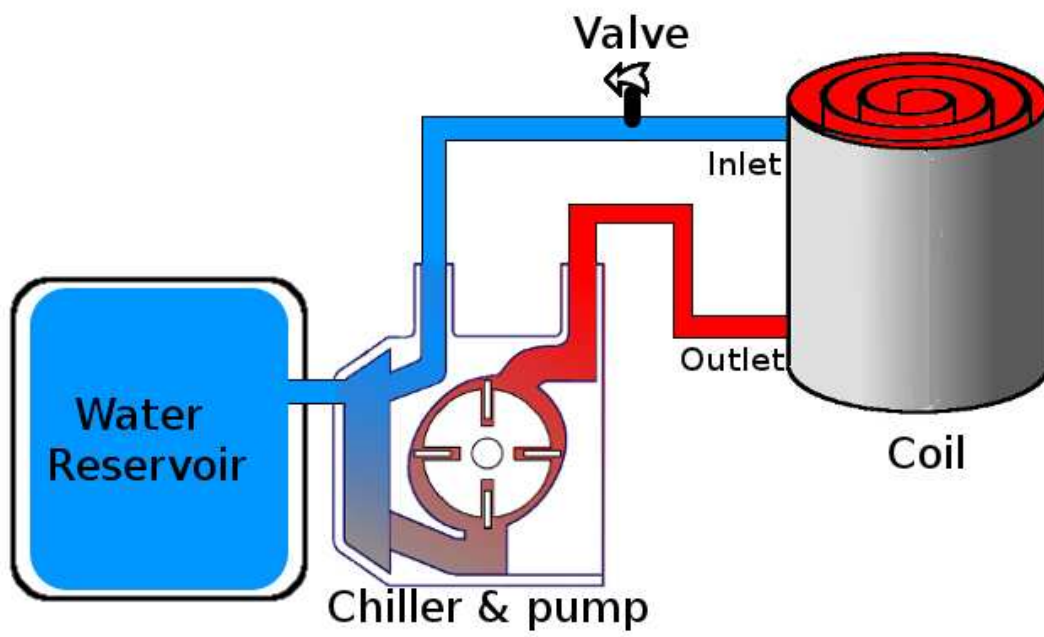


Figure 4.6: Coil cooling mechanism - The cooling process of the coil with the help of the chiller and the pump.

of either 50 Hz or 60 Hz. Our chosen frequency was in the order of kilohertz and a current supply which oscillates at this frequency is not readily available. Therefore, a black-box which converts a direct current to an alternating current has to be implemented. It should be characterized by:

- Changeable magnitude of current
- Variable frequency

The diagram for this system is shown in Figure 4.7 and a power supply takes in a direct current as input and converts it into an alternating one. A frequency generator capable of changing the appropriate frequency for the oscillation of the magnetic field.

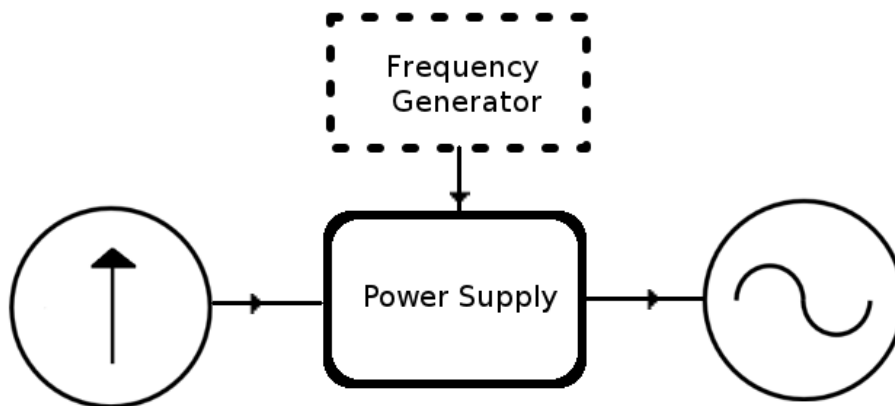


Figure 4.7: Schematic of power supply - The power supply responsible for converting the dc source into an ac one with chosen frequency.

The power supply consists basically of an inductor and a capacitor. The purpose of these two components is to define the resonant frequency of the system. Inductive reactance magnitude X_L increases as frequency increases while capacitive reactance magnitude X_C decreases with the increase in frequency in a series ac circuit.

Frequency	X_C	X_L
↑	↓	↑

There is a specific frequency that the resultant reactances are equal in magnitude and thus they nullify each other. The frequency at which this happens is the resonant frequency f_r and is given by:

$$f_r = \frac{1}{2\pi\sqrt{LC}} \quad (4.6)$$

At the resonant frequency, the current flowing out of the circuit into our coil is maximum because the circuit impedance is minimum. As a result, the magnetic field in the coil will have the utmost value.

An external frequency generator has to be employed to fine tune the resonant frequency of the system. The frequency generator is manufactured by BK Precision. A picture of the frequency generator that was chosen (BK Precision 4011A) is given in Figure 4.8. The frequency can sweep a large frequency range, from 0 Hz to 5 MHz. Hence in the future, if we choose to go to a higher frequency, we can do so with ease.



Figure 4.8: BK Precision 4011A function generator

In this set-up, the inductor maintains a constant value while there is a set of capacitors with capacitances, consequently different resonance frequencies. Each capacitor operates independently of the other and when selected, only that specific capacitor contributes to the circuit. The other ones are open-circuited. The

resonant frequency of the combined capacitor and inductor that was chosen is between 100 kHz and 1 MHz.

For a desired frequency, we need to switch to a predefined capacitor and then adjust the frequency of the generator to bring the system to a self resonance.

The connected set-up is shown in Figure 4.9. The enclosed copper coil containing a glass tube is shown in the center of this figure. On the left is the power supply that converts a direct current into an alternating current. A function generator on its right (showing 176.8 on its display) sets the whole system into resonance. On top of the frequency generator, we have the FISO fiber-optics temperature controller. The temperature probe is put inside of the glass tube. Finally, on the bottom of the function generator, there is a constant voltage supply which sets the required voltage to drive the components in the power supply.

4.3.3 Optimization of the System

As we have previously stated, with a highly oscillating field, the copper coil will heat up and the heating of the coil will drastically increase with increasing alternating frequency. This is the prime reason for water-cooling of the inside coil. However, even with water cooling, the coil will have a tendency to heat up because the water being pumped into the coil cannot remove completely the amount of heat released by the coil. Hence, there will be some heat transfer to the sample by convection. Convection heating implies currents in some fluid (e.g., air) and the medium is responsible for carrying thermal energy from one point to another. Without the fluid, then there will be no convection. Being cognizant of this fact, we have decided to pump the air out of the coil and having a partial vacuum inside the coil. This will obliterate any heat transfer into the sample. Thence, any increase in temperature of the magnetic nanoparticles will be solely due to the increase in temperature of the particles.

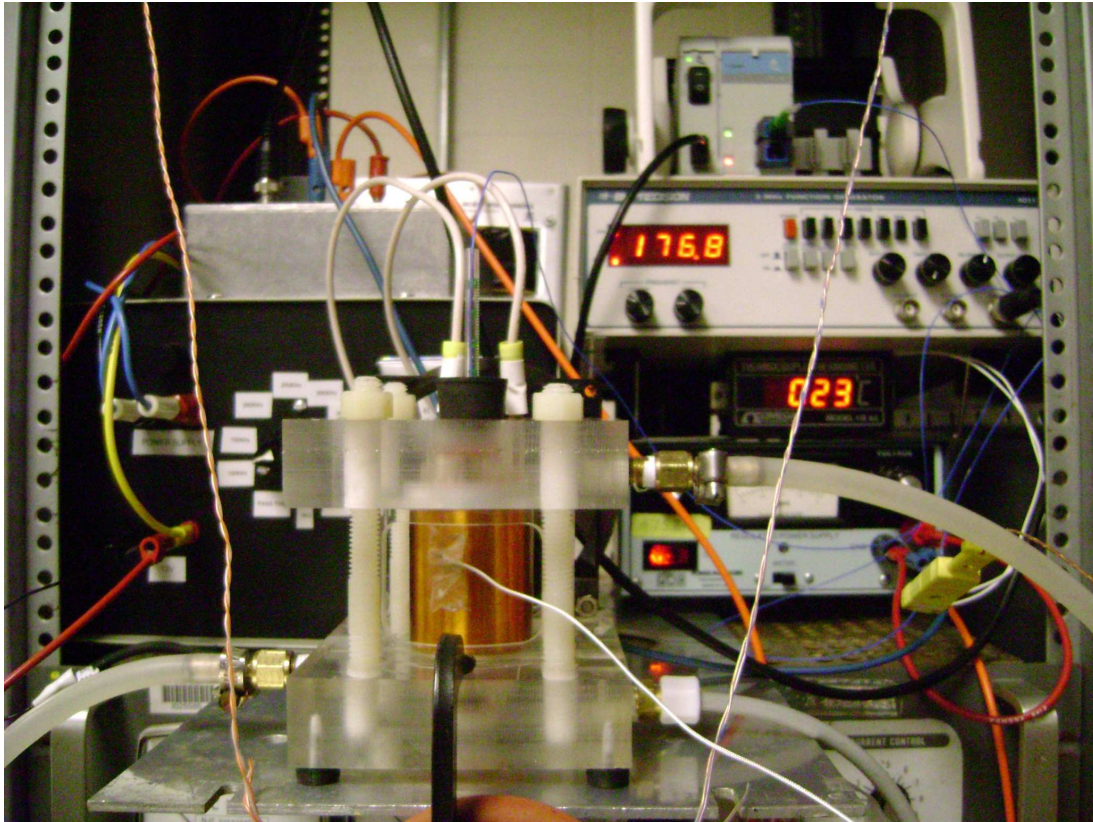


Figure 4.9: Set-up assembly - The complete set-up of the function generator, the fiber-optics temperature probe, the power supply and the coil.

4.3.4 End-Product

The final system including the chiller, the vacuum pump, the power supplies the fiber optics temperature probe and the coil is shown in Figure 4.10. A thermocouple is added to monitor the external (outside) temperature of the coil and thereby prevent overheating of the coil.

4.3.5 Commercially Available Systems

There are also commercially available systems that do the same thing as our system, with a less level of sophistication. For example, Ambrell, an Ameritherm company produces the Easyheat kit. The compact Easyheat induction heating systems feature a power supply and a movable work head incorporating the coil that can be located up to 3 m from the power supply. The induction heater has a precise power control within 25 W resolution. It features a front panel LCD and sealed touchpad and remote power control is available for employing contact inputs, analog inputs or optional serial data port. A picture of the apparatus (power supply and work head including a coil) is shown in Figure 4.11. It is a water-cooled system, requiring a connection to a heat exchanger or other mechanism for dissipating heat [52].

Features

- Agile tuning for single-cycle and continuous heating operations
- Selection and monitoring of power levels from the front panel LCD and sealed touchpad
- Easy control of the duration of the heating cycle with a built-in programmable digital timer
- Repeatable, reliable heating with agile frequency tuning
- Field-calibration capable
- 3 m movable workhead

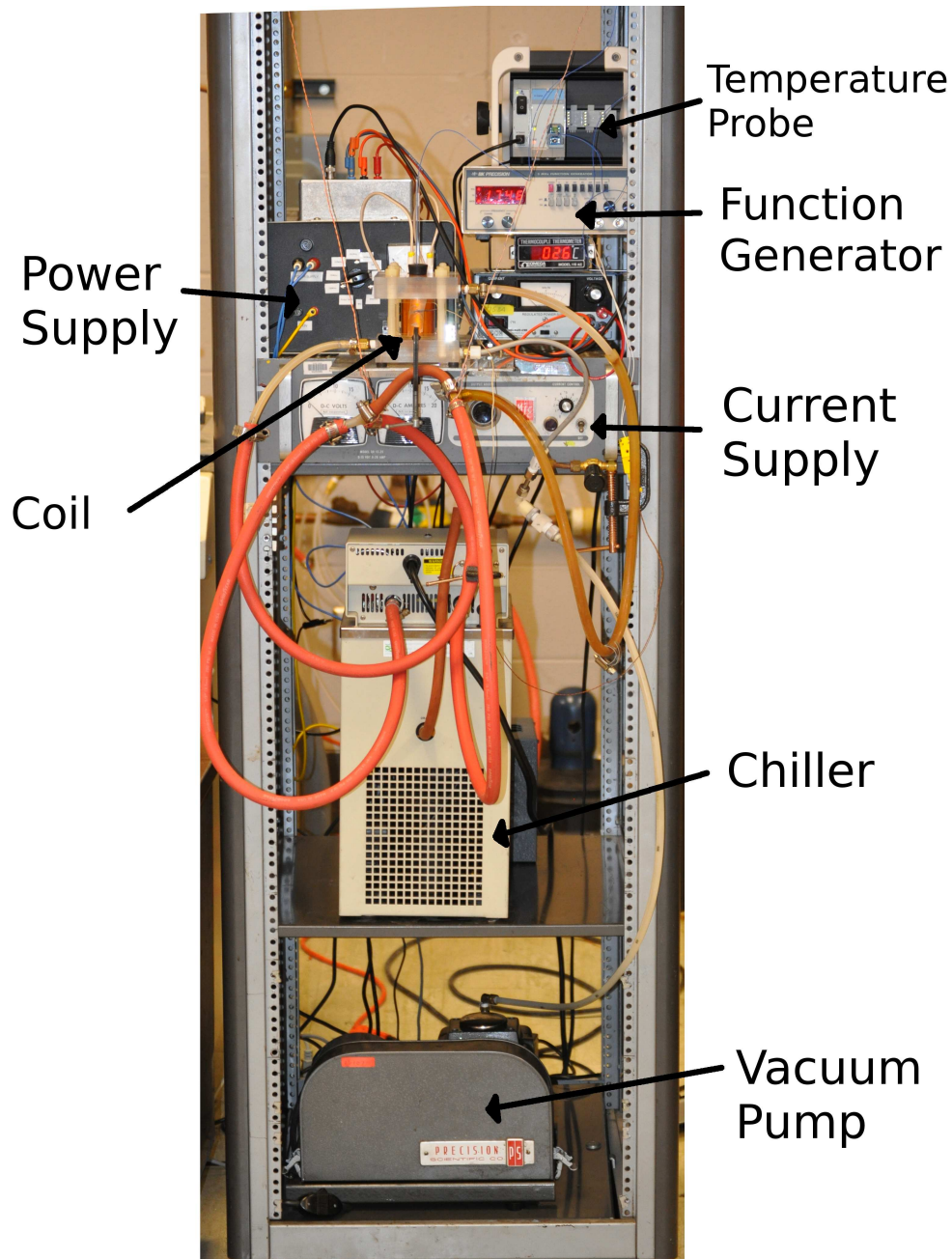


Figure 4.10: Complete system setup - There is the vacuum pump at the bottom, then the chiller for cooling the water above it. On top there is the current supply which feeds the power supply on the top left. On the right lies the function generator and the fiber optics probe.



Figure 4.11: Ambrell EASYHEAT induction heater - The left picture shows the complete system. The power supply is on the bottom while the work head is on top. A coil is mounted on the work head. The right picture is a zoomed image of the LCD panel and touchpad. It displays the current flowing through the coil and the frequency of oscillation.

One of our collaborators has the 1.2 kW Easyheat induction heating system. To this system was attached a 5-turns copper induction coil (Figure 4.12). A chiller was responsible for maintaining the overall temperature of the system constant. The coil temperature was kept at 10 °C with a water flow from the external Lauda thermostat. The exact dimensions of the coil are as follows:

Inner Diameter: 27 mm

Tube Diameter: 6.35 mm

Length: 55 mm

Spacing between the tubes: 6 mm

4.3.5.1 Comparison with Commercially Available System

Since our collaborator has this system, it will be good to compare the major differences of both system.



Figure 4.12: Coil in Belfast - The commercial system was attached to this 5-turns coil into which water was flowed.

Custom Built System	AMBRELL Easyheat 1.2 kW
Cheap	Expensive
Fixed System	Movable work head up to 3 m
Variable frequencies	Fixed frequency for each coil
Low current operation	Up to 300 A current
Slow cycle	Fast power cycle

The major advantage that our system has over any commercially available system is that we can change to any frequency that we wish. Hence we have the freedom to choose from a range of frequencies. If we decide that we would like some other frequencies, then we need to replace the set of capacitors by another set of capacitors. This is easily done since the system is modular.

4.4 Chapter Summary

The various sections in this chapter describe the different stages in the production of an alternating magnetic field system.

This AMF system consists of a power supply capable of producing an alternating current at a frequency in the range of kilohertz. The main components in the power supply are power components, a set of capacitors and an inductor.

The alternating current that is produced by this power supply is fed to a coil. This coil, because of its special design, produces a magnetic field inside of its walls. It is enclosed in a special case for safety purposes. The coil in turn is connected to a pair of connectors for cooling the coil. Cold water maintained at a specific temperature by a chiller enters the coil and cools it from the inside. A vacuum pump is connected to the coil enclosure. A vacuum inside of the coil is important because it eliminates any possible heat transfer by conduction or convection from the coil.

The aim of this system is to measure the heating rate of magnetic nanoparticles when irradiated by a magnetic field. A sample can be mounted in the coil and when the field is turned on, the temperature will increase if the material is magnetic in nature. Hence, we have chosen a very sensitive temperature probe that is unaffected by an oscillating magnetic field. The probe operates by measuring how light is totally, internally reflected by a fiber optic tube.

CHAPTER 5

Results

This chapter will exhibit the different results of the experiments or simulations that have been performed during this research. Because data has been collected in two different locations, it will be best to dissect the chapter into two independent parts. The first part will depict results that have been obtained at Wright State University (USA) using the custom-built system. The second part will concentrate solely on data that were obtained at Queen's University (UK). Before proceeding to the data, it will be best to describe the entities common to both places.

5.1 Magnetic Nanoparticles

Ferromagnetic nanoparticles that had been synthesized with various grain sizes (30-50 nm) by a sol-gel method were obtained from our collaborator [53]: GPZ4, GPZ5, GPZ8, and GPZ11. The morphology as well as magnetic properties were studied using X-ray diffraction (XRD), scanning electron microscopy (SEM), X-ray photoelectron spectroscopy (XPS), and vibrating sample magnetometry (VSM).

The average crystallite sizes, calculated using the Scherrer equation from the XRD peaks, were found to vary from less than 10 to 26.9 nm for the samples. The

characteristics of the hysteresis loop, the coercivity, and the saturation magnetization, are shown in Figure 5.1a while the remanant magnetization and hysteresis loss are presented in Figure 5.1b as a function of the average crystallite size at 295 and 355 K.

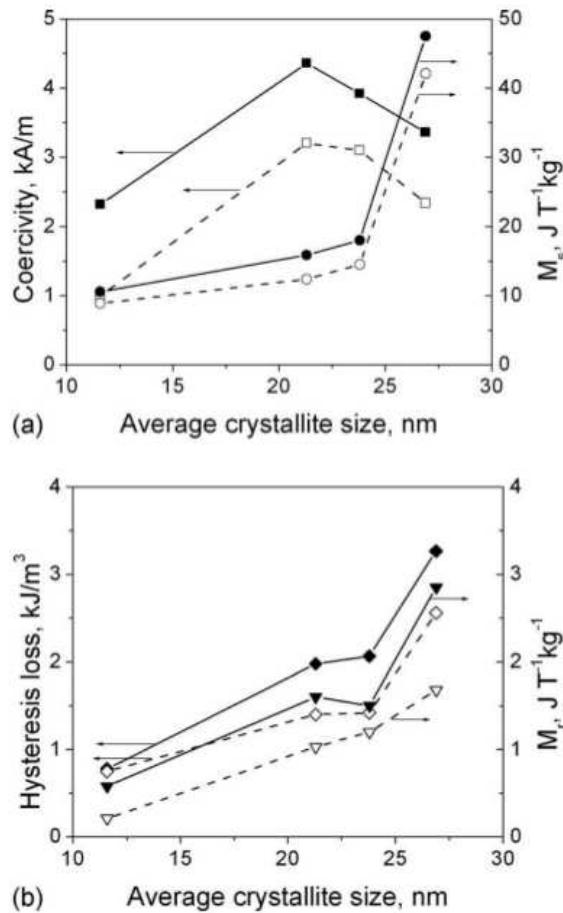


Figure 5.1: Hysteresis loop, coercivity, and saturation magnetization - (a) Coercivity and saturation magnetization M_s ; (b) hysteresis loss and remanant magnetization M_r as a function of crystallite size. Solid lines and closed symbols: measurements at 295 K, dashed lines and open symbols: measurements at 355 K.

The remanant magnetization M_r , saturation magnetization M_s , and coercivity H_c were measured at 295K by means of a VSM equipped with a 2 T electromagnet. The Joule energy density in Table 5.1 refers to the dissipated energy density. For a more detailed explanation of how the synthesis and magnetic measurements

Table 5.1: The sizes and magnetic properties of the nanoparticles are shown as measured by the VSM, SEM and XRD.

Name	Sample	Grain Size (nm)	M_r (emu/g)	M_s (emu/g)	H_c (Oe)	Joule (J/m ³)
Ni _{0.5} Zn _{0.5} Fe ₂ O ₄	GPZ4	48.7	2.85	47.5	42.2	3266
Co _{0.4} Ni _{0.4} Zn _{0.2} Fe ₂ O ₄	GPZ5	46	3.29	26.2	75.3	3683
NiFe ₂ O ₄	GPZ8	42.9	3.47	14.8	146	6182
CoFe ₂ O ₄	GPZ11	34.5	7.01	22.2	626	12250

were accomplished, see [53, 54]. A list of the magnetic parameters for the following ferrites: Ni_{0.5}Zn_{0.5}Fe₂O₄ (NZFO), Co_{0.4}Ni_{0.4}Zn_{0.2}Fe₂O₄ (CNZFO), NiFe₂O₄ (NFO), CoFe₂O₄ (CFO) is presented in Table 5.1. ¹

5.2 Mass Measurement

One of the critical aspect in this research is to get the most accurate value of the mass. To achieve this, a precise mass balance was chosen that can measure to the nearest tenth of a thousand gram (0.0001 g). Since even the slightest change in the surrounding conditions can affect the mass measurement, the balance was shielded on all sides with glass panes. The balance that was used for the accurate measurement of mass is given in Figure 5.2.

5.3 Holding Container

Before we can proceed to doing the experiment, we have to select the proper container to put the magnetic nanoparticle into. The container that was chosen was a 5 mm outer diameter nuclear magnetic resonance (NMR) tube. This is an ideal holder because of its small inner diameter notably 4.57 mm. In terms of manufacturing, NMR tubes have the finest overall finish and quality. The tubes have the added-advantage that their inner diameter is equal throughout the tube. This usually is never the case in regular tubes since the base is thicker than the walls on the sides. On top of that, as these tubes are long (7 in.) compared to

¹1 emu/cm³ = 12.57 × 10⁻⁴ Wb/m² and 1 Oersted = 79.6 A/m



Figure 5.2: Mass balance - The balance used to measure the mass of the powder of the nanoparticles.

other tubes, they are unaffected by possible air drafts. They are quasi free from defects in material and workmanship. All the tubes that were used had the same diameter. The tube is shown in Figure 5.3.



Figure 5.3: Wilmad NMR tubes - The container which holds the magnetic nanoparticles.

A known mass of magnetic nanoparticle was measured using weighing paper and then transferred into the tube. The total mass of the quartz tube with the sample was re-measured to cater for any remanants on the weighing paper. The final mass of nanoparticle is given as:

$$m = m_{total} - m_{tube} \quad (5.1)$$

The next step requires the insertion of the fiber optic temperature probe in the tube. As I mentioned earlier, the NMR tubes are paragon because of their

small inner diameter. Hence, a very small amount of nanoparticles is required to have a reasonable height of the sample.

When the temperature probe is inserted, then particles spread on all sides leaving the probe nearly in the middle of the tube as shown in Figure 5.4.

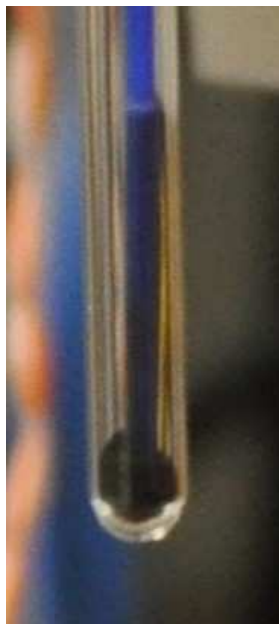


Figure 5.4: Probe position relative to powder - The probe was carefully centered inside of the NMR tube for all measurements.

5.4 Test Measurement

To test the validity of the equipment, a known amount of NaCl (refined salt) was inserted in an NMR tube and was subjected to the alternating magnetic field. The measurement is shown in Figure 5.5 and there is less than $0.005\text{ }^{\circ}\text{C}$ variation in the first 40 s of running time re-enforcing the fact that heating loss is minimal initially.

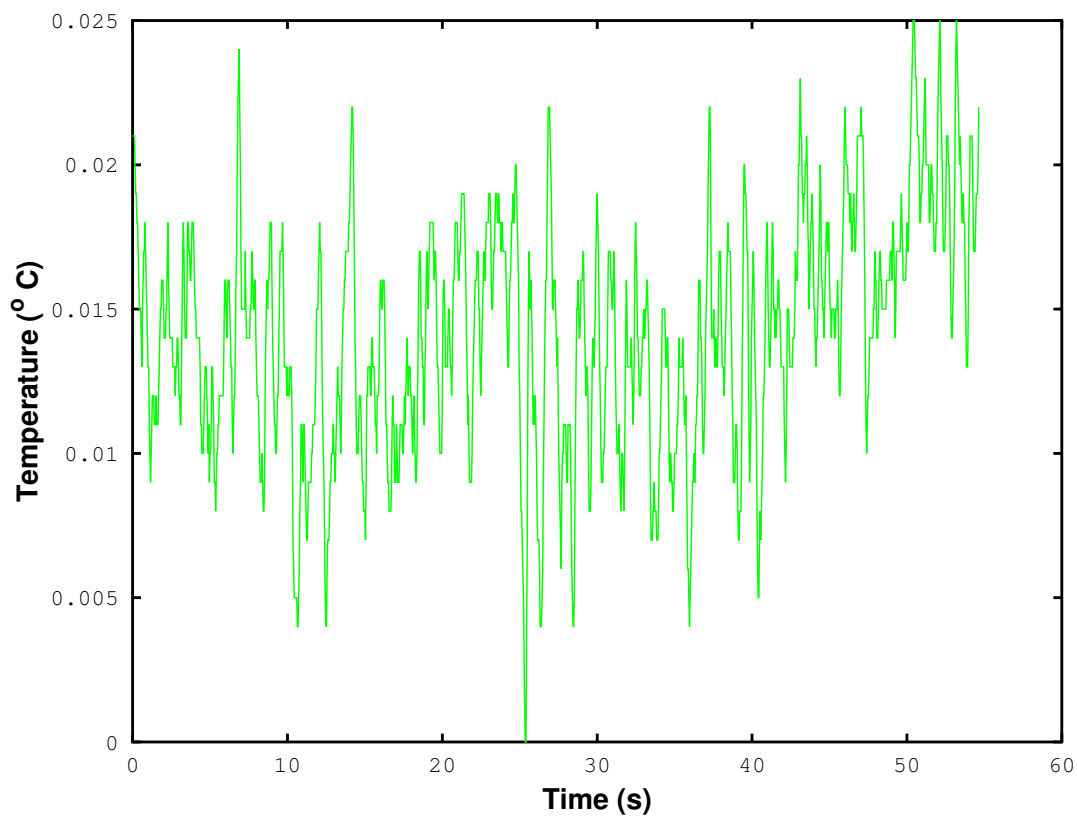


Figure 5.5: Test Measurement - NaCl was used instead of magnetic nanoparticles as a reference measurement.

Part I

Wright State University Data

5.5 Resonance Frequency

If we refer back to Chapter 4, we will recall that the capacitors in the power supply had to be set in resonance mode in order to have the maximum output current into the coil. Resonance occurs in an electric circuit at a particular resonant frequency when the transfer function is at a maximum or when the impedance of the circuit is at a minimum in our series connection. Resonance also occurs when the driving frequency matches the natural frequency of the system and since the function generator is forcing the power components to oscillate at the preset frequency, the function generator is acting as a driver in this case.

Table 5.2: Resonance frequencies of power supply - The frequencies predefined on the power supply and the corresponding driver's frequencies.

Capacitor	Frequency	
	Capacitor	Function Generator
A		174.8 kHz
B		259.3 kHz
C		348.0 kHz
D		441.8 kHz
E		726.0 kHz

Hence if we decide on an alternating frequency of, say, 348 kHz, we change to Capacitor 200 on the power supply and we alter the frequency of the function generator to 348.0 kHz, then the output from the power supply will be extremum. Once the resonant frequency was set, the next step was to experimentally measure the frequency of oscillation of the magnetic field. This was performed by inserting a solenoid inside of the coil and see the variation of the induced voltage in the solenoid.

Capacitor	Time-base	Wavelength	Frequency of Operation
A	1 μ s	5.65 cm	177.0 \pm 1.5 kHz
B	1 μ s	3.70 cm	270.3 \pm 1.5 kHz
C	0.5 μ s	5.70 cm	350.9 \pm 3.0 kHz
D	0.5 μ s	4.50 cm	444.4 \pm 3.0 kHz

Thusly, we can conclude that the resonance frequency set by the function

generator is the correct frequency that the magnetic field is oscillating given by Table 5.2.

The other interesting data obtained using the solenoid was the shape of the induced voltage. A picture of the output given by a cathode ray oscilloscope when connected to the two ends of the solenoid is shown in Figure 5.6. As we notice from the figure, the shape is almost sinusoidal except at the peaks where there is some distortion which is to be expected.

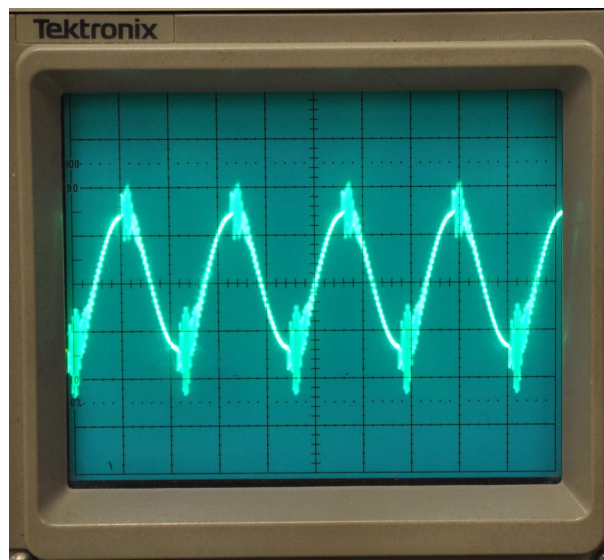


Figure 5.6: CRO output - The output from an oscilloscope when connected to the solenoid which was placed inside of the coil.

5.6 WSU Magnetic Field

The magnetic field was simulated to get a rough value of the magnetic field and an idea of the variation of the alternating magnetic field inside the coil. A proper measurement was then done to get an accurate value of the field using two different approaches.

5.6.1 Simulated Field

The simplified way is to simulate the magnetic field profile of the coil. “Quick-field” (2-D field simulation) ¹ was the software used to simulate the magnetic field. Since the thickness of the coil spiral is much less than the radius of the coil, the coil was assumed as a hollow cylinder with a spacing for positive and negative currents respectively. In 2-D, when viewed from the top, it appears as a pair of parallel conductors. The current (direct) used was 1 A. The diameter of the coil is 3 cm and the length is 5 cm. The output from the software is given in Figure 5.7a. From the simulation, the magnitude of the magnetic field varies by less than 10% (exactly 5.4%) within the axis of the curve. We deduce that the magnetic field of the system is 1.611×10^{-5} T for 1 A. This is however an estimate since the exact geometry was not used and a d.c. simulation was performed.

5.6.2 Measured Magnetic Field

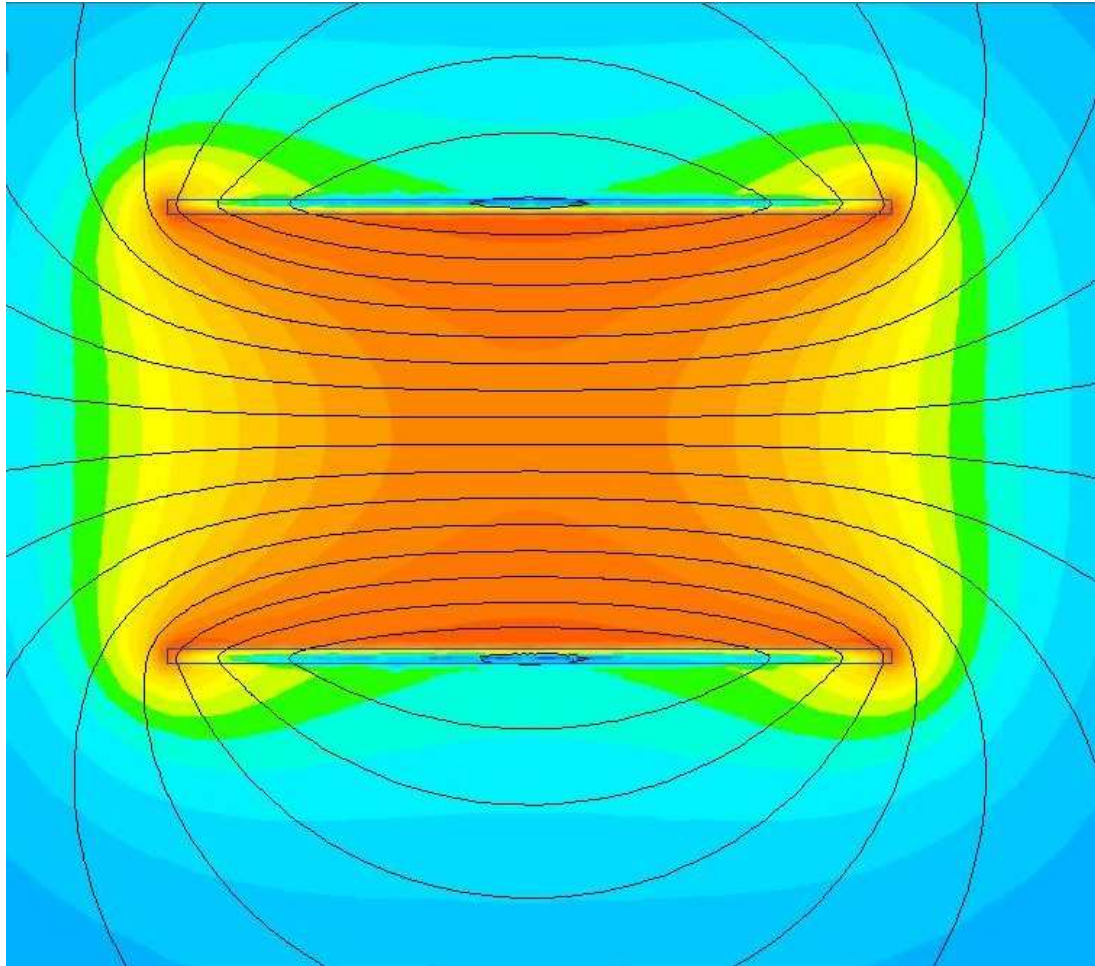
To test the field inside the coil, a sensor from Magnetic Sciences (Figure 5.8 - MC162 B-thin Sensor) ² was used. This accurate sensor has a flat, calibrated frequency response from 2 kHz to 1 MHz and an estimated accuracy of calibration data is ± 10 % of magnetic field. The coil was connected to a cathode ray oscilloscope with capacitance of 20 pF and resistance of 1 M Ω . The output current was varied at two distinct frequencies (174.8 kHz and 348.0 kHz) and the induced emf was measured. The magnetic field values were obtained from the calibrated magnetic fields and are presented in Fig. 5.9. For a supply current of 10 A, the magnetic field was found to be 1.38×10^{-5} T and when the current was 15 A, the field was 2.06×10^{-5} T.

5.7 Magnetic Heating

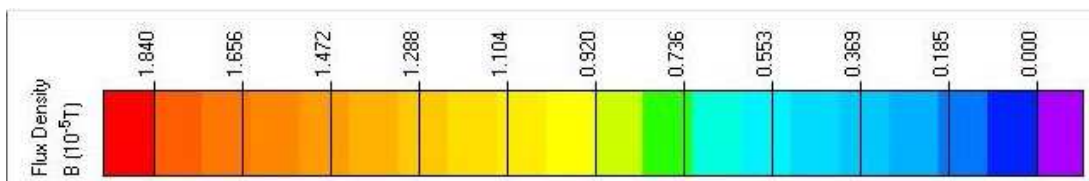
All the four samples were put in an NMR tube along with the probe and were subjected to magnetic heating. Heating took place for 2 minutes and the magnetic

¹Tera Analysis Ltd, Knasterhovvej 21, DK-5700 Svendborg, Denmark

²Magnetic Sciences, 367 Arlington Street, Acton, MA 01720, USA



(a) Simulated Magnetic Field



(b) Legend

Figure 5.7: WSU field profile - (a) The magnetic field relative to the position inside the coil, (b) the legend for the intensity of the field.



Figure 5.8: Induction coil - Designed coil to confirm the simulated value of the magnetic field.

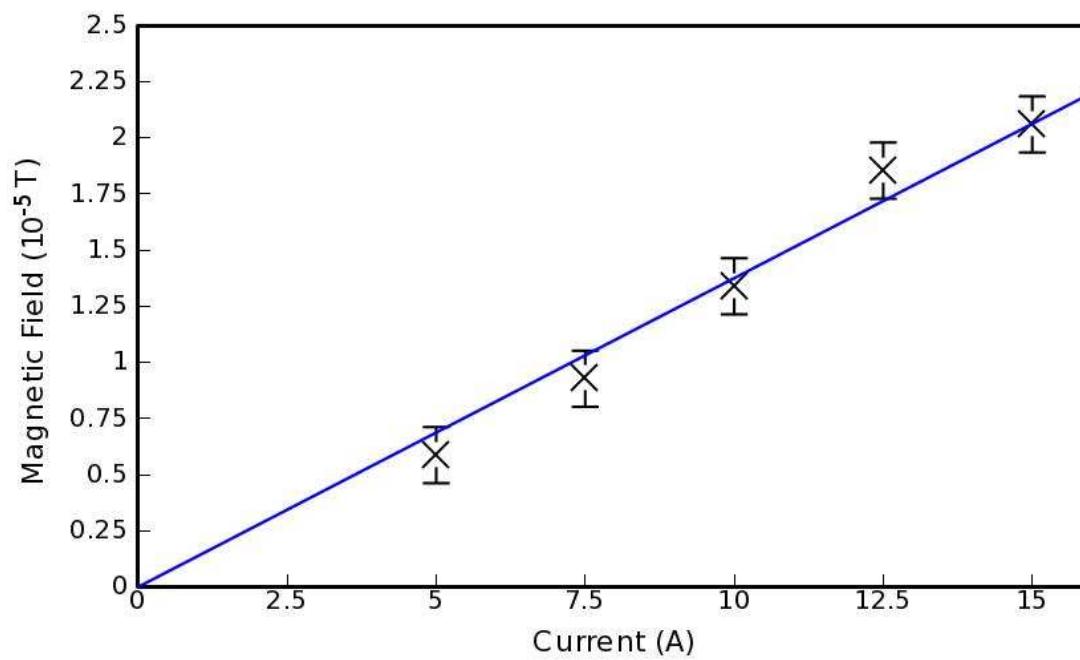


Figure 5.9: Magnetic field measurements - The variation of the magnetic field as the current is increased.

field (1.38×10^{-5} T) was turned off. The sample was allowed to cool naturally and then the experiment was repeated two more times. The magnetic field was increased to 2.06×10^{-5} T and the experiment was done three times. Afterwards, the frequency was changed from 177 kHz to 351 kHz. A total of 12 runs were made for each sample. In the present experiment, we did not perform any kind of alignment and the particles are packed directly to the holder without a binder or suspension material.

5.7.1 GPZ4

Mass of nanoparticle used = 0.0300 g

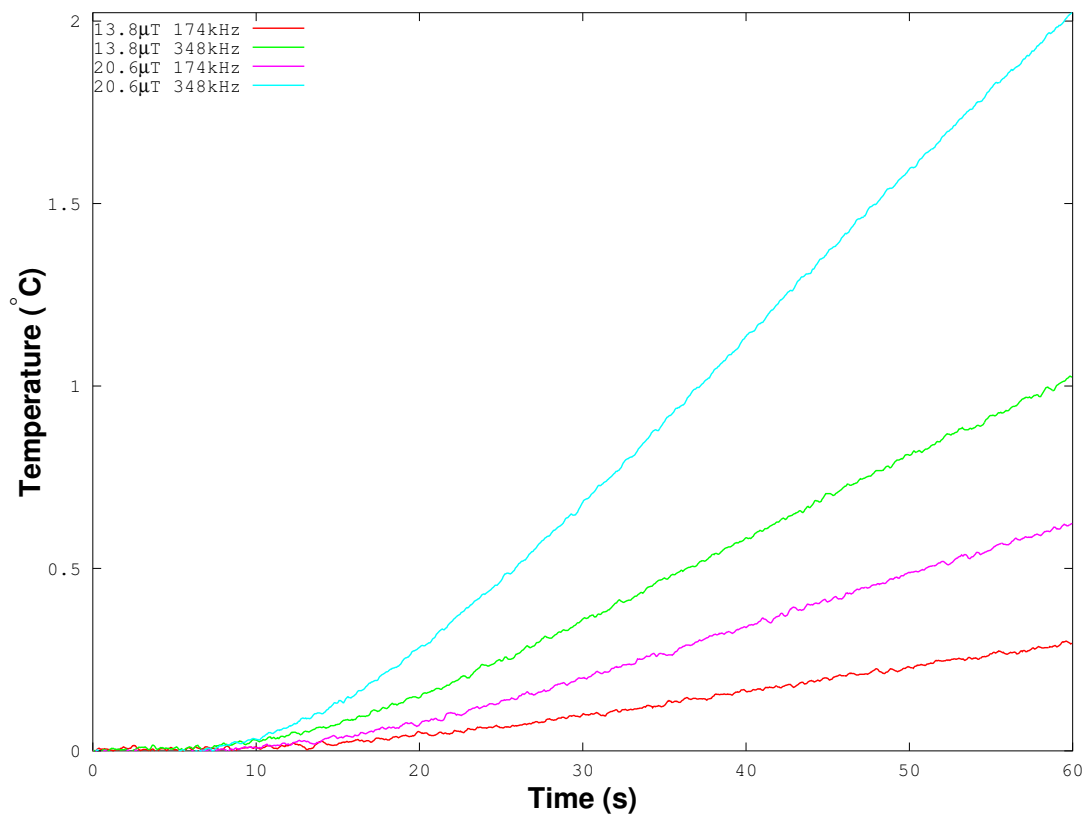


Figure 5.10: Temperature against time of GPZ4 - The variation of the temperature of the GPZ4 nanoparticle with time as the sample is heating up.

5.7.2 GPZ5

Mass of nanoparticle used = 0.0310 g

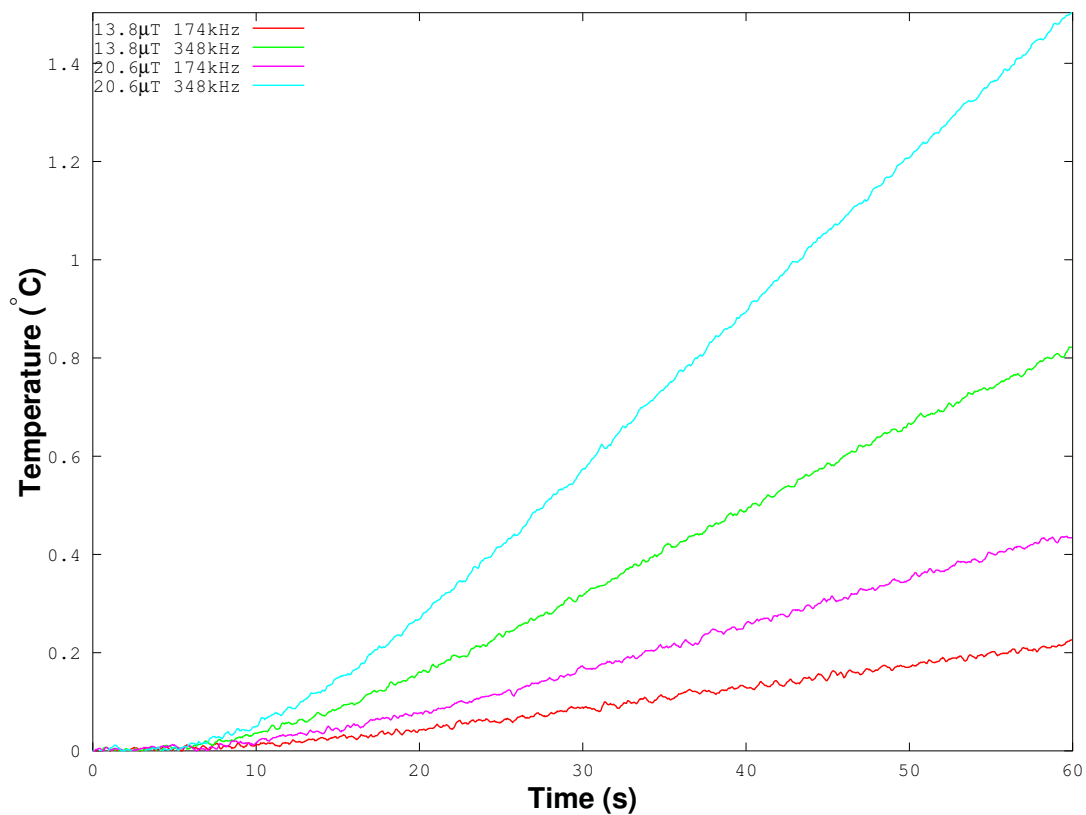


Figure 5.11: Temperature against time of GPZ5 - The variation of the temperature of the GPZ5 nanoparticle with time as the sample is heating up.

5.7.3 GPZ8

Mass of nanoparticle used = 0.0347 g

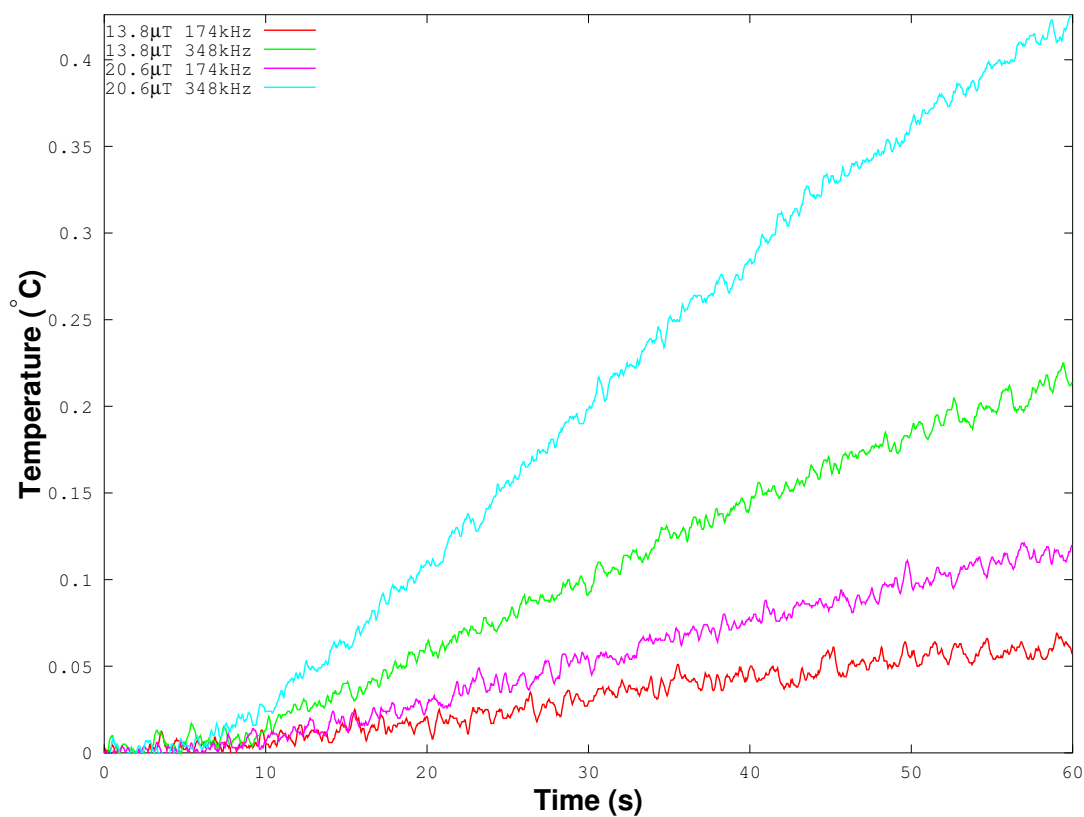


Figure 5.12: Temperature against time of GPZ8 - The variation of the temperature of the GPZ8 nanoparticle with time as the sample is irradiated.

5.7.4 GPZ11

Mass of nanoparticle used = 0.0304 g

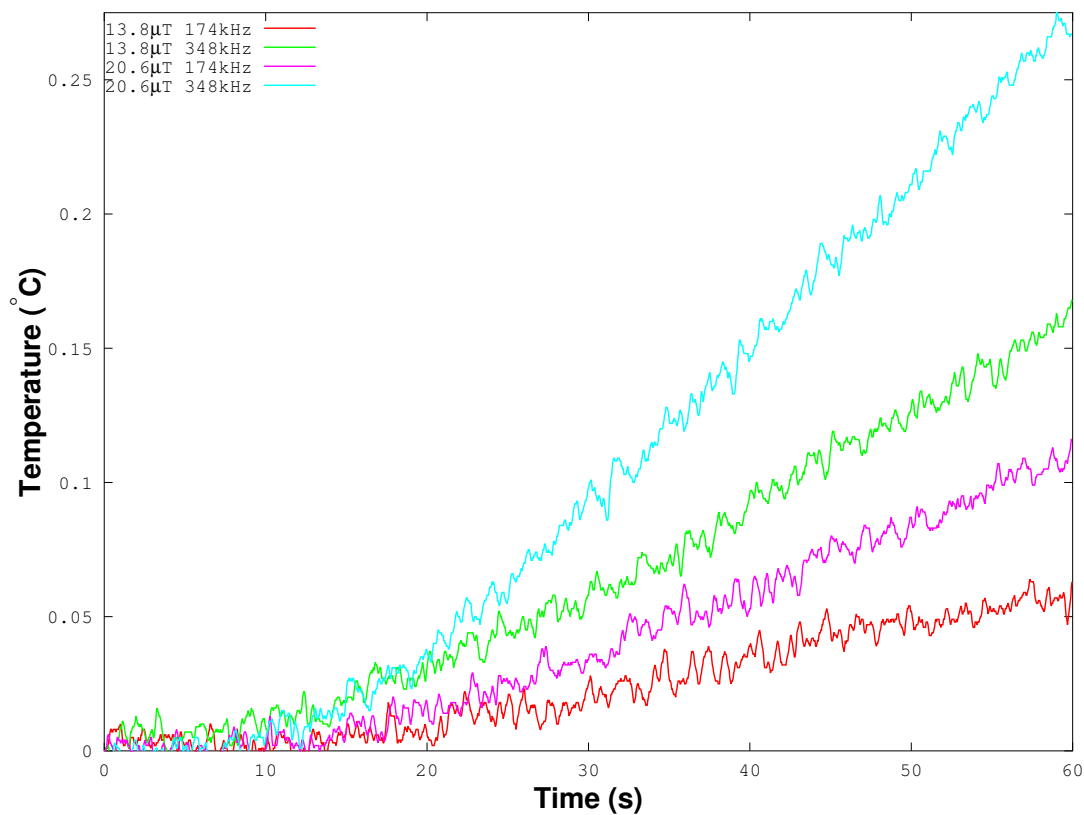


Figure 5.13: Temperature against time of GPZ11 - The variation of the temperature of the GPZ11 nanoparticle with time as the sample is heating up.

As we can see from all these graphs, the temperature increases with a higher magnetic field and higher frequency. The analysis and calculation of how exactly they relate to each other will be discussed in the next chapter.

Part II

Queen's University Data

Data in this section was collected while I was at Queen's University in UK. The apparatus was first set-up and then the same measurements were performed as in Wright State University. The lab at Queen's University was equipped with a commercial Ambrell induction heating machine. The coil was lagged with a special PVC tube and the NMR tube was inserted in the middle of the coil.

The advantage of this system is that it can yield very high power in the copper coil. But the major disadvantage is that the frequency is fixed and there is an internal locking mechanism which regulates the optimum frequency of the current harmonic motion for each current value.

5.8 QU Magnetic Field

The magnetic field was simulated using the same software as before with a current (d.c) of 1 A and the final result is shown in Figure 5.14.

The maximum magnetic field was found to be 0.001647 T for a direct current of 1 A if the sample is in the middle. There is a 9% fluctuation if the sample is positioned within 1.5 cm from the center along axis of the coil.

Unfortunately, we have not been able to measure the magnetic field of the system at Queen's University like we did at Wright State University because of lack of equipment during my stay in the United Kingdom.

Henceforth, we are going to use the current that the apparatus was tuned instead of the magnetic field as a reference.

5.9 Magnetic Heating

This time also, the four samples were subjected to magnetic heating in an NMR tube with the temperature probe. Heating was monitored for 1 minute and then the apparatus was switched off. The sample was allowed to cool naturally and then the experiment was repeated two more times.

The current was varied in steps of 25 A: 25 A, 50 A, 75 A and 100 A. The frequency was almost constant with little variation between the runs.

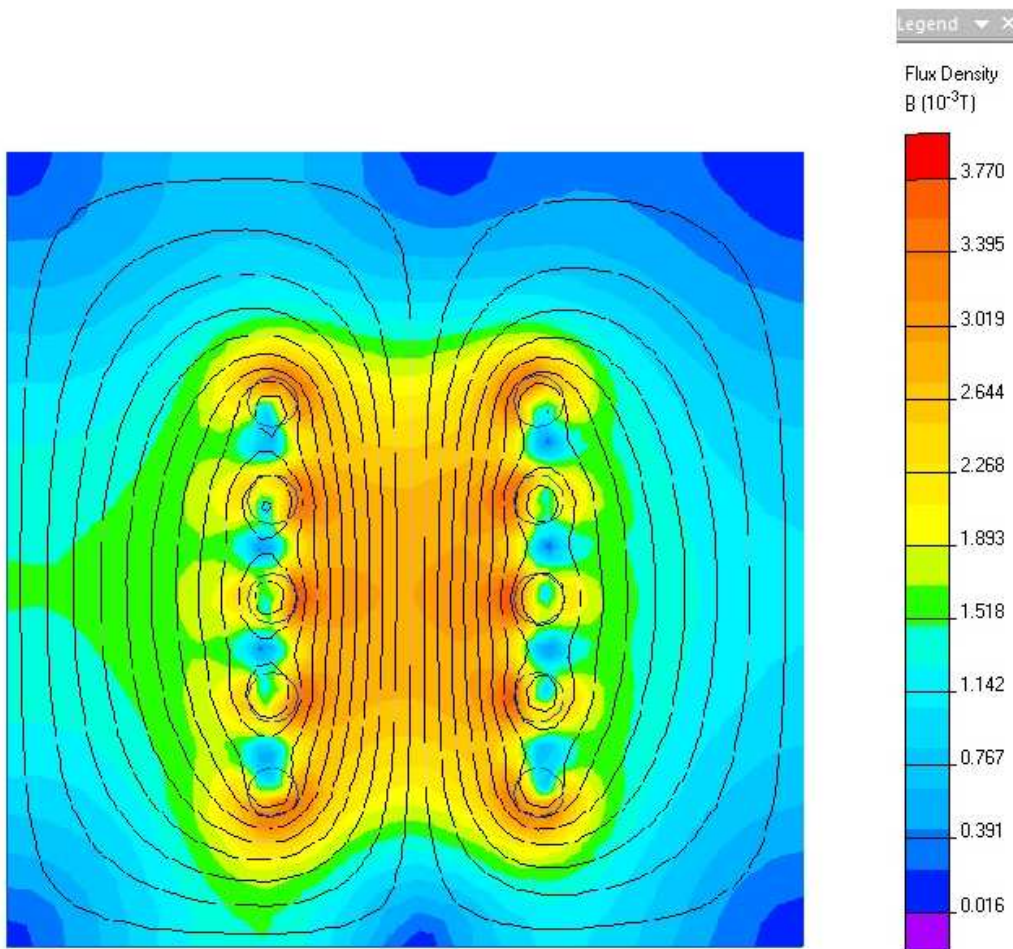


Figure 5.14: QU field profile - The magnetic field relative to the position inside the coil with the corresponding legend on the right.

For any applied current, the power supply finds the optimal frequency of oscillation and then feeds that current to the coil. Hence for each current, there is a specific frequency that enhances the output of the apparatus. For an applied current of 25.2 A, the optimum frequency was found to be 314 kHz; for 50.4 A, it was 310 kHz; for 75.6 A, the frequency reached a plateau of 299 kHz and finally, at 100.6 A, it settled down at 294 kHz. The temperature of the coil was kept constantly at 10 ± 0.2 °C and the temperature of the nanoparticles eventually stabilized at the external coil temperature.

5.9.1 GPZ4

Mass of nanoparticle used = 0.0600 g

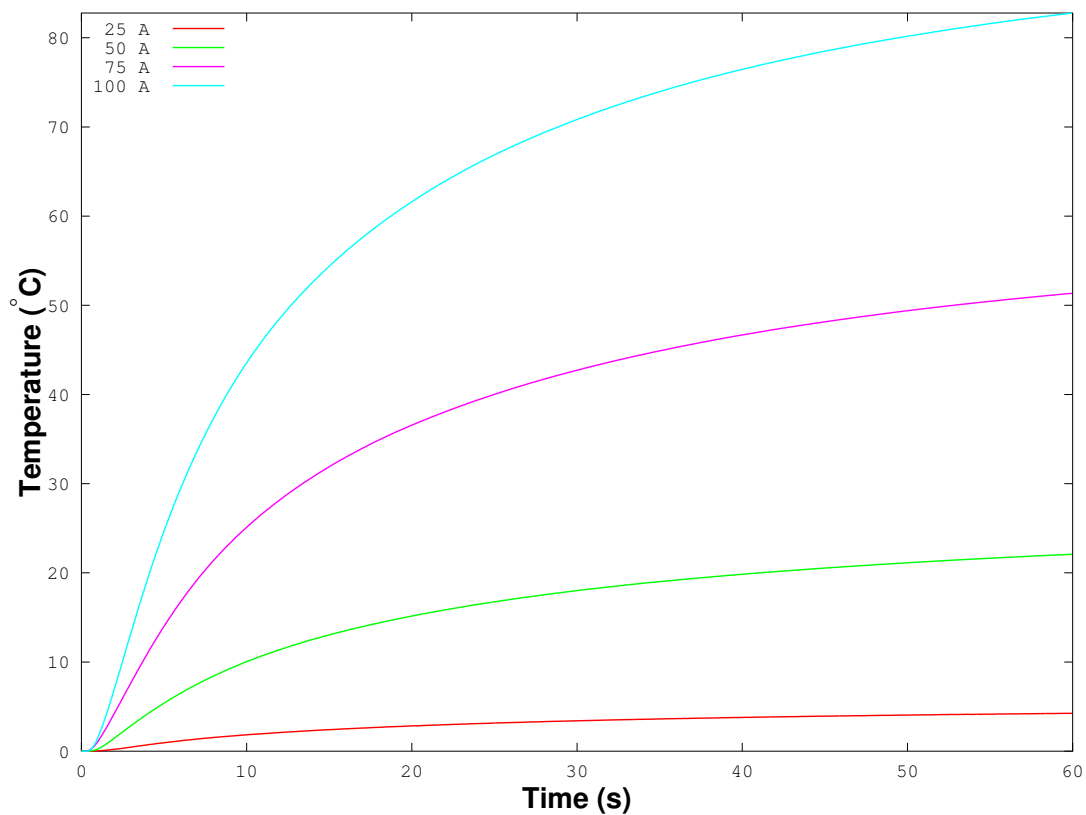


Figure 5.15: Temperature against time of GPZ4 - The variation of the temperature of the GPZ4 nanoparticle with time as the sample is heating up.

5.9.2 GPZ5

Mass of nanoparticle used = 0.0678 g

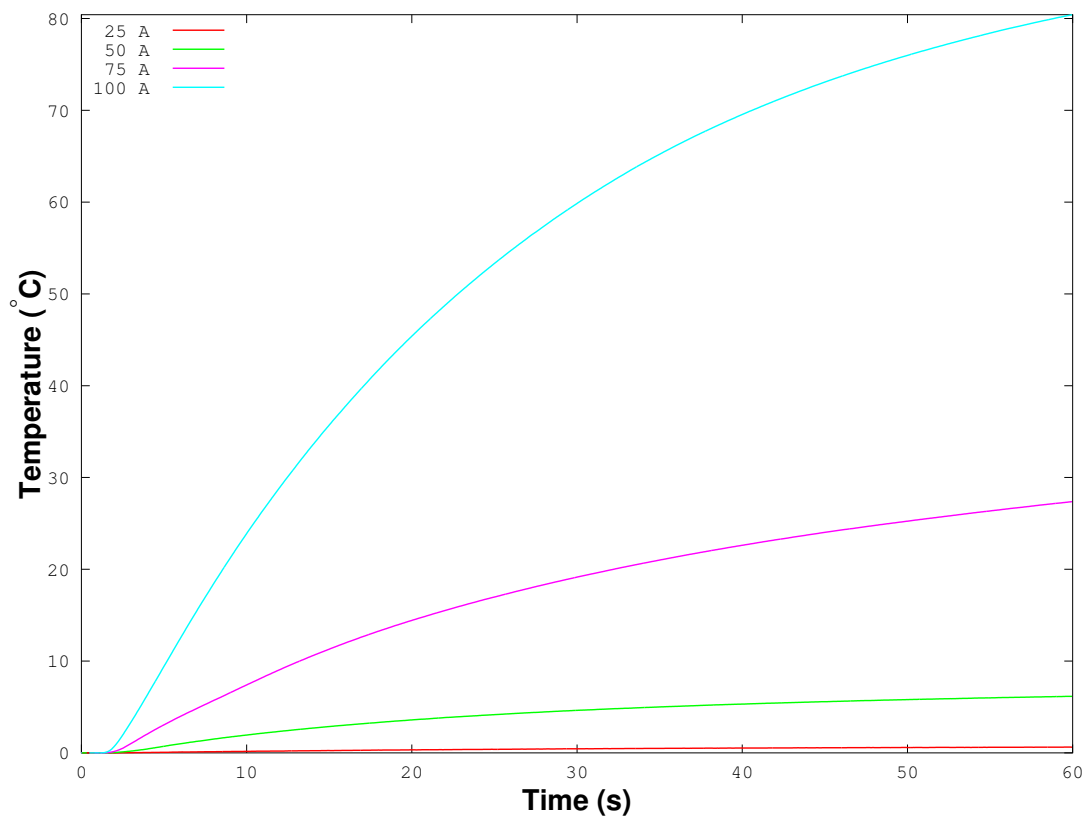


Figure 5.16: Temperature against time of GPZ5 - The variation of the temperature of the GPZ5 nanoparticle with time as the sample is heating up.

5.9.3 GPZ8

Mass of nanoparticle used = 0.0571 g

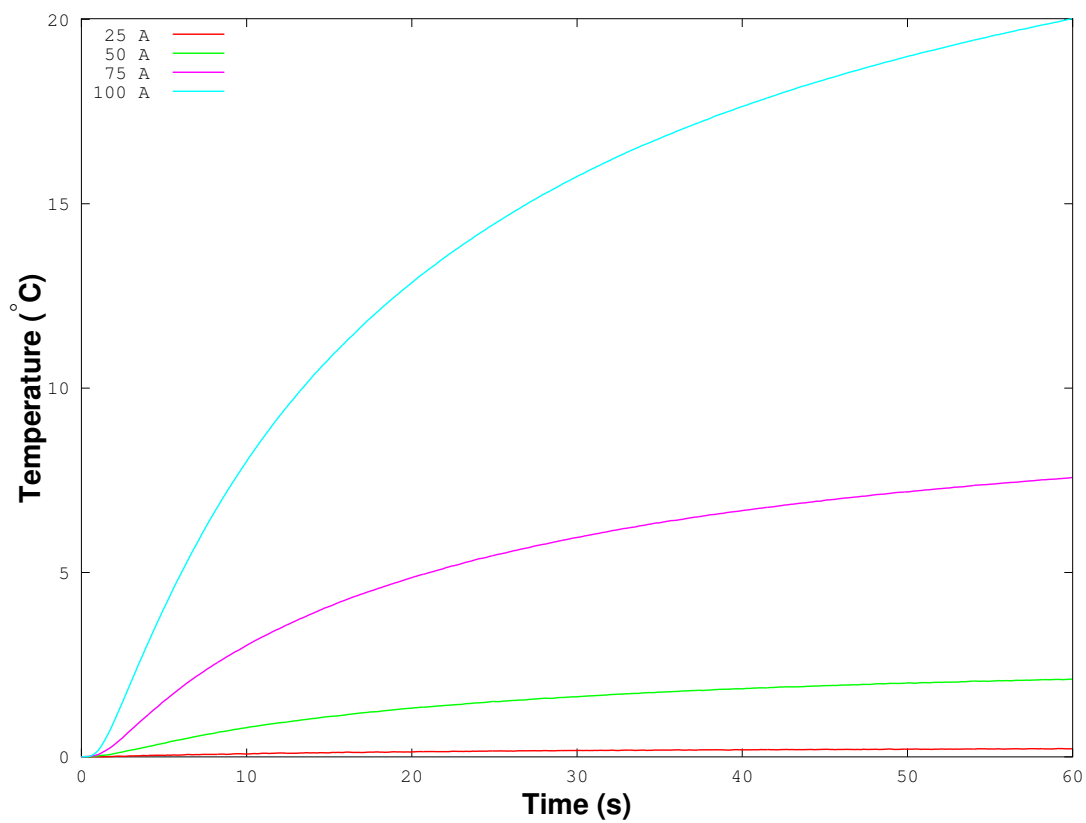


Figure 5.17: Temperature against time of GPZ8 - The variation of the temperature of the GPZ8 nanoparticle with time as the sample is irradiated.

5.9.4 GPZ11

Mass of nanoparticle used = 0.0707 g

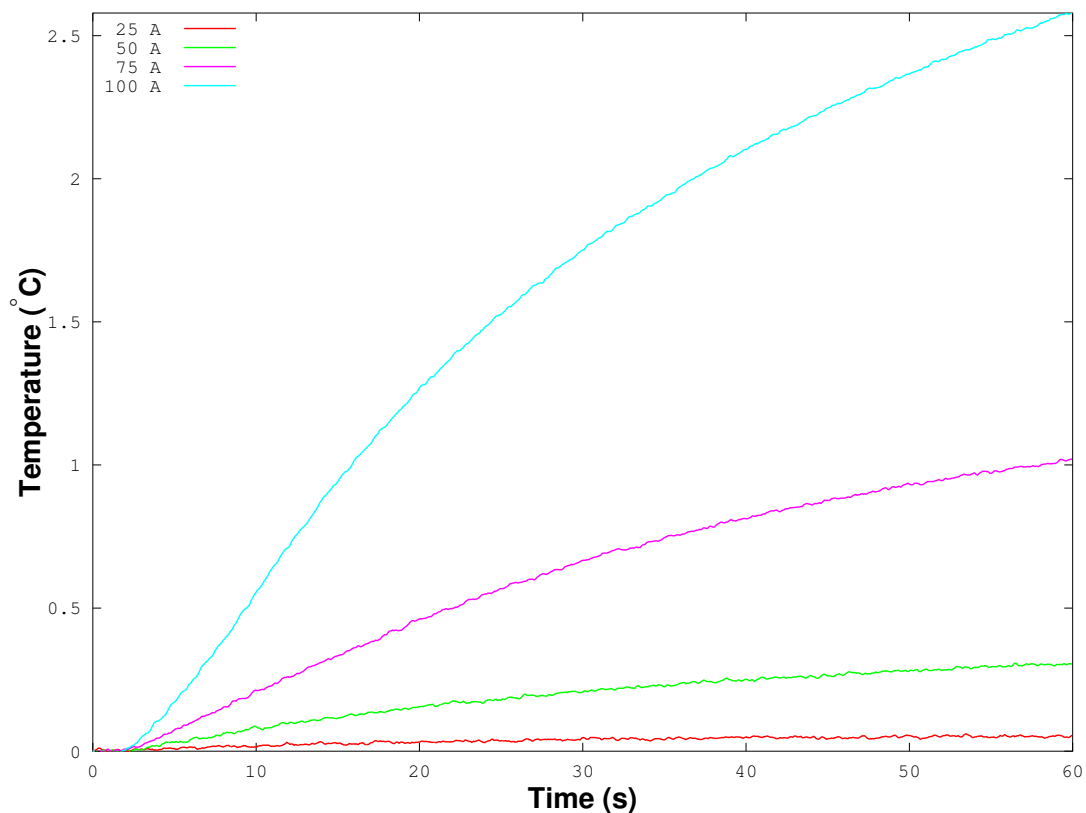


Figure 5.18: Temperature against time of GPZ11 - The variation of the temperature of the GPZ11 nanoparticle with time as the sample is heating up.

From the graphs, we can conclude that the heating rate is much higher as the current was increased. Also, the heating rate is very much higher than for the system at Wright State University.

5.10 Chapter Summary

This chapter elucidated the different phases of the experiment performed in two different labs. The apparatuses used were very similar in both venues. The ferromagnetic nanoparticles were inserted in a 5 mm diameter tube. The fiber optics temperature probe was carefully inserted until it was in the middle of the sample. Then the tube was controlled until it was at the center of the coil. Once the temperature of the sample was stabilized with that of the surrounding temperature, an alternating current (thus alternating magnetic field) was applied. Heating of the sample occurred and the raise in temperature was measured. There was a much higher heating rate at QU as compared to WSU. From the results, it can be concluded that the magnetic field at QU was much higher than that at WSU since the heat response was on a higher level while most of the other variables were kept constant. The magnetic field was measured experimentally at WSU and was found to be 1.38×10^{-5} T and 2.06×10^{-5} T, respectively. We could unfortunately not measure experimentally the magnetic field at QU. The next phase in this research is to calculate the SPL of the samples which corresponds to the amount of heat that can be extracted from the sample.

Analysis and Discussion

After the experiments on the different samples were completed, the data that had been collected were analyzed. This chapter will elaborate how the analysis phase was performed. Based on the results that are going to be obtained, the relationship between the frequency and magnetic field of the system can be compared with the theoretical equation elucidated in Chapter 3. Consequently, the systems in UK and USA will be compared to find whether a common ground can be obtained.

6.1 Heating Rate

The data obtained as a result of the experiments were plotted. A graph of the temperature rise against the time was obtained. Since the heating rate is of interest to us, we have to find the change in temperature in unit time from the graph. This is analogous to the gradient of the curve. To find the gradient precisely we chose to fit a polynomial to the curve.

GNU Plot and GNU BASH were used to plot and manipulate the data sets, respectively. A function that returns the coefficients of a polynomial of a certain degree that minimizes to best fit the data in the least squares sense was developed to do the curve fitting. Several fitting polynomials were tested and an F-test¹

¹An F-test [55] is used to test if the standard deviations of two populations are equal.

was done to determine if a higher order polynomial improves the fit.

The fitting program plots at any time 2 fitting curves and does a 'p'-test which is the probability of observing the improvement in χ^2 obtained by adding an extra parameter to the fit. If $p < 0.05$, then the lower order polynomial was rejected at the 5% level.

Once the best-fit curve was obtained, another routine was created to find the gradient of the fit. The software numerically calculates the gradient at all the points (Figure 6.1) and compares them. The output is the gradient during the initial stages of the heating process as shown in Figure 6.2. The peak of the curve in Figure 6.2 corresponds to the maximum initial gradient in that curve.

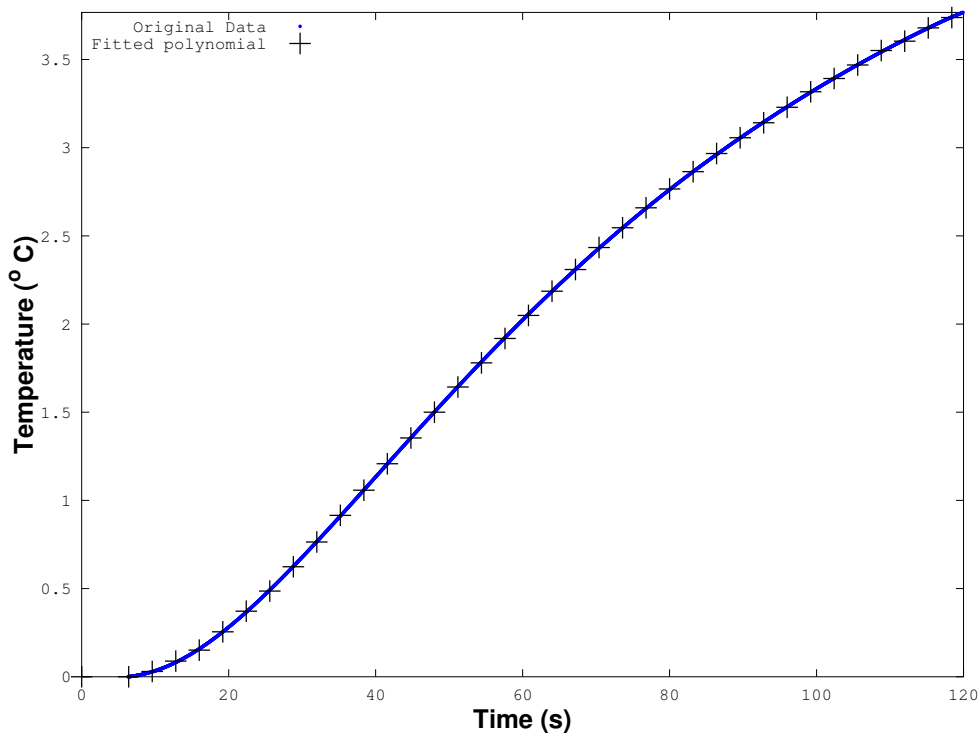


Figure 6.1: Heating rate curve - The plotted data, fitted curve and the maximum heating rate are given.

This gradient corresponds to the heating rate when the heat lost to the surroundings is zero because there is no heat loss or heat gain when the temperature of the sample is equivalent to the temperature of the surrounding.

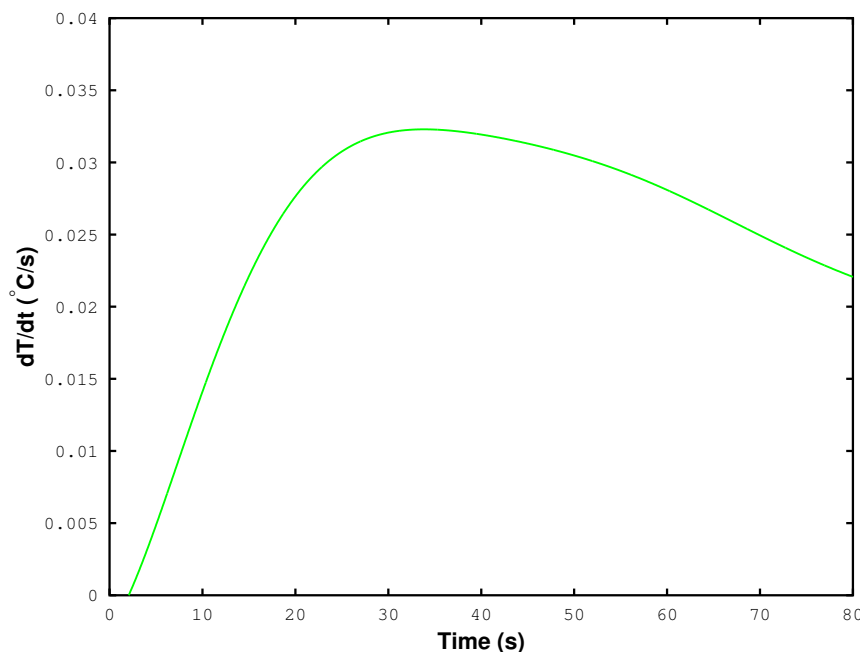


Figure 6.2: Time evolution of gradient - The rate of change of temperature is plotted against time.

A slightly different approach which will theoretically yield the same result is to use Newton's Law of Cooling/Heating and model the heating curve. This method was not adopted because it is computationally intensive and very complex to implement because of the numerous variables and even the slightest change in the external temperature affects the model rendering it futile for our case.

From our manipulation of the graphs, we get the value of $\Delta T/\Delta t$ directly from the gradient. Since all the experiments were repeated at least twice, the statistical mean was performed to reduce the overall (random) error associated with the experiments. The standard deviation of this distribution was calculated using

$$\sigma = \sqrt{\frac{1}{N} \sum_{i=1}^N (x_i - \mu)^2}, \quad \text{where } \mu = \frac{1}{N} \sum_{i=1}^N x_i. \quad (6.1)$$

Table 6.1: The average heating rate of GPZ4 sample when different magnetic fields of different frequencies are applied along with the percentage error and the absolute error. Units are in W/g^2 unless stated explicitly.

WSU	GPZ4	$1.38 \times 10^{-5} \text{ T}$		$2.06 \times 10^{-5} \text{ T}$	
		100 kHz	200 kHz	100 kHz	200 kHz
	Statistical Mean	0.00694	0.01419	0.02245	0.04807
	Standard Error	± 0.00025	± 0.00020	± 0.00023	± 0.00111
	% Error	3.7	1.4	1.0	2.3

and the standard error in the rate of heating is obtained from

$$\delta \left(\frac{\Delta T}{\Delta t} \right) = \frac{\sigma}{\sqrt{N}}. \quad (6.2)$$

where N is the number of times each experiment was performed. Consequently, the percentage error was calculated from the heating rate and the standard error associated with the heating rate.

6.2 WSU

6.2.1 GPZ4

GPZ4 data was plotted in Figure 6.3. This figure also incorporates the best-fit curve drawn in blue. The peak heating rate was obtained from the fit parameter for GPZ4 and the results of the runs are summarized in Table 6.1. The absolute error and the percentage error are both displayed for each set of data.

6.2.2 GPZ5

A graph containing the data for sample GPZ5 was drawn in Figure 6.4. The frequency was altered from 100 kHz to 200 kHz for each magnetic field. The fitting curve is also drawn in blue color. The optimal heating rate was extracted from the best fit curve and is displayed in Table 6.2.

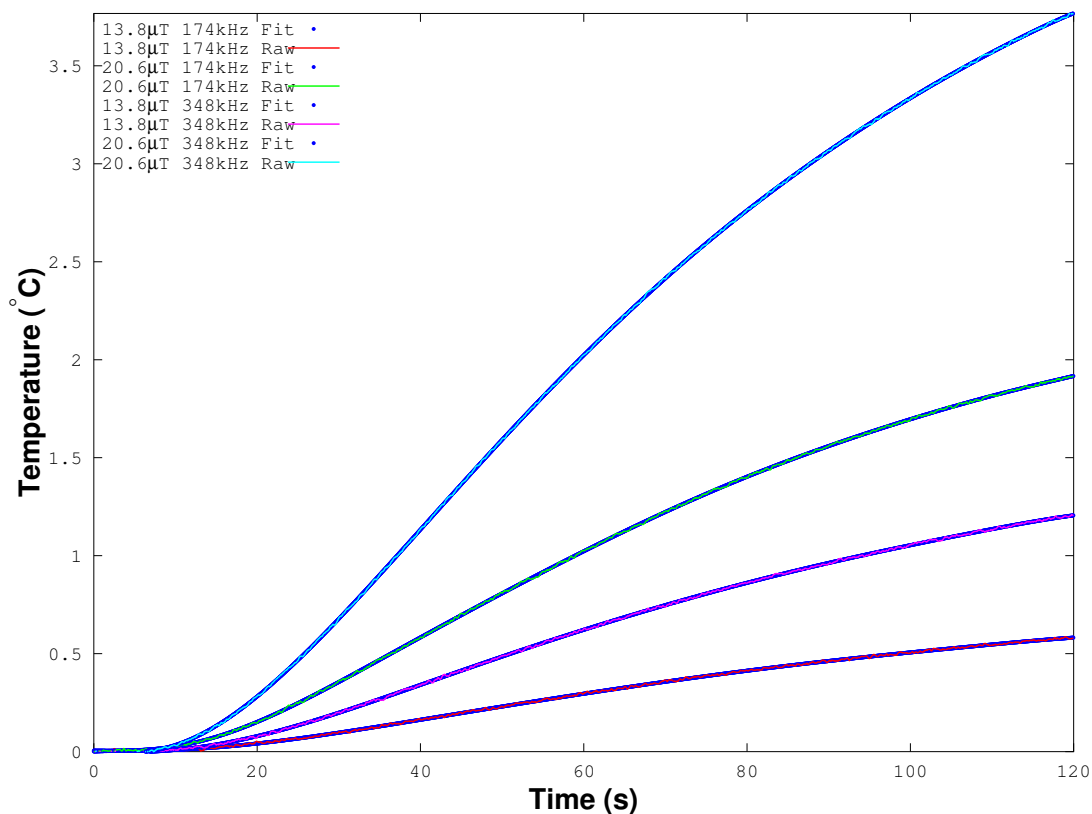


Figure 6.3: Heating of GPZ4 magnetic nanoparticles - The plotted data and fitted curve for the 4 different settings are shown.

Table 6.2: The average heating rate of GPZ5 when different magnetic fields of dissimilar frequencies are applied along with the percentage error and the absolute error. Units are in W/g^2 unless stated explicitly.

WSU	GPZ5	$1.38 \times 10^{-5} \text{ T}$		$2.06 \times 10^{-5} \text{ T}$	
		100 kHz	200 kHz	100 kHz	200 kHz
	Statistical Mean	0.00458	0.00920	0.01782	0.03238
	Standard Error	± 0.00005	± 0.00018	± 0.00016	± 0.00011
	% Error	1.0	2.0	0.9	0.3

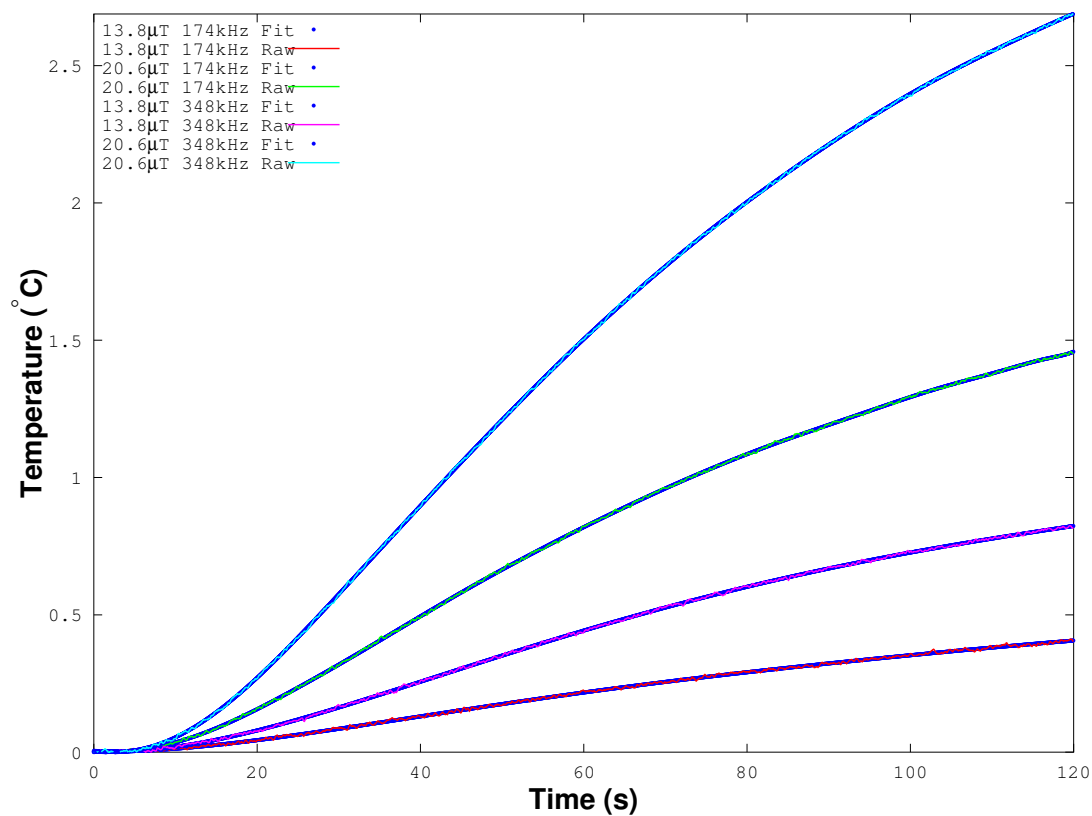


Figure 6.4: Heating of GPZ5 MNP - The plotted data and fitted curve for the 4 different settings are shown.

6.2.3 GPZ8

The data for sample GPZ8 was plotted in Figure 6.5. In the same figure, the best-fit (blue) curve is also shown. From the latter, the maximum heating rate was obtained for GPZ8 and the average of the runs is summarized in Table 6.3.

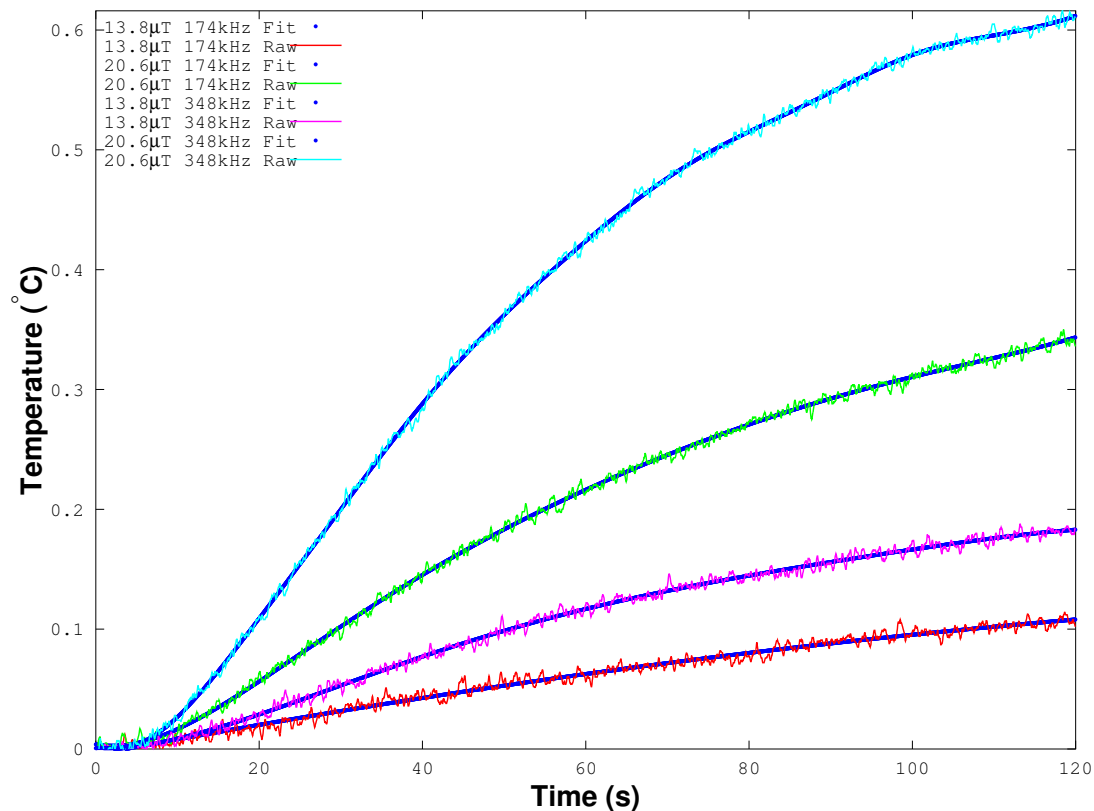


Figure 6.5: Heating of GPZ8 MNP - The plotted data and fitted curve for the 4 different settings are shown.

6.2.4 GPZ11

The acquired data was plotted for different frequencies and different magnetic field as depicted in Figure 6.4. Figure 6.4 also contains the fitted curves from which $\Delta T/\Delta t$ was obtained. This data is shown in Table 6.6 along with the percentage error and the standard error of the average heating rate.

Table 6.3: The mean heating rate of sample GPZ8 when different magnetic fields of unlike frequencies are applied along with the percentage error and the absolute error. Units are in W/g^2 unless stated explicitly.

WSU	GPZ8	$1.38 \times 10^{-5} \text{ T}$		$2.06 \times 10^{-5} \text{ T}$	
		100 kHz	200 kHz	100 kHz	200 kHz
	Statistical Mean	0.00216	0.00303	0.00560	0.00911
	Standard Error	± 0.00078	± 0.00053	± 0.00078	± 0.00013
	% Error	36.0	17.4	13.9	1.5

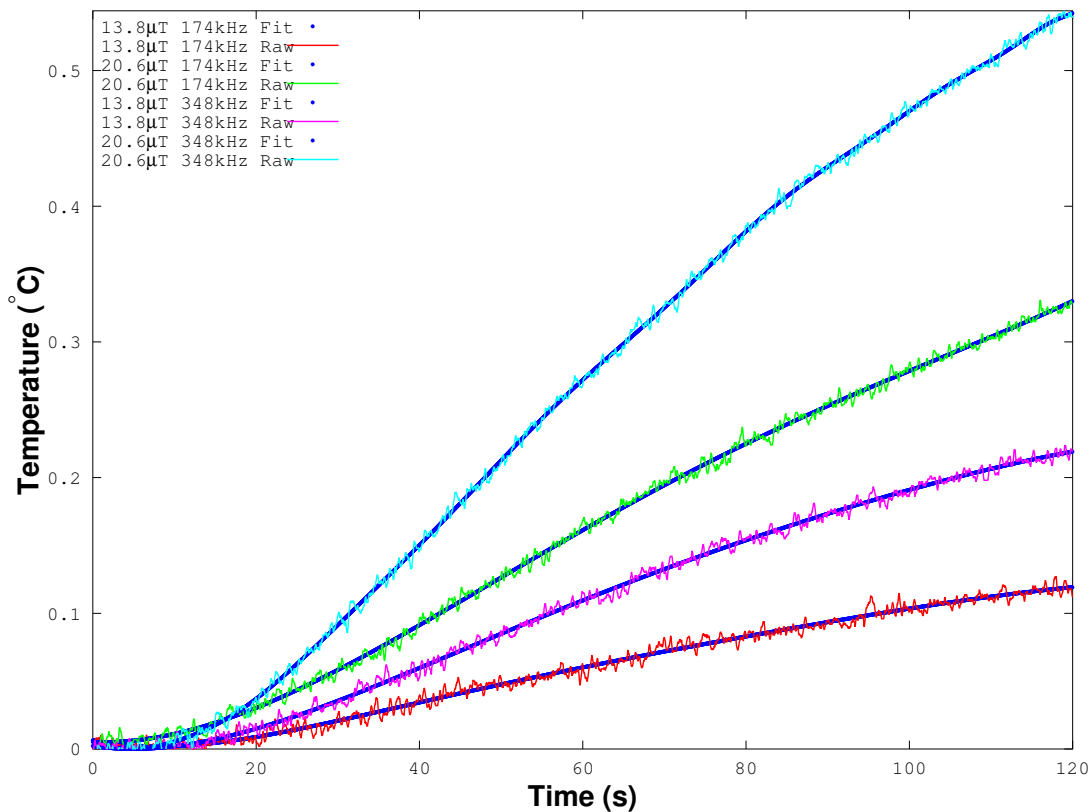


Figure 6.6: Heating of GPZ11 MNP - The plotted data and fitted curve for the 4 different settings are shown.

Table 6.4: The average heating rate of GPZ11 when different magnetic fields of dissimilar frequencies are applied along with the percentage error and the absolute error. Units are in W/g^2 unless stated explicitly.

WSU	GPZ11	$1.38 \times 10^{-5} \text{ T}$		$2.06 \times 10^{-5} \text{ T}$	
		100 kHz	200 kHz	100 kHz	200 kHz
	Statistical Mean	0.00138	0.00246	0.00347	0.00630
Standard Error	± 0.00001	± 0.00007	± 0.00004	± 0.00004	
% Error	0.8	2.9	1.2	0.6	

Table 6.5: The mean heating rate of sample GPZ4 when different magnetic fields of unlike frequencies are applied along with the percentage error and the absolute error. Units are in W/g^2 unless stated explicitly.

QU	GPZ4	25.2 A	50.4 A	75.6 A	100.8 A
		314.0 kHz	310.0 kHz	299.0 kHz	294.0 kHz
	Statistical Mean	0.2535	1.4169	3.4721	7.4364
	Standard Error	0.0062	0.0205	0.0178	0.0754
% Error	2.4	1.4	0.5	1.0	

6.3 QU

The same manipulation is done for the data obtained at Queen's University namely fitting a curve to the data sets and the calculate the initial gradient of the fitted curve. The results are presented in the following subsections.

6.3.1 GPZ4

GPZ4 data was plotted in Figure 6.7. This figure also incorporates the best-fit curve drawn in blue. The peak heating rate was obtained from the fit parameter for GPZ4 and the results of the runs are summarized in Table 6.5. The absolute error and the percentage error are both displayed for each set of data.

6.3.2 GPZ5

A graph containing the data for sample GPZ5 was drawn in Figure 6.8. The frequency was altered from 100 kHz to 200 kHz for each magnetic field. The

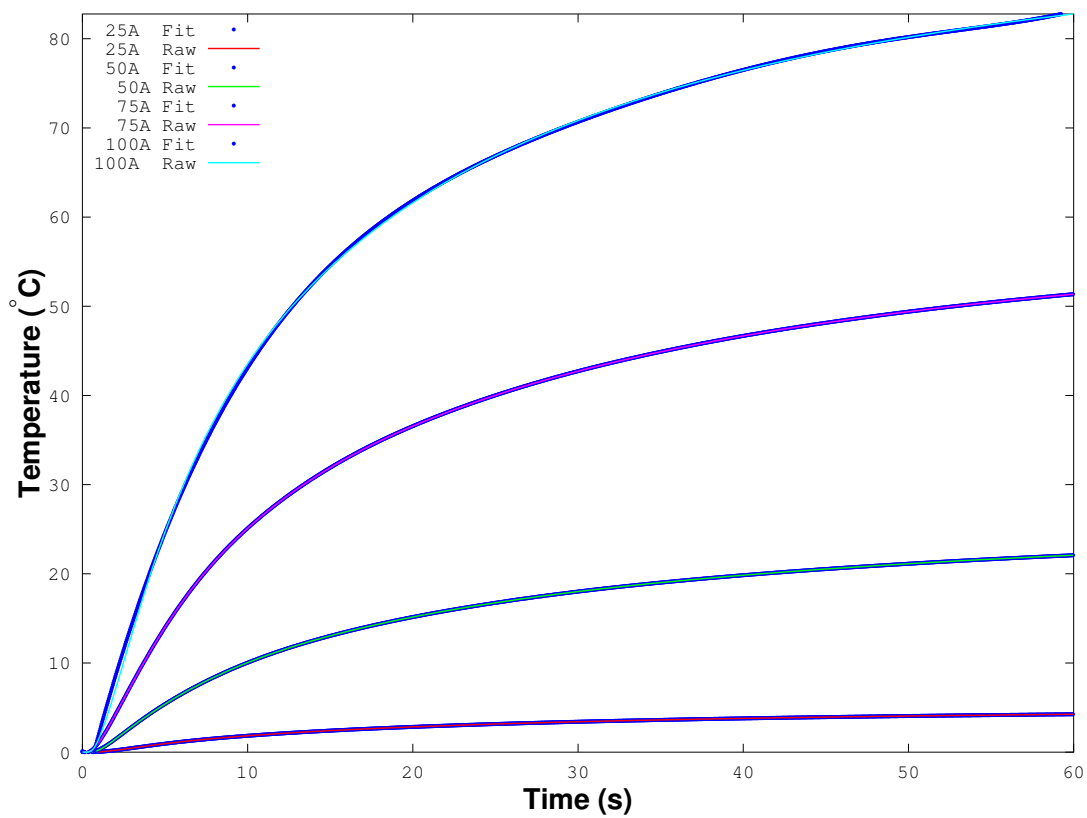


Figure 6.7: Heating of GPZ4 MNP - The plotted data and fitted curve for the 4 different settings are shown.

fitting curve is also drawn and is shown in blue color. The optimal heating rate was extracted from the best fit curve and is displayed in Table 6.6.

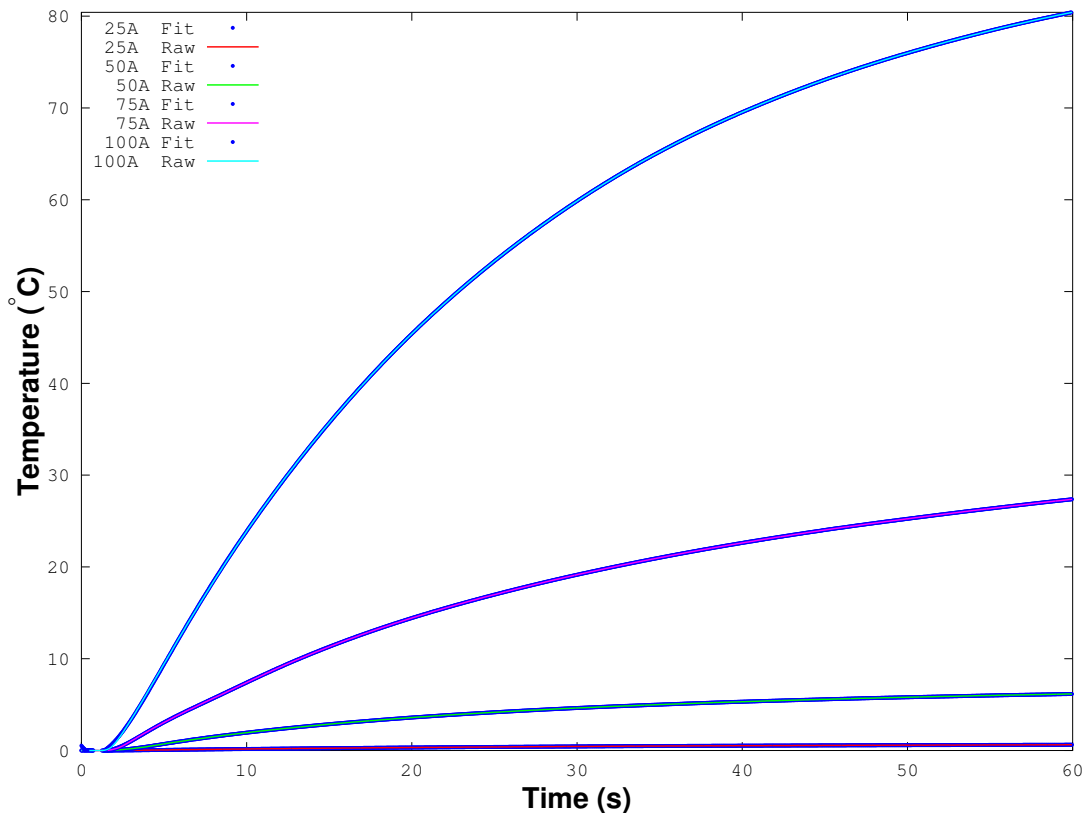


Figure 6.8: Heating of GPZ5 MNP - The plotted data and fitted curve for the 4 different settings are shown.

6.3.3 GPZ8

The data for sample GPZ8 was plotted as shown in Figure 6.9. In the same figure, the best-fit (blue) curve is also shown. From the latter, the maximum heating rate was obtained for GPZ8 and the average of the runs is summarized in Table 6.7.

Table 6.6: The mean heating rate of sample GPZ5 when different magnetic fields of unlike frequencies are applied along with the percentage error and the absolute error. Units are in W/g^2 unless stated explicitly.

QU	GPZ5	25.2 A 314.0 kHz	50.4 A 310.0 kHz	75.6 A 299.0 kHz	100.8 A 294.0 kHz
	Statistical Mean		0.0228	0.2479	1.0069
Standard Error		0.0010	0.0179	0.0437	0.1664
% Error		4.4	7.2	4.3	5.7

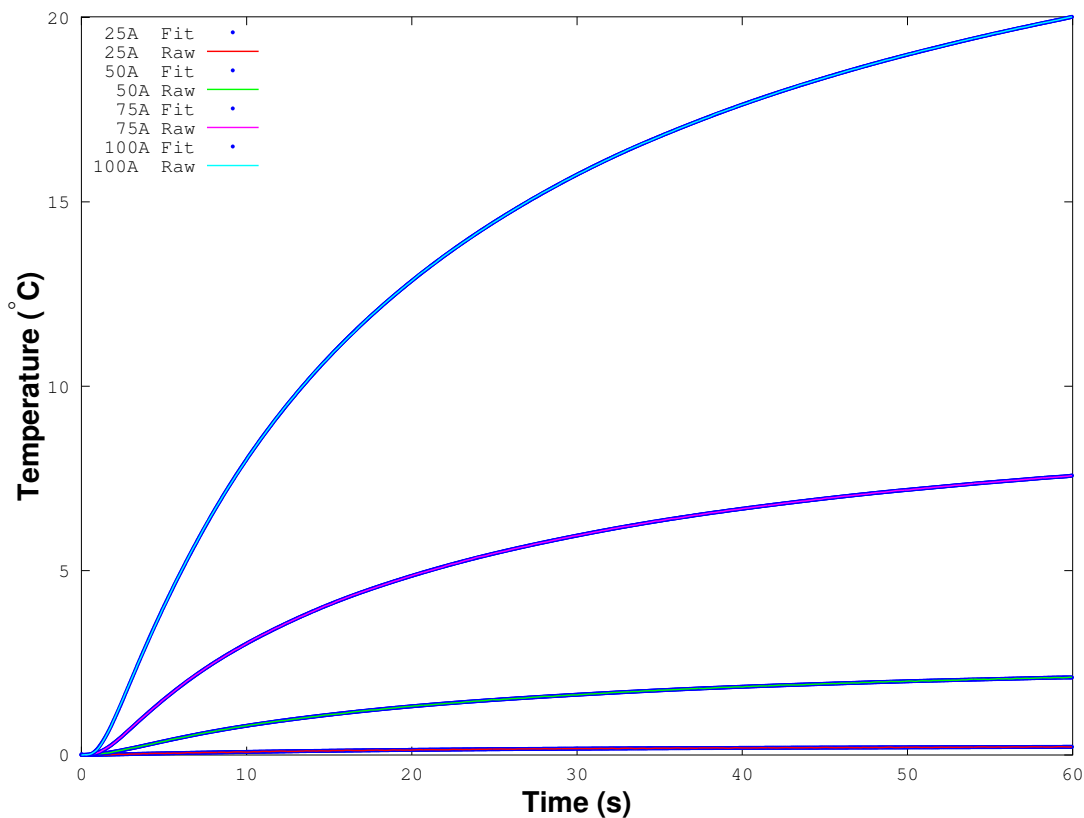


Figure 6.9: Heating of GPZ8 MNP - The plotted data and fitted curve for the 4 different settings are shown.

Table 6.7: The mean heating rate of sample GPZ8 when different magnetic fields of unlike frequencies are applied along with the percentage error and the absolute error. Units are in W/g^2 unless stated explicitly.

QD	GPZ8	25.2 A 314.0 kHz	50.4 A 310.0 kHz	75.6 A 299.0 kHz	100.8 A 294.0 kHz
	Statistical Mean	0.0111	0.0998	0.4059	1.0557
Standard Error	0.0001	0.0023	0.0044	0.0277	
% Error	0.9	2.3	1.1	2.6	

Table 6.8: The mean heating rate of sample GPZ11 when different magnetic fields of unlike frequencies are applied along with the percentage error and the absolute error. Units are in W/g^2 unless stated explicitly.

QD	GPZ11	25.2 A 314.0 kHz	50.4 A 310.0 kHz	75.6 A 299.0 kHz	100.8 A 294.0 kHz
	Statistical Mean	0.0025	0.0112	0.0296	0.0688
Standard Error	0.0002	0.0006	0.0011	0.0057	
% Error	8.0	5.4	3.7	8.3	

6.3.4 GPZ11

The acquired data was plotted for different frequencies and different magnetic field as depicted in Figure 6.4. Figure 6.10 also contains the fitted curves from which $\Delta T/\Delta t$ was obtained. This data is shown in Table 6.8 along with the percentage error and the standard error of the average heating rate.

6.4 Normalized SPL

The equation for the specific power loss as derived in Chapter 4 is

$$SPL = c \frac{\Delta T}{\Delta t} \quad (6.3)$$

However, since the mass used in the experiments is not equal, the SPL has to be reduced by mass to account for the differences in the mass. This new quantity

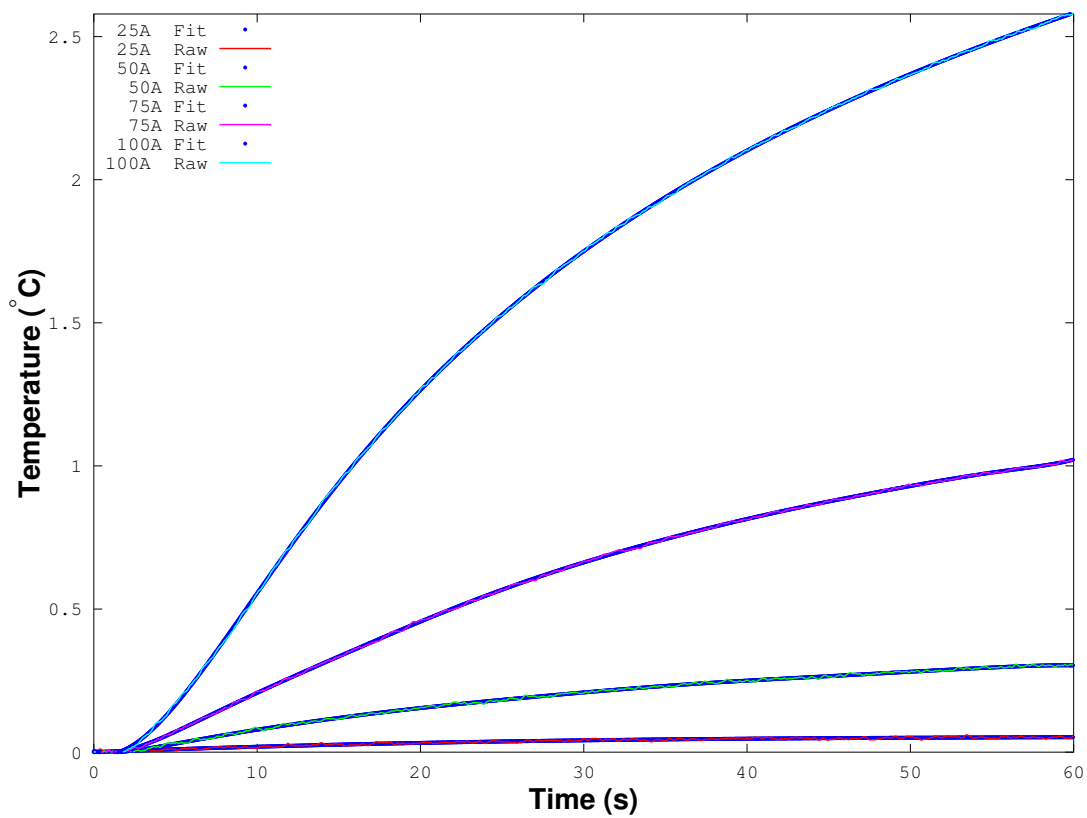


Figure 6.10: Heating of GPZ11 MNP - The plotted data and fitted curve for the 4 different settings are shown.

Table 6.9: The molar mass and specific heat capacities of some ferrites is given as measured at a temperature of 25.16 °C (298.16 K).

Name	Molar Mass (g)	c_p (cal/mol-°C)	c_p (J/g-°C)
NiFe ₂ O ₄	234.39	34.81	0.6214
ZnFe ₂ O ₄	241.08	32.99	0.5726
CoFe ₂ O ₄	234.64	36.53	0.6514
Ni _{0.5} Zn _{0.5} Fe ₂ O ₄	237.73	38.20	0.6809
Co _{0.4} Ni _{0.4} Zn _{0.2} Fe ₂ O ₄	235.617	?	?

will be called SPL^* with $Jkg^{-2}s^{-1}$ or Wg^{-2} as its units:

$$SPL^* = \frac{c}{m_{NP}} \frac{\Delta T}{\Delta t} \quad (6.4)$$

Since the specific heat capacity of the materials is crucial in the determination of the value of SPL, great care was taken to obtain exact values of the heat capacity. Literature [56, 57, 58, 59, 60, 61] was consulted to obtain precise values for the heat capacities which is summarized in Table 6.9.

Unfortunately, we could not find a value for the specific heat capacity of Co_{0.4}Ni_{0.4}Zn_{0.2}Fe₂O₄ from literature but we can try to estimate the value using the theory given in [57]:

$$c_p = c_p^{lattice} + c_p^{magnetic} \quad (6.5)$$

where $c_p^{lattice}$ is the heat capacity due to the contribution of the lattice vibrations and $c_p^{magnetic}$ is the contribution of the magnetic contribution to the specific heat capacity.

The lattice vibrational contribution is determined from vibrational frequencies and depends also on Einstein's and Debye's functions. Since the vibrational frequencies for the ferrites are approximately the same, we can roughly say that they are going to be more or less equal. The magnetic contribution depends on the exchange interaction energy between cation moments in tetrahedral and octahedral sites of the spinel lattice. Hence if we plot a graph of the specific heat capacity of the sample in question to the saturation magnetization as given in Table 6.10, we can estimate a value of the specific heat capacity of Co_{0.4}Ni_{0.4}Zn_{0.2}Fe₂O₄.

This is done by fitting a curve to the points and the value of the heat capacity is extracted (Figure 6.11). From our extrapolation, the specific heat capacity of $\text{Co}_{0.4}\text{Ni}_{0.4}\text{Zn}_{0.2}\text{Fe}_2\text{O}_4$ was found to be $0.66657 \text{ J/g}\cdot^\circ\text{C}$. All the contributions to the heat capacity are not being taken into consideration, so this is an approximation and there will be an error associated to this value which from the course of the heat capacities, the error will be approximately $\pm 0.05 \text{ J/g}\cdot^\circ\text{C}$.

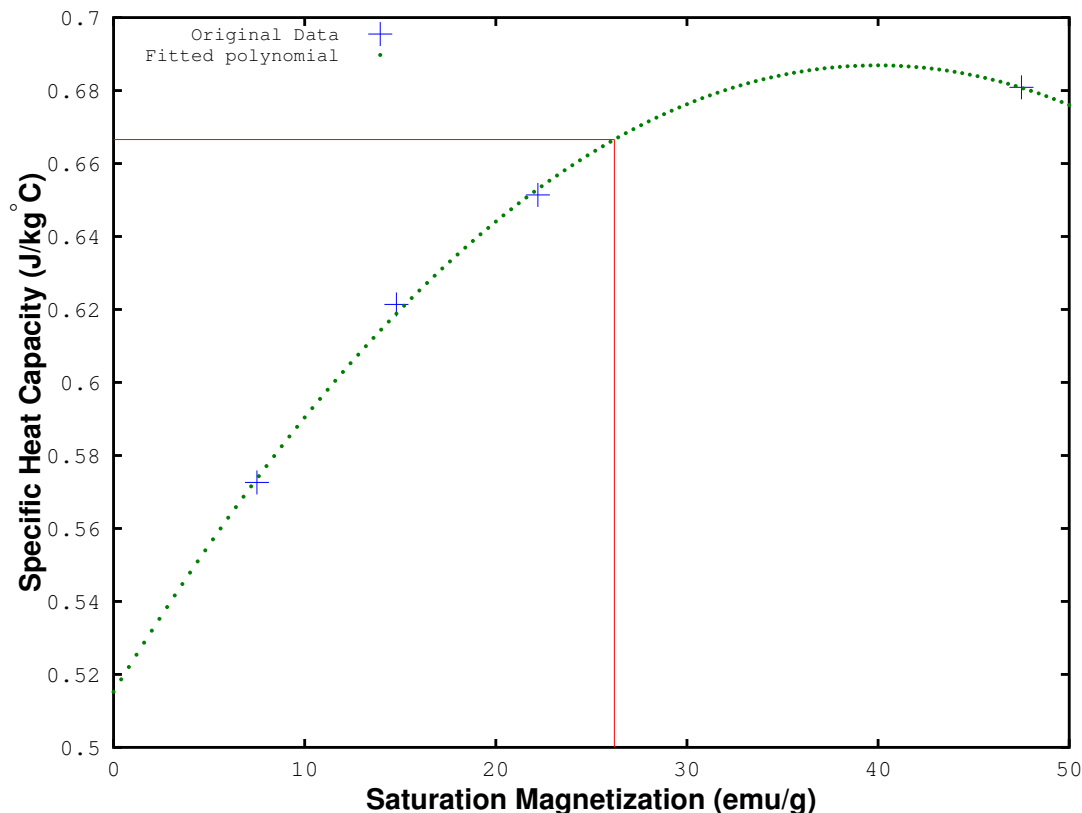


Figure 6.11: Heat capacity vs. saturation magnetization - The specific heat capacity of 4 ferrites against the magnetization is plotted and a curve is fitted to the points to extract the heat capacity of the fifth ferrite.

The error associated with the value of the SPL normalized by mass, SPL^* was calculated using the propagation of errors and the equation used to calculate

Table 6.10: The saturation magnetization and specific heat capacities of some ferrites is given as measured at a temperature of 25.16 °C (298.16 K).

Name	M_s (emu/g)	c_p (J/g-°C)
NiFe ₂ O ₄	14.8	0.6214
ZnFe ₂ O ₄	7.5 [62]	0.5726
CoFe ₂ O ₄	22.2	0.6514
Ni _{0.5} Zn _{0.5} Fe ₂ O ₄	47.5	0.6809
Co _{0.4} Ni _{0.4} Zn _{0.2} Fe ₂ O ₄	26.2	0.6667

the error in the value of SPL^* is:

$$\Delta SPL^* = \sqrt{\left(\frac{\partial(SPL^*)}{\partial c} \Delta c\right)^2 + \left(\frac{\partial(SPL^*)}{\partial m} \Delta m\right)^2 + \left(\frac{\partial(SPL^*)}{\partial \dot{T}} \Delta \dot{T}\right)^2} \quad (6.6)$$

$$= \sqrt{\left(\frac{\dot{T}}{m} \Delta c\right)^2 + \left(-\frac{c\dot{T}}{m^2} \Delta m\right)^2 + \left(\frac{c}{m} \Delta \dot{T}\right)^2} \quad (6.7)$$

WSU

Table 6.11: The normalized SPL values as a function of magnetic field and frequency. Units are in W/g^2 unless stated explicitly.

Sample	$1.38 \times 10^{-5} \text{ T}$		$2.06 \times 10^{-5} \text{ T}$	
	178.4 kHz	348.0 kHz	178.4 kHz	348.0 kHz
GPZ4	0.15749±0.00946	0.322088±0.004855	0.50946±0.00925	1.09101±0.016467
GPZ5	0.098571±0.028764	0.197938±0.014859	0.38329±0.028987	0.696393±0.052275
GPZ8	0.03869±0.01403	0.05427±0.00103	0.1003±0.0140	0.1631±0.0027
GPZ11	0.02966±0.00117	0.05267±0.00083	0.07430±0.00148	0.1349±0.0021

QU

Table 6.12: The normalized SPL values are given as a function of current and frequency. Units are in W/g^2 unless stated explicitly.

Sample	25.2 A	50.4 A	75.6 A	100.8 A
	314 kHz	310 kHz	299 kHz	294 kHz
GPZ4	2.8769±0.0821	16.0792±0.3323	39.4027±0.6163	84.391±1.5123
GPZ5	0.2240±0.0195	2.4378±0.2540	9.9013±0.8583	28.6634±2.7020
GPZ8	0.1243±0.0124	1.346±0.0769	5.989±0.1108	17.00±0.5340
GPZ11	0.02345±0.0020	0.1033±0.0056	0.2726±0.0106	0.6343±0.0534

The normalized SPL values are tabulated in Table 6.11 and Table 6.12 for data at Queen’s University and Wright State University, respectively.

When the normalized SPL is plotted against the current (Figure 6.12), we observe a high value for the specific power loss for a higher current (eventually magnetic field) in all the samples. From this plot, we deduce that GPZ4 has a higher normalized SPL for all current values followed by GPZ5. This experiment was performed at Queen’s University in Belfast with a frequency of 300 kHz. The same trend was observed in Wright State University’s lab when the samples were subjected to an alternating magnetic field. A higher magnetic field produced a higher SPL* value if the frequency was kept constant (cf. Table 6.11).

We can conclude that the magnetic field plays a crucial role in the magnitude of the value of the specific loss power.

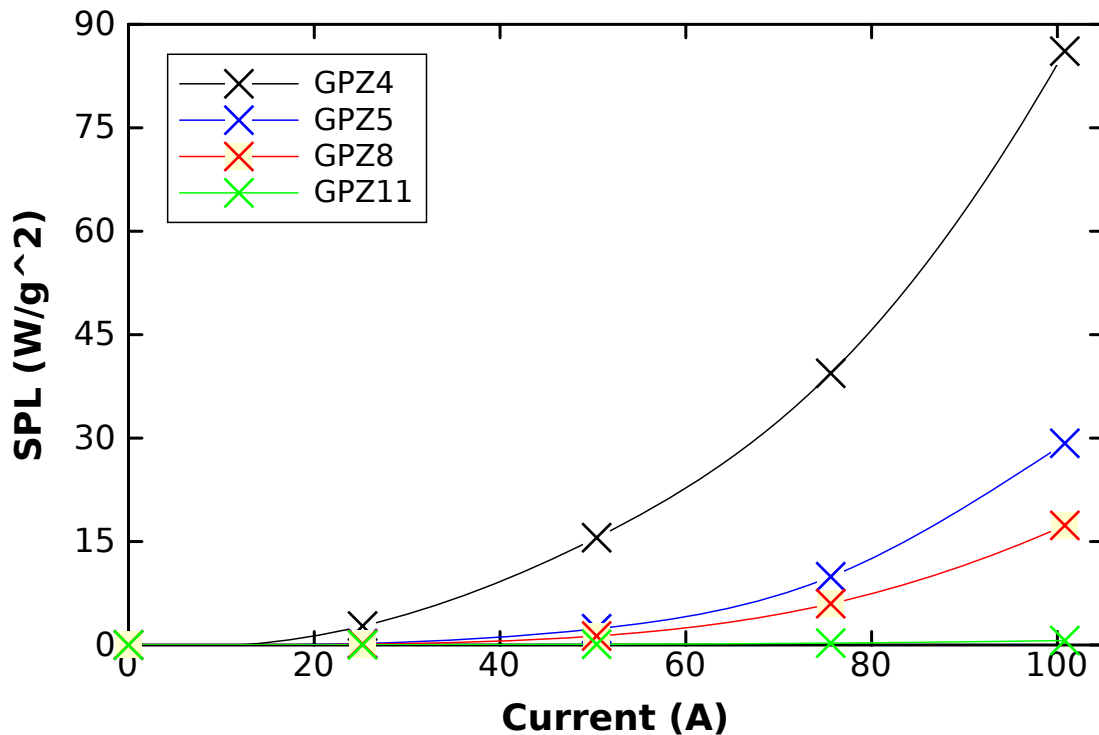


Figure 6.12: Normalized SPL vs. current - The normalized SPL of 4 ferrites was plotted against the current.

6.5 Magnetic Field Dependence of SPL

In the previous section, we have concluded that a higher magnetic field produces a higher SPL* value. So far, we do not know the exact relationship between the magnetic field and SPL. To get an insight of this dependence, the effect of increasing the magnetic field intensity on the SPL was investigated. The magnetic field inside the coil was increased from 1.38×10^{-5} T to 2.06×10^{-5} T by a factor of 1.5 while the frequency was kept constant at 174 kHz. This was repeated for a higher frequency of 348 kHz. The ratio of SPL* at 2.06×10^{-5} T to 1.38×10^{-5} T is plotted for data collected at WSU and is shown in Figure 6.13.

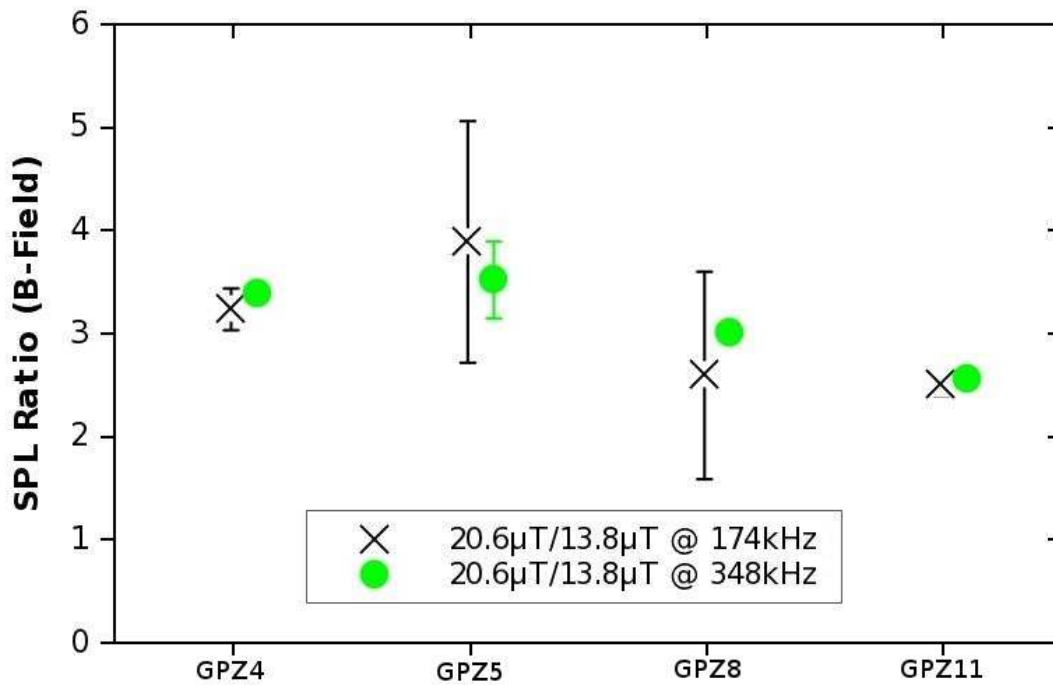


Figure 6.13: Magnetic field effect on SPL - The ratio of SPL at 2.06×10^{-5} T to 1.38×10^{-5} T vs. the samples.

The same analysis was done with data from QU but instead of the magnetic field, the current was used while the frequency was locked at 300 kHz. In this case, the ratio of the value of the SPL* at 50 A to 25 A is plotted. The ratio of

the value of the SPL* at 100 A to 50 A is also plotted. The outcome is given in Figure 6.14.

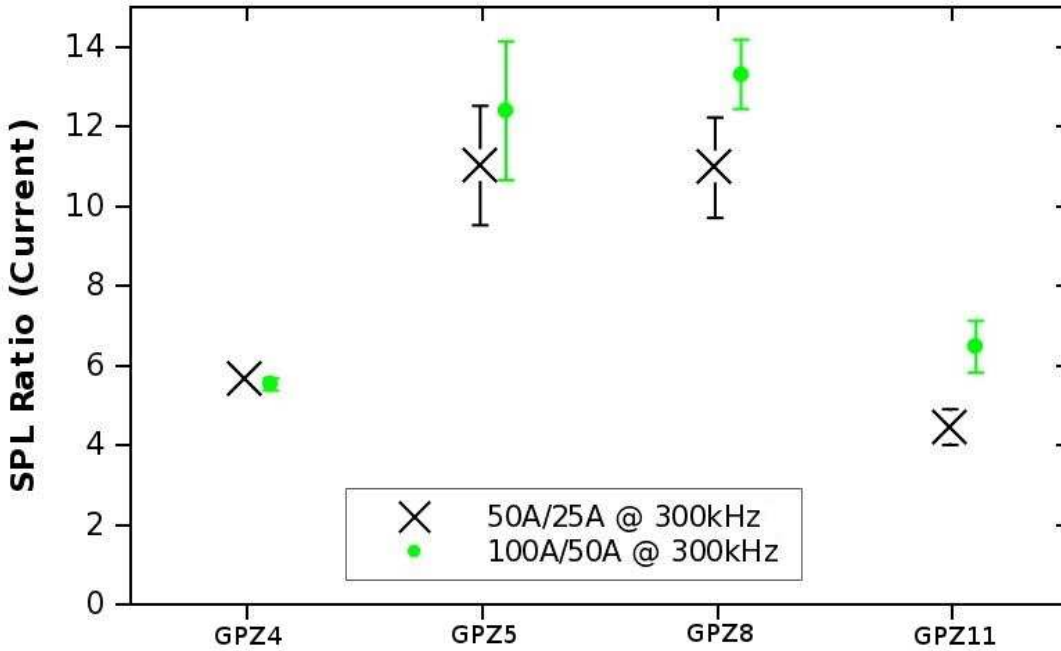


Figure 6.14: Current effect on SPL - The ratio of the value of SPL for two different current sets for the 4 ferrites.

Unfortunately, from both plots, a relationship between the magnetic field and SPL could not be found for all the materials. Increasing the intensity of the magnetic field increases the value of the SPL but this raise is specific to the material. From the two plots, we deduct that tuning up the field by a factor of 1.5 increases the SPL* value by the same amount for each material. For example, from Figure 6.14, for GPZ4, the ratio of the SPL* when the current is increased from 25 A to 50 A and from 50 A to 100 A is the same (roughly 5.6). Hence in this case, if the current is increased to, say 200 A, we can obtain the value of the SPL by multiplying the SPL* value at a current of 100 A by 5.6 for GPZ4. This ratio is around 11.5 for GPZ5 when doubling the current.

6.5.1 Estimation of the Magnetic Field at Queen's University

6.6 Frequency Dependence of SPL

It is apparent from Table 6.11 that increasing the frequency increases the value of the normalized SPL. The same analysis is done as in the previous section namely, the ratio of the SPL* when the frequency is doubled (from 174 kHz to 348 kHz at WSU) is looked into for all the samples. Figure 6.15 gives the frequency

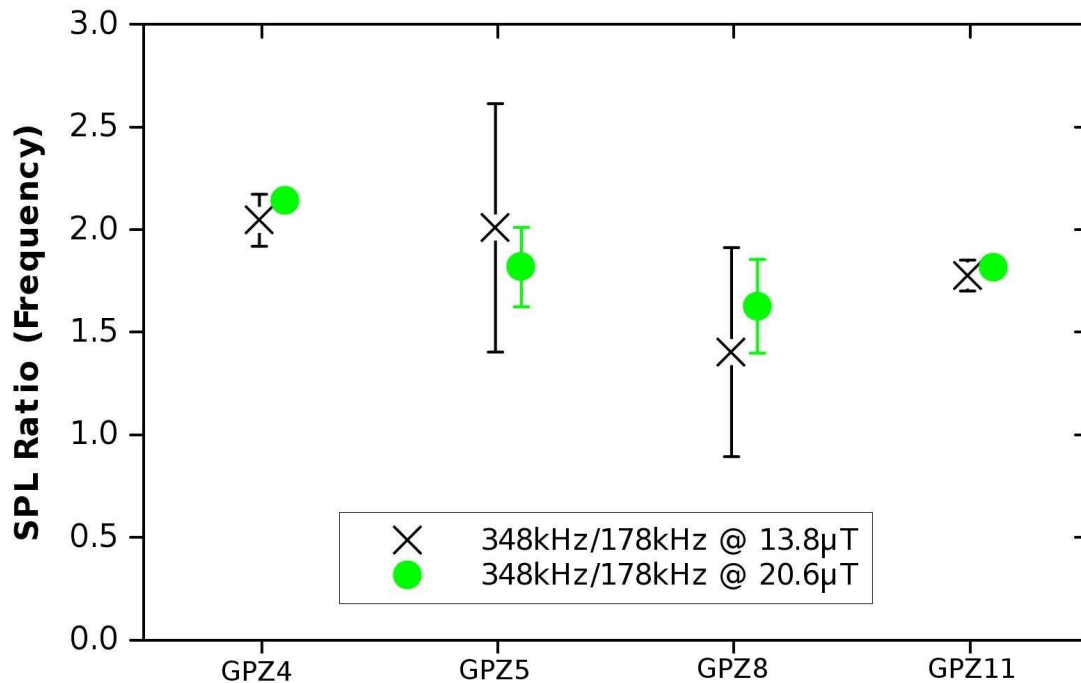


Figure 6.15: Frequency effect on SPL - The ratio of the value of SPL for two different frequencies for the 4 ferrites at two values of magnetic fields.

dependence of the different ferrites on the value SPL*. If we fit a line through the points, Figure 6.16 is produced. From Figure 6.16, when the frequency is doubled, the SPL is also doubled within errors irrespective of the material. This is a very important result since the SPL has a proportional relationship with the

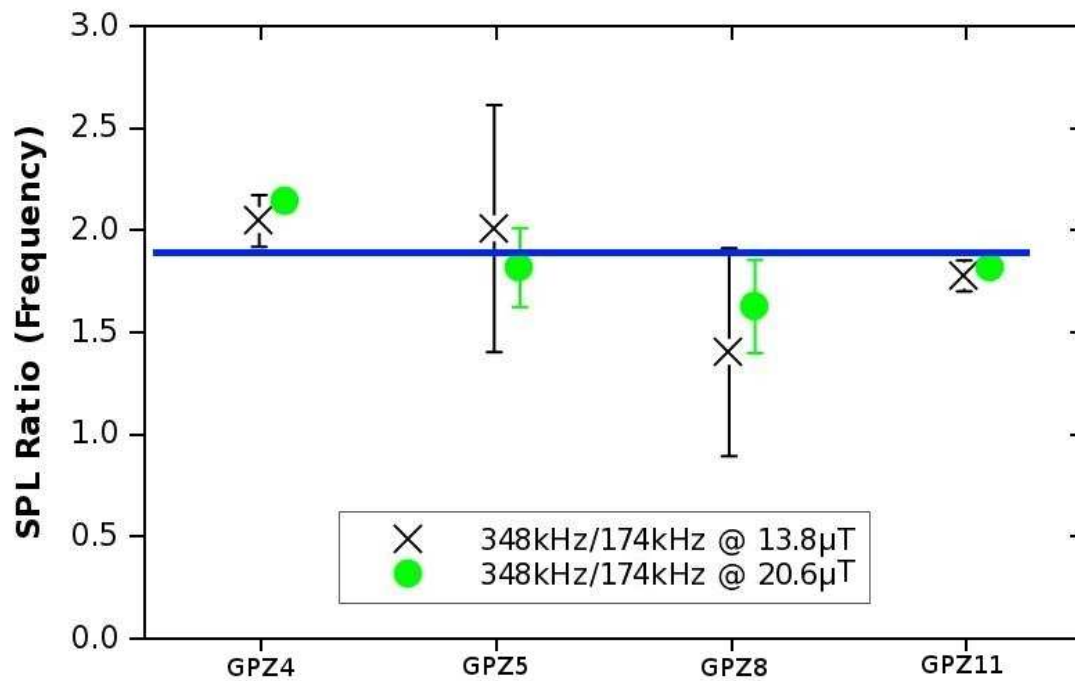


Figure 6.16: Frequency significance on SPL - This is a reproduction of Figure 6.15 with a straight line fitted through the points.

frequency of the applied magnetic field and this also verifies the equation which was derived in Chapter 3.

$$P = f \oint H dB \quad (6.8)$$

6.7 Magnetic Property Dependence of SPL

The magnetic properties (saturation magnetization, remanent magnetization and coercive force) have also been plotted for each sample to see the dependence of the SPL with these quantities. The following sections contains the plots of the SPL against the remanent magnetization, saturation magnetization and coercivity, respectively.

6.7.1 Remanent Magnetization

The remanent magnetization, M_R is the left-over magnetization after an applied magnetic field has been reduced to zero.

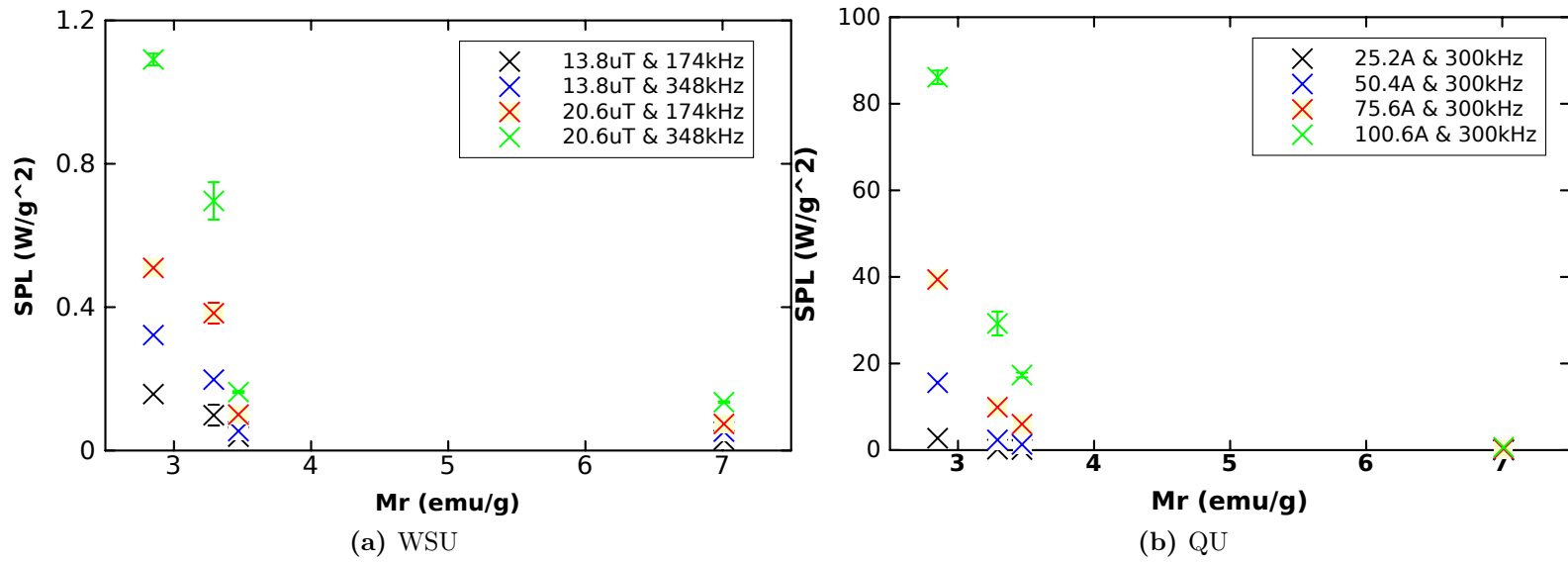


Figure 6.17: SPL vs. remanent magnetization - The SPL is plotted as a function of the remanent magnetization using two different set-ups.

6.7.2 Saturation Magnetization

As a reminder, the saturation magnetization, M_S is the maximum induced magnetic moment that is possible for a given material with the application of a magnetic field. Beyond this field no further increase in magnetization occurs.

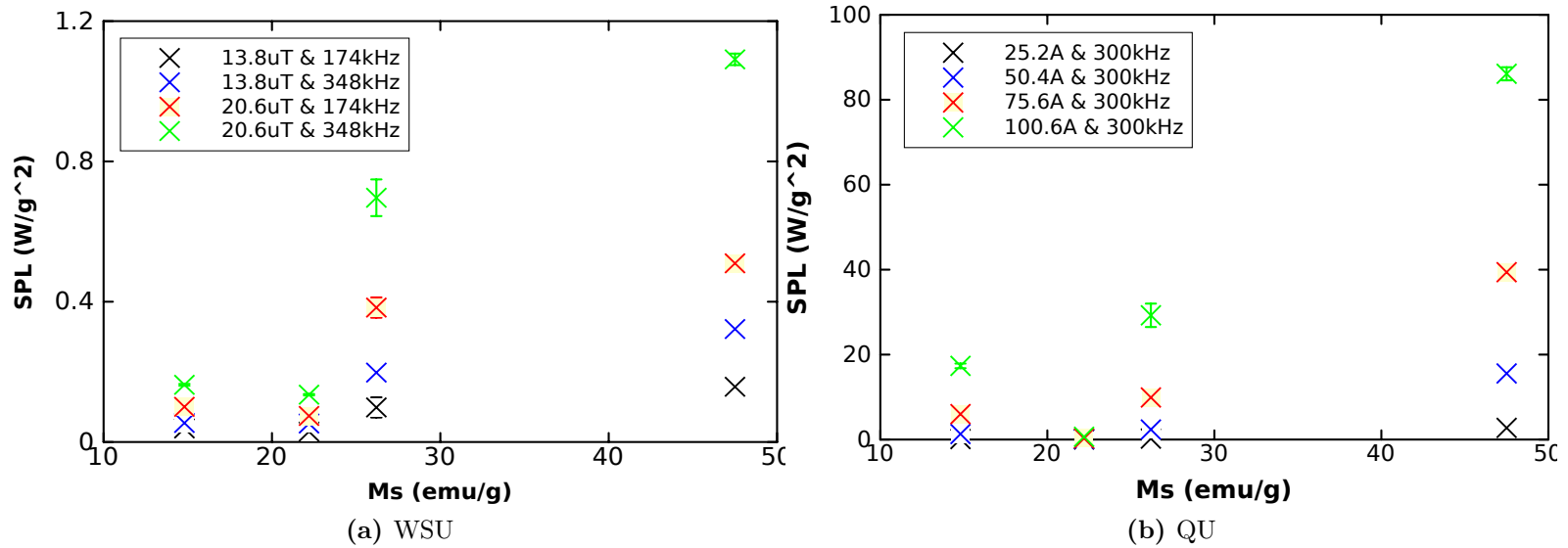


Figure 6.18: SPL vs. saturation magnetization - The SPL against the saturation magnetization is plotted in two different labs.

6.7.3 Coercive Forces

The coercivity, H_c is the reverse field which, when applied and then removed, reduces the magnetization to zero after the magnetization has been saturated.

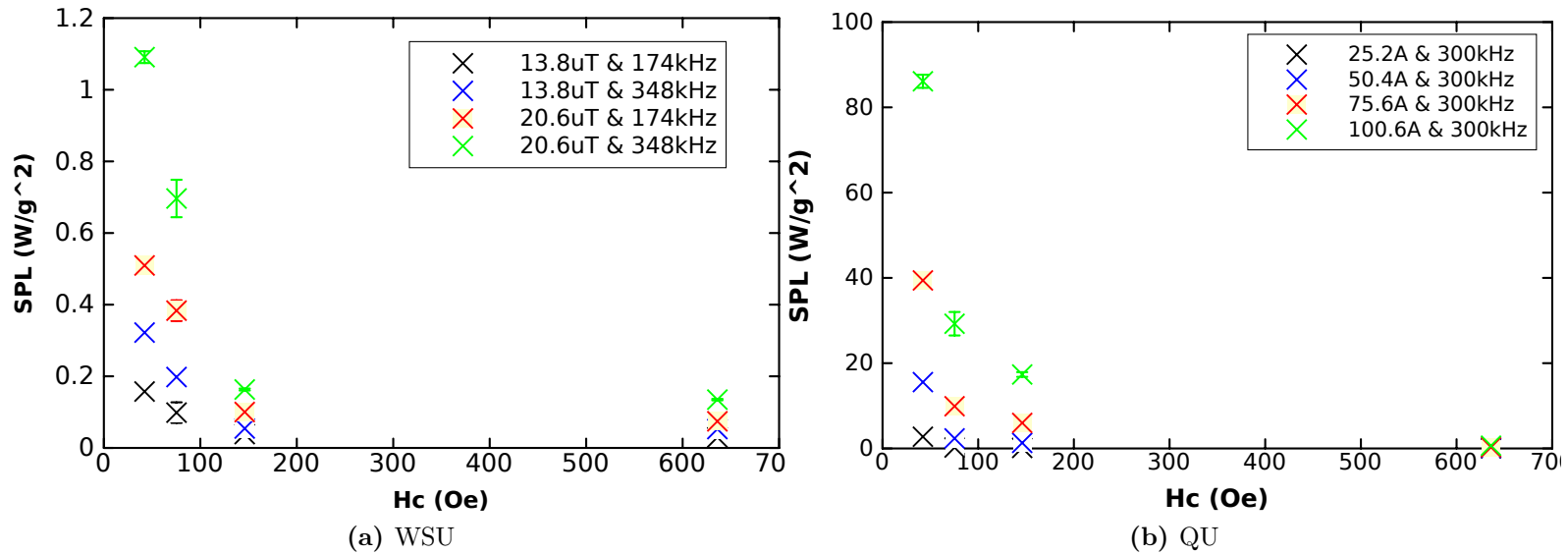


Figure 6.19: SPL vs. coercivity - The SPL is plotted against the coercive forces in two different labs.

From the previous graphs, we can see some dependence on the value of the normalized SPL and the magnetic quantities.

We can associate an inverse relationship between the remanent magnetization and the SPL of the samples as seen on Figure 6.17 in both labs. As the remanent magnetization increases, the value of SPL decreases. This is the case for all magnetic fields and frequencies. They all follow the same pattern of an increase in the value of SPL when the remanent magnetization. From this, we can conclude that to get a higher value of SPL, the optimum sample that is needed is one which has a low remanent magnetization.

If we examine Figure 6.18, we cannot find any visible trend that relate the saturation magnetization and the SPL as the points are randomly distributed on the curve.

Looking closely at Figure 6.19, we observe the same pattern as Figure 6.17, that is an inverse relationship between the SPL value and the coercive forces. This is both the case for the experiment performed at WSU and QU. As previously the case, the inverse relationship maintains for all values of magnetic fields or frequency ranges used. Again, to get a high SPL, the sample must have a low coercivity.

6.8 Grain Size Effect

A. Habib et al., [63] have investigated how SPL varies with the average size of the several samples and their result is given in Figure 6.20. As we can observe, the value of SPL increases or decreases depending on the material used with increase in the average size of the particle. In this present research, we have not examine the effect of the core diameter of the nanoparticles on the value of SPL by doing additional syntheses but if we base our analysis on the fact that our sample is closer to maghemite, then with increase in size, the value of SPL decreases. Since GPZ4, 5, 8 and 11 have average diameter of 48.7, 46, 42.9, and 34.5 nm (cf. Table 5.1) we expect the value of the SPL to be less for GPZ4 as compared to GPZ11. Hence the value of the SPL calculated for GPZ4 is an underestimate if reduced to the size of 34.5 nm. Even though, this is the case, GPZ4 still has the highest

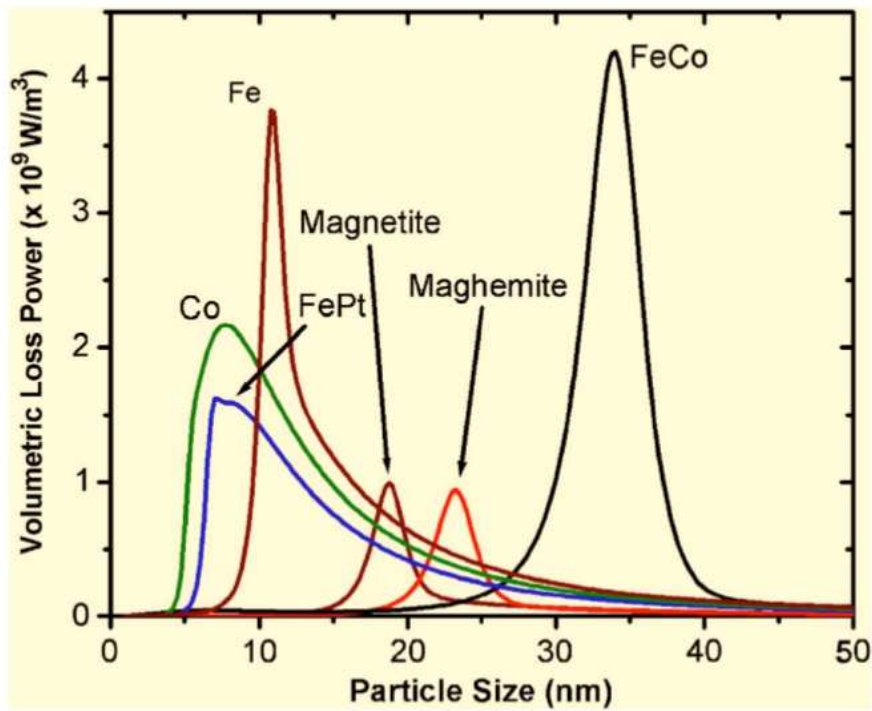


Figure 6.20: SPL vs. grain size - The variation of the SPL as the mean diameter is diversified.

value for the SPL. We may conclude that the grain size is not playing a decisive role in our case.

6.9 Discrepancy between Measured Values

If we refer back to Table 5.1 from Chapter 5, we can see that there is a discrepancy between the last column (Joule losses or energy loss density) of that table and our measured values of the SPL which is synonymous to the power loss. GPZ11 has the highest Joule Loss value (12250 J/m^3) when it was measured by VSM but when measured using by a calorimetric method, it had the lowest SPL. GPZ8 has the second highest Joule Loss value (6182 J/m^3) but still, it was far from having the highest SPL among our samples.

This is unnatural since SPL and power loss density refer to the same physical quantity and they should follow the same tendency. One explanation for this is that the magnetic field produced by the VSM is huge and the sample is being magnetized to its full extent whereas the magnetic field that is used in our systems is a fraction of that of the VSM. Hence although GPZ has the highest power loss density as measured by the VSM, we are unable to magnetize to a good extent. This explanation is more convincing with the aid of Figure 6.21. Hence, a material with a low coercivity will be fully magnetized even though the magnetic field is small whereas a magnetic material with a large coercivity will not be fully magnetized although the hysteresis curve is very wide in nature meaning a large value for the power loss density. For example, if the applied magnetic field is shown as in Figure 6.21, then the hysteresis curve will open up to curve 3 although the full hysteresis curve goes to curve 1.

6.10 Chapter Summary

In this chapter, the heating rate for all the samples was extracted from the data that was collected at Wright State University and Queen's University. From the heating rate, the value of the reduced by mass specific loss power (SPL) was obtained using the heat capacity values that were obtained from literature.

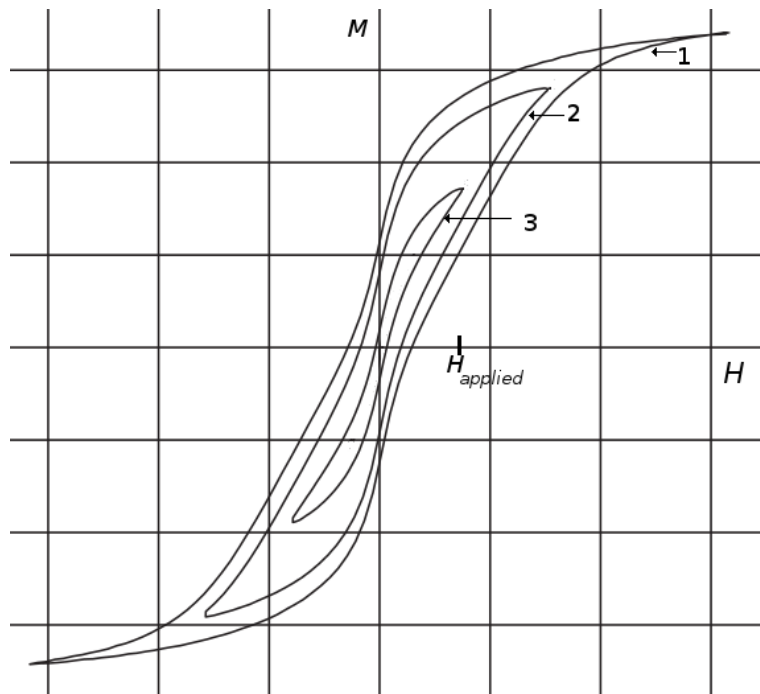


Figure 6.21: Minor loops - The figure shows how the hysteresis loop of a ferromagnetic material opens up as the magnetic field intensity is increased.

Increasing the magnetic field did increase the value of the SPL but not by a linear factor. The SPL increased proportionally when the frequency was increased. The dependence of the value of the SPL on different magnetic properties were also investigated and from our analysis, there is an inverse relationship between the coercive forces and the remanent magnetization. A sample with a lower coercivity (or remanent magnetization) will have a higher SPL value.

CHAPTER 7

Conclusion

As the introduction to this dissertation, a brief review of the different classifications of magnetic materials was achieved. Ferromagnetism, paramagnetism and diamagnetism was discussed. Following that, changing from the magnetism of bulk material to small particle magnetism was examined when the size is reduced to less than 100 nm. The mystery behind high coercivities noted in nanoparticles was explained using the fanning and curling mechanisms. Still in the regime of single-domain particles, there is a special classification whereby single-domain particles are able to overcome the energy barrier and reverse the magnetization over very short time scales. Thermal excitations is responsible for this phenomenon. A particle above a threshold limit is ferromagnetic in nature but below a certain volume, it becomes superparamagnetic and there is no opening in the hysteresis curve. Superparamagnetism is identical to paramagnetism save for the very high saturation magnetization. Magnetic heating was the next issue to be addressed after the foundations on magnetism have been laid. The heating associated with ferromagnetism was addressed whereby the area enclosed by the hysteresis loop gives the power loss. The relevant equations were derived for the power loss. Neel and Brown relaxation is responsible for magnetic heating in superparamagnetic nanoparticles and in the low frequency and high frequency regimes, the power loss was derived. There is also frictional losses when nanoparticles are submerged in a viscous fluid which results in additional heating.

An important quantity was defined to measure the performance of the heating mechanism and is measured experimentally using a calorimetric method.

The system to achieve magnetic heating was designed and implemented. A fiber optic temperature sensor combined with a data logger were responsible to measure precisely the temperature of the nanoparticles. The fiber optic probe was chosen because it is not influenced by the highly oscillating field. The frequency of operation of the system was chosen between 100 kHz to 1 MHz. This frequency range takes into account the safety operating frequency of human tissues. A coil in the shape of a spiral was trusted with the task of producing a magnetic field. A power supply was custom made to convert the direct current into a highly oscillating current. A set of capacitors and an inductor was responsible to set the system in resonance and thus to change the frequency of operation to a certain frequency, the capacitance of the system was altered by toggling the capacitor. Since the frequency of operation is extremely high, the coil heats up and to prevent melting of the copper coil, cold water was injected in the coil. A sample can be mounted inside the coil using a holder. Although water is cooling the system, the can be heat transfer by conduction and convection from the inside of the coil to the sample. The air was sucked out of the system using a vacuum pump since this eliminates convection and conduction. This system was compared to a commercially available system (Ambrell 1 kW induction heater).

Ferromagnetic ferrite magnetic nanoparticles were heated by an alternating magnetic field and from the temperature against time data, a graph was plotted from which the heating rate was inferred. This rate leads to the value of the SPL which was reduced by mass to cater for differences in the mass of nanoparticle used in the different experiments. We found that the lower the coercivity and remanent magnetization, the higher is the SPL value.

7.1 Future Works

Over the last few months, there has been a lot of interest in the application of nanoparticles to cure cancer in the biomedical field. Magnetic hyperthermia and thermoablation therapies which kill tumor cells by the heat generated from an alternating magnetic field when tiny packets of MNPs are placed in the propinquity

of the infected tumor in a living organism. The theory behind this is straightforward; healthy cells can withstand temperatures of up to 42°C but infected cells start to die at this elevated temperature. Hence this will be a non-invasive technique without any surgical tools involved. Notwithstanding, the proper recipe for the nanoparticle that will produce the optimum heating with the minimum quantity of nanoparticle is being researched for the time being.

We can take the results of the present research to the next level by testing it on laboratory rats for example and see whether these nanoparticles eradicate malignant cells or not. A study spanning over several weeks can conclude whether magnetic hyperthermia is a viable process or it is effective only partially (damaged cells reappear after a few weeks or so).

APPENDIX **A**

Procedure for using AMF System

A.1 AMF Hardware

1. Turn ON Neslab water chiller
2. Turn ON Duo-seal vacuum pump
3. Switch ON -18V Powermate power supply
4. On ACDC 5V power supply
5. Turn ON 12V main power supply
6. Start BK precision function generator
7. Switch ON FISO fiber optic temperature probe and load Evolution software on the computer

A.2 Testing

1. Put sample in NMR tube
2. Insert fiber optic temperature probe inside the NMR tube. Ensure that the probe is at the center

3. Allow time for the probe to settle
4. Set the frequency of the main power supply
5. Set the resonant frequency of the BK function generator (see Chapter 5)
6. Start logging with the Evolution software
7. Switch on current supply and rotate knob to desired amperage
8. After desired time, rotate down the current knob before turning off the current supply
9. Turn off the remaining equipment in the reverse order
10. Save data, exit software and shut down the computer

References

- [1] S. LURYI, J. XU, AND A. ZASLAVSKY. *Future Trends in Microelectronics*. Wiley Online Library, 1999. [1](#)
- [2] G. CARPENTER. *Nanotechnology: The Plastics of the 21st Century*. 2006. [3](#)
- [3] J. MOORE. **Small science, big challenge**. *Nature*, **442**:747, 2006. [3](#)
- [4] C. LIEBER. **One-dimensional nanostructures: Chemistry, Physics & applications**. *Solid State Communications*, **107**:607, 1998. [5](#), [6](#)
- [5] B. FAHLMAN. *Materials Chemistry*. Springer. [5](#)
- [6] S. VANAERT, K. BATENBURG, M. ROSSELL, R. ERNI, AND G. VANTENDELOO. **Three-dimensional atomic imaging of crystalline nanoparticles**. *Nature*, **470**:374, 2011. [6](#)
- [7] I. BERTINI. *Inorganic and Bio-inorganic Chemistry*. EOLSS, 2009. [6](#)
- [8] J. JACKSON. *Classical Electrodynamics*. Wiley, 1998. [9](#), [10](#), [11](#)
- [9] M. GETZLAFF. *Fundamentals of Magnetism*. Springer Verlag, 2008. [10](#), [11](#)

-
- [10] B. CULLITY AND C. GRAHAM. *Introduction to Magnetic Materials*. Wiley-IEEE Press, 2009. [14](#), [16](#)
- [11] B. RANA, M. AGRAWAL, S. PAL, AND A. BARMAN. **Magnetization reversal dynamics in clusters of single domain Ni nanoparticles**. *Journal of Applied Physics*, **107**:513, 2010. [19](#)
- [12] M. AGRAWAL, B. RANA, AND A. BARMAN. **Magnetization reversal in chains and clusters of exchange-coupled nickel nanoparticles**. *The Journal of Physical Chemistry C*, **114**:11115, 2010. [19](#)
- [13] B. RANA, A. GANGULY, AND A. BARMAN. **Magnetic shape anisotropy in chemically synthesized chains of nickel nanoparticles**. *IEEE Transactions on Magnetics*, **47**:2859, 2011. [19](#)
- [14] K. KLABUNDE AND R. RICHARDS. *Nanoscale Materials in Chemistry*. Wiley Online Library, 2001. [19](#), [20](#)
- [15] C. BEAN AND J. LIVINGSTON. **Superparamagnetism**. *Journal of Applied Physics*, **30**:120, 1959. [20](#)
- [16] W. SCHUELE AND V. DEETSCREEK. **Appearance of a weak ferromagnetism in fine particles of antiferromagnetic materials**. *Journal of Applied Physics*, **33**:1136, 1962. [20](#)
- [17] T. NEUBERGER, B. SCHÖPF, H. HOFMANN, M. HOFMANN, AND B. VON RECHENBERG. **Superparamagnetic nanoparticles for biomedical applications: Possibilities and limitations of a new drug delivery system**. *Journal of Magnetism and Magnetic Materials*, **293**:483, 2005. [23](#)
- [18] M. MA, Y. WU, J. ZHOU, Y. SUN, Y. ZHANG, AND N. GU. **Size dependence of specific power absorption of Fe_3O_4 particles in AC magnetic field**. *Journal of Magnetism and Magnetic Materials*, **268**:33, 2004. [23](#)

- [19] A. LU, E. SALABAS, AND F. SCHÜTH. **Magnetic nanoparticles: synthesis, protection, functionalization, and application.** *Angewandte Chemie International Edition*, **46**:1222, 2007. [23](#)
- [20] N. KURTI. *Selected Works of Louis Neel*. Routledge, 1 edition, 1 1988. [23](#)
- [21] M. KNOBEL, W. NUNES, L. SOCOLOVSKY, E. DEBIASI, J. VARGAS, AND J. DENARDIN. **Superparamagnetism and other magnetic features in granular materials: A review on ideal and real systems.** *Journal of Nanoscience and Nanotechnology*, **8**:2836, 2008. [24](#)
- [22] C. CHIEN. **Granular magnetic solids.** *Journal of Applied Physics*, **69**:5267, 1991. [25](#)
- [23] Y. LIU, D. SELLMYER, AND D. SHINDO, editors. *Handbook of Advanced Magnetic Materials: Vol 1. Nanostructural Effects. Vol 2. Characterization and Simulation. Vol 3. Fabrication and Processing.* Springer, 1 edition, 11 2005. [25](#), [26](#)
- [24] M. HANSEN AND S. MØRUP. **Estimation of blocking temperatures from ZFC/FC curves.** *Journal of Magnetism and Magnetic Materials*, **203**:214, 1999. [25](#)
- [25] A. JORDAN, R. SCHOLZ, P. WUST, H. FÄHLING, AND R. FELIX. **Magnetic fluid hyperthermia (MFH): Cancer treatment with AC magnetic field induced excitation of biocompatible superparamagnetic nanoparticles.** *Journal of Magnetism and Magnetic Materials*, **201**:413, 1999. [30](#)
- [26] G. BERTOTTI AND I. MAYERGOYZ. *The Science of Hysteresis: Mathematical Modeling and Applications*, **1**. Academic Press, 2006. [31](#)
- [27] G. BERTOTTI. *Hysteresis in Magnetism: for Physicists, Materials Scientists, and Engineers.* Academic Pr, 1998. [31](#)
- [28] Z. HAZNADAR AND Ž. ŠTIH. *Electromagnetic Fields, Waves, and Numerical Methods*, **20**. Ios Pr Inc, 2000. [31](#)

- [29] R. ROSENSWEIG. **Heating magnetic fluid with alternating magnetic field.** *Journal of Magnetism and Magnetic Materials*, **252**:370, 2002. [32](#)
- [30] M. HANSON. **The frequency dependence of the complex susceptibility of magnetic liquids.** *Journal of Magnetism and Magnetic Materials*, **96**:105, 1991. [32](#)
- [31] W. ANDR AND H. NOWAK, editors. *Magnetism in Medicine: A Handbook*. Wiley-VCH, 2nd, completely revised and enlarged edition edition, 1 2007. [32](#), [34](#)
- [32] P. DEBYE. *Polar Molecules*. Dover New York, 1929. [32](#)
- [33] M. SHLIOMIS AND V. STEPANOV. **Theory of the dynamic susceptibility of magnetic fluids.** *Advances in Chemical Physics*, **87**:1, 1994. [32](#)
- [34] E. M. LANDAU L. D. LIFSHITZ. *Electrodynamics of Continuous Media. (Course of Theoretical Physics, Volume 8)*. Addison Wesley, 1966. [33](#)
- [35] R. HERGT, W. ANDRA, C. D'AMBLY, I. HILGER, W. KAISER, U. RICHTER, AND H. SCHMIDT. **Physical limits of hyperthermia using magnetite fine particles.** *IEEE Transactions on Magnetics*, **34**:3745, 1998. [34](#)
- [36] R. HERGT, S. DUTZ, R. MÜLLER, AND M. ZEISBERGER. **Magnetic particle hyperthermia: nanoparticle magnetism and materials development for cancer therapy.** *Journal of Physics: Condensed Matter*, **18**:2919, 2006. [35](#)
- [37] S. CURLEY. **Radiofrequency ablation of malignant liver tumors.** *Annals of Surgical Oncology*, **10**:338, 2003. [36](#)
- [38] B. GHOLAMZADEH AND H. NABOVATI. **Fiber optic sensors.** *Proceedings of World Academy of Science, Engineering and Technology*, **42**:297, 2008. [39](#)
- [39] Y. HEICHAL, S. CHANDRA, AND E. BORDATCHEV. **A fast-response thin film thermocouple to measure rapid surface temperature changes.** *Experimental Thermal and Fluid Science*, **30**:153, 2005. [41](#)

- [40] G. HOROWITZ, B. BACHET, A. YASSAR, P. LANG, F. DEMANZE, J. FAVE, AND F. GARNIER. **Growth and characterization of sexithiophene single crystals.** *Chemistry of Materials*, **7**:1337, 1995. [41](#)
- [41] K. PARK AND D. BANG. **Electrical properties of Ni–Mn–Co–(Fe) oxide thick-film NTC thermistors prepared by screen printing.** *Journal of Materials Science: Materials in Electronics*, **14**:81, 2003. [41](#)
- [42] Y. CHIANG AND T. TAKAGI. **Grain-boundary Chemistry of barium titanate and strontium titanate: II, origin of electrical barriers in positive-temperature-coefficient thermistors.** *Journal of the American Ceramic Society*, **73**:3286, 1990. [41](#)
- [43] C. HAMEL AND É. PINET. **Temperature and pressure fiber-optic sensors applied to minimally invasive diagnostics and therapies.** *Proc. SPIE*, **6083**:608306, 2006. [42](#)
- [44] J. REILLY. **Peripheral nerve stimulation by induced electric currents: Exposure to time-varying magnetic fields.** *Medical and Biological Engineering and Computing*, **27**:101, 1989. [10.1007/BF02446217](#). [44](#)
- [45] P. MACCABEE, V. AMASSIAN, L. EBERLE, AND R. CRACCO. **Magnetic coil stimulation of straight and bent amphibian and mammalian peripheral nerve in vitro: locus of excitation.** *The Journal of Physiology*, **460**:201, 1993. [44](#)
- [46] R. BICKFORD, M. GUIDI, P. FORTESQUE, AND M. SWENSON. **Magnetic stimulation of human peripheral nerve and brain: response enhancement by combined magnetoelectrical technique.** *Neurosurgery*, **20**:110, 1987. [44](#)
- [47] D. FORMICA AND S. SILVESTRI. **Biological effects of exposure to magnetic resonance imaging: an overview.** *BioMedical Engineering Online*, **3**, 2004. [45](#)

- [48] F. DE VOCHT, L. LIKET, A. DE VOCHT, T. MISTRY, P. GLOVER, P. GOWLAND, AND H. KROMHOUT. **Exposure to alternating electromagnetic fields and effects on the visual and visuomotor systems.** *British Journal of Radiology*, **80**:822, 2007. 45
- [49] J. SWANSON AND L. KHEIFETS. **Biophysical mechanisms: a component in the weight of evidence for health effects of power-frequency electric and magnetic fields.** *Radiation Research*, **165**:470, 2006. 45
- [50] A. AHLBOM, J. BRIDGES, R. DESEZE, L. HILLERT, J. JUUTILAINEN, M.O. MATTSSON, G. NEUBAUER, J. SCHÜZ, M. SIMKO, AND K. BROMEN. **Possible effects of electromagnetic fields (EMF) on human health-opinion of the scientific committee on emerging and newly identified health risks (SCENIHR).** *Toxicology*, **246**:248, 2008. 46
- [51] P. BOTTOMLEY AND E. ANDREW. **RF magnetic field penetration, phase shift and power dissipation in biological tissue: implications for NMR imaging.** *Physics in Medicine and Biology*, **23**:630, 1978. 46
- [52] AMBRELL. *Precision Induction Heating EASYHEAT 411*. 2012. 56
- [53] P. GAO, E. REBROV, T. VERHOEVEN, J. SCHOUTEN, R. KLEISMIT, G. KOZLOWSKI, J. CETNAR, Z. TURGUT, AND G. SUBRAMANYAM. **Structural investigations and magnetic properties of sol-gel $Ni_{0.5}Zn_{0.5}Fe_2O_4$ thin films for microwave heating.** *Journal of Applied Physics*, **107**:044417, 2010. 61, 63
- [54] E. REBROV, P. GAO, T. VERHOEVEN, J. SCHOUTEN, R. KLEISMIT, Z. TURGUT, AND G. KOZLOWSKI. **Structural and magnetic properties of solgel $Co_{2x}Ni_{0.5x}Zn_{0.5x}Fe_2O_4$ thin films.** *Journal of Magnetism and Magnetic Materials*, **323**:723, 2011. 63
- [55] S. GEORGE AND C. WILLIAM. *Statistical Methods*. Iowa State University Press, 8 edition, 1 1989. 88

- [56] B. KING. **Heat capacities at low temperatures and entropies of five spinel minerals.** *The Journal of Physical Chemistry*, **60**:410, 1956. [102](#)
- [57] S. ZIEMNIAK, L. ANOVITZ, R. CASTELLI, AND W. PORTER. **Magnetic contribution to heat capacity and entropy of nickel ferrite ($NiFe_2O_4$).** *Journal of Physics and Chemistry of Solids*, **68**:10, 2007. [102](#)
- [58] H. JOSHI, Y. LIN, M. ASLAM, P. PRASAD, E. SCHULTZ-SIKMA, R. EDELMAN, T. MEADE, AND V. DRAVID. **Effects of shape and size of cobalt ferrite nanostructures on their MRI contrast and thermal activation.** *The Journal of Physical Chemistry C*, **113**:17761, 2009. [102](#)
- [59] G. CHACHANIDZE. **Thermodynamic properties of nickel and cobalt ferrites.** *Inorganic Materials*, **26**:314, 1990. [102](#)
- [60] V. BERBENNI, C. MILANESE, G. BRUNI, A. GIRELLA, AND A. MARINI. **Mechanochemical solid-state synthesis of cobalt (II) ferrite and determination of its heat capacity by MTDSC.** *Zeitschrift fur Naturforschung B*, **65**:1434, 2010. [102](#)
- [61] B. REDDY AND P. REDDY. **Low temperature heat capacities of some ferrites.** *Physica Status Solidi (a)*, **22**:219, 1974. [102](#)
- [62] A. KUNDU, C. UPADHYAY, AND H. VERMA. **Magnetic properties of a partially inverted zinc ferrite synthesized by a new coprecipitation technique using urea.** *Physics Letters A*, **311**:410, 2003. [104](#)
- [63] A. HABIB, C. ONDECK, P. CHAUDHARY, M. BOCKSTALLER, AND M. MCHENRY. **Evaluation of iron-cobalt/ferrite core-shell nanoparticles for cancer thermotherapy.** *Journal of Applied Physics*, **103**:307, 2008. [115](#)